

**Debonding Strength Evaluation for Bonded
Axi-symmetric Bodies in Terms of Intensity of
Singular Stress**

By

Zefeng Wang

Department of Mechanical Engineering

Kyushu Institute of Technology

ACKNOWLEDGMENTS

My study at Kyushu Institute of Technology will soon come to an end and, at the completion of my graduation thesis; I wish to express my sincere appreciation to all those who have offered me invaluable help during the four years of my study.

Firstly, I would like to express my heartfelt gratitude to my supervisor, Professor Nao-Aki Noda, for his constant encouragement and guidance. He has walked me through all the stages of the writing of this thesis. I was first introduced to the study in Japan when Professor Noda visited Shandong University, and then he helped me with the application of MEXT scholarship, which supported my study in Japan for 4 years. Without his consistent and illuminating instruction and enthusiastic help, this thesis could not have reached its present form.

Secondly, I should express my heartfelt gratitude to Professor Tatsujiro Miyazaki for his introduction and valuable suggestions in my study. I am also greatly indebted to Dr. Yasushi Takase, who has been supporting my study with patience and kindness since I entered KIT.

I would like to give my hearty thanks to technical consultant Dr. Yoshikazu Sano for his patient instructions in various courses and his precious suggestions for my study here.

My supervisor, Professor Weiming Feng in Shandong University, introduced me to the study in Japan, and helped me in the application of scholarship. I would like to give my thanks to him for all his contribution and encouragement during my toughest period. I am also indebted to him for his constructive comments on my career.

I also owe my sincere gratitude to my friends and my fellow collaborators who gave me their time in helping me work out my problems during the difficult course of the thesis. Especially for Mr. Kazuki Iida, who helped me with the translation of

Japanese.

My thanks would go to my beloved parents, for their loving considerations and great confidence in me all through these years. And I would like give my wife, Mrs. Li Jiang, many thanks for coming along with me all the time. Without her companion in Japan for such long time, I'm not sure I could have the courage to face the difficulty in my study.

Finally, the financial support of MEXT scholarship of Japanese government, which made it possible for my study in Japan, is gratefully acknowledged.

ABSTRACT

The bonded axi-symmetric structures have been widely used in the steel and petroleum industries recent years. However, as is known that there is stress singularity at the end of interface for different materials, which may result in the failure of the joint. The intensity of singular stress field (ISSF) was discussed for bonded plate under arbitrary material combination, while few studies are available for the intensity of bonded structures in axi-symmetric problems, and no results with varying material combination. Thus this research focuses on the analysis of ISSF of different axi-symmetric problems with arbitrary material combinations, which may contribute to evaluating the strength for axi-symmetric structures. And in addition, the analysis method in this study was applied in the analysis of a practical engineering problem to verify the significance of this study. This thesis is composed of total 6 chapters and organized as follows

Chapter 1 gives an introduction of composites and bonded structures applied to aviation industry, microelectronic packaging, and steel process equipment. Also the applications and importance of bonded axi-symmetric structure are investigated. For example the application in thermal spray coating roll used in continuous annealing furnace and bonded joint of riser pipe in offshore oil equipment. With the extensive application of the technology, structural failure problems are emerging, which requires further study. Then, the issues of the research on singularity in the bonded structures are reviewed, and it is found that there are only few papers focused on the ISSF for bonded axi-symmetric problems. Then, the research purpose of this thesis is introduced, focusing on the analysis of ISSF for bonded axi-symmetric structures.

In chapter 2, the proportional method is discussed for axi-symmetric problems. It is known that FEM is not suitable for the solution of bimaterial problems due to the mesh dependence of singular stress near the end of interface. However, FEM is still

useful in the analysis of singular stress problems since FEM error can be eliminated by applying the proportional method. This study extends the method to the bonded axis-symmetric problems. However, the difference between bonded plane problems and axis-symmetric problems makes the application of proportional method quite difficult. This is because non-singular stress appears due to non-zero circumferential strain ε_{θ} . Then, non-singular terms are derived explicitly and eliminated from the stress components calculated by FEM to extend this method to axis-symmetric problems. Finally the method is verified by numerical analysis.

In chapter 3, the ISSF for the bonded cylinder is first calculated by changing the material combination systematically after extending of the proportional method to axis-symmetric problems. Then, the results are compared with that of plane strain problem and the differences are elaborated. It is found that the ISSF of axis-symmetric problem can not be governed by the Dundurs' parameters, therefore, the maximum and minimum values of the SIFs are considered and shown in tables and charts in the space of Dundurs' parameters.

Chapter 4 mainly focuses on another type of axis-symmetric bonded structure, bonded pipe. The effect of inner radius on ISSF is also discussed. Generally, it is thought that the bonded pipe with an infinite inner diameter is equivalent to the plane strain problem, but it is found that they are quite different. Therefore, the results of bonded pipe with infinite inner diameter are compared with the plane strain problem. As is done in analysis of bonded cylinder in chapter 3, the maximum and minimum values of the ISSF are considered and shown in tables and charts in the space of Dundurs' parameters.

Chapter 5 shows an example of the proposed method applied to a practical engineering problem. By using the aforementioned analysis proposed for bonded axis-symmetric structures, a pipe shaped hearth roll used in continuous annealing furnace for producing steel sheet is investigated. Spraying coating is commonly used in the hearth roll. However, after long-term use under high temperature and thermal shock,

the spray coating, which is a sandwich bonded structure, will peel off. Thus, Chapter 5 discusses how to improve the strength of the spray coating under thermal shock. It is found that thinner top coating always has better thermal shock resistance. And under fixed top coating thickness, the ISSF takes a minimum value when the coating thickness ratio $H/h \cong 2$, which is in accord with the previous research for plane strain state and experimental results in engineering. Here, H and h represent the top coating thickness and bond coating thickness, respectively.

In the last chapter of this thesis, chapter 6, main conclusions of this study are summarized for bonded cylinder and bonded pipe, and for the optimum design of thermal spray coating.

特異応力場の強さに注目した異種材料接合軸対称体の構造強度評価に関する研究

【論文の要旨】

近年、パイプ接合などの軸対称接合構造が鉄鋼、石油産業などにおいて使用されてきている。しかし、異種材料接合体の界面端で特異応力が発生することがあり、それは接合部の損傷へとつながり、そこから広範囲の破壊に波及する場合がある。任意の材料を組合せた接合板の特異応力場の強さ (ISSF) については、すでに体積力法を用いて精度の良い解析が数多く行われている。しかし、軸対称接合体の特異応力場の強さに関する研究は、ほとんど行われていない。そこで、本研究では、軸対称接合体の特異応力場の強さの問題に注目して、任意の異種材料組合せによる種々の ISSF を調査、解析して考察を加えた。本研究で得られた知見や解析方法を用いることによって、一般的な軸対称接合問題に関する強度の理解に役立てることができるだけでなく、実際の工学上の問題にも応用可能である。本論文は、全 6 章から構成されている。

まず、第 1 章では本研究の背景として、航空産業、マイクロエレクトロニクス部品のパッケージ、鉄鋼プロセス装置などにおける複合構造の応用例について述べている。また、接合された軸対称構造のアプリケーションと重要性が調査されている。例えば、薄鋼板を生産する連続焼鈍炉内で用いられる表面コーティングされたハスロールとオフショア石油掘削・生産装置で用いられるライザ管継手等である。しかし、文献調査の結果により、接合軸対称体の特異応力場の強さに対する研究が少ないことがわかり、異種材料で接合された軸対称体を対象にした特異応力場の強さの解析が本研究目的とされている。

第 2 章では平面問題に適用する比例法を軸対称問題に拡張して適用したことが述べられている。有限要素法 (FEM) では、メッシュ依存性という問題があり、FEM は異種材料問題の解析には適していない。しかし、西谷により提案された比例法では、FEM の解析誤差を除去できるので、この方法を用いれば特異応力問題の解析においても FEM が有用であり、本研究もこの方法が拡張して適用されている。平面問題と軸対称問題は異なり、特に周方向ひずみがゼロにな

らない非特異応力項の存在が,この比例法を軸対称問題に直接適用することを困難にしている。そこで,この非特異応力を導出し、FEM における応力成分から取り除かれた。その結果,この拡張した比例法により,良好な結果が得られることが確認された。

第 3 章では接合円柱の特異応力場の強さを材料の組合せを変えて系統的に解析したことが述べられている。さらに,得られた結果を平面問題と比較し,その違いについて考察された。平面応力問題において知られている界面端部付近の ISSF は,Dundurs パラメータ α, β により支配される。しかし,接合円柱問題における ISSF は α, β のみにより表現できない。解析結果は,ISSF の最大値と最小値とが比較検討され,Dundurs パラメータが用いられて図表の形で示されている。

4 章では,2 重管接合部が接合板の問題と比較対比して解析されている。ここでは,ISSF への内半径の影響も検討されている。まず,接合板に近いと考えられる接合管内半径が ∞ の場合が考察されている。このようなパイプ形状では,一般には平面ひずみとみなされるが,この近似によりどの程度の誤差が生じるかについて解析によって明らかにされている。そして,応力場の強さ ISSF の最大値と最小値を比較検討し,Dundurs パラメータを用いて図表の形で示されている。

第 5 章では,第 4 章で述べた方法を実用的な工学上の問題への適用例が述べられている。軸対称接合構造に本解析法を適用するために,前述の結果を用いて,メッキ鋼板生産用連続焼鈍炉内で用いられるハースロールが取り挙げられている。ハースロールでは,溶射によるセラミックコーティングが施されて使用され,この構造は多重管とみなすことができ,ステンレス製中空スリーブの外形面に 2,3 層のコーティングが施されている。コーティング層が長時間使用にともなうはく離が課題となっており,炉の降温過程で作用する熱応力が主たる要因と考えられている。したがって,第 5 章では,ロール冷却時における熱衝撃下でのスプレーコーティングの強度を向上させる方法に焦点を当てた解析がなされている。最表層のトップコートが薄いほど,耐熱衝撃性に良いことが

見出されている。また,トップコート(厚さ H)とその下層のボンドコート(厚さ h)の最適な厚比 H/h は,特異応力場の観点から考察した結果, $H/h \cong 2.0$ で最適であることが示されている。この結果は,平面ひずみ条件で考察した以前の研究や直方形の一面にコーティングを施して,行った実験結果とも一致することが述べられている。

最後の第 6 章では結論として,接合軸対称問題の特異応力場の強さ,及び溶射皮膜の最適設計への応用を議論するとともに本研究論文全体をまとめている。

TABLE OF CONTENTS

ACKNOWLEDGMENTS	ii
ABSTRACT	iv
TABLE OF CONTENTS	x
LIST OF TABLES	xii
LIST OF FIGURES	xiv
NOMENCLATURE	xvii
Chapter 1 Introduction	1
1.1 Research Backgrounds	1
1.2 Studies history	3
1.3 Research Purposes	6
1.4 Overview of chapters	9
1.5 Reference of Chapter 1	11
Chapter 2 Extended proportional method and the basic reference problem for the analysis of axi-symmetric problems	16
2.1 Introduction	16
2.2 Numerical analysis method	18
2.3 Intensity of singular stress for bonded strip as a reference solution	22
2.4 Extended proportional method in bonded axi-symmetric problems	25
2.5 Discussion on the similarity of singular stress field and FEM model	29
2.6 Conclusions	34
2.7 Reference of Chapter 2	35
Chapter 3 Analysis on Intensity of Singular Stress for Cylinder in Comparison with Bonded Plate	37
3.1 Introduction	37
3.2 Difference of singularity between bonded plate and bonded cylinder	38

3.3 Discussion of suitable prediction for debonding strength	40
3.4 Analysis results for bonded cylinder under arbitrary material combinations	43
3.5 Conclusion and discussion	47
3.6 Reference of Chapter 3.....	48
Chapter 4 Analysis on Intensity of Singular Stress for Bonded Pipe in Comparison with Bonded Plate.....	50
4.1 Introduction	50
4.2 Effect of inner radius R_i on stress distribution of bonded pipe.....	52
4.3 Analysis method for bonded pipe.....	56
4.4 Difference of singularity between bonded plate and bonded pipe.....	61
4.5 Discussion of suitable prediction for debonding strength	62
4.6 Analysis results for bonded pipe under arbitrary material combinations	65
4.7 Conclusion and discussion	69
4.8 Reference of Chapter 4.....	70
Chapter 5 Analysis on singular stress intensity of ceramic spray coating on hearth roll.....	72
5.1 Introduction	72
5.2 Key parameters for analysis	78
5.3 Analysis method for the singularity of thermal stress	81
5.4 Results and Discussion for the Intensity of Singular Stress Field	86
5.5 Conclusion	91
5.6 Reference of Chapter 5.....	92
Chapter 6 Conclusion	95
Appendix A	98
A.1 Introduction.....	98
A.2 Thermal shock test for evaluating the peeling strength of sprayed coating.....	100
A.3 Analysis method for the singularity of thermal stress	101
A.4 Results and discussion for the intensity of singular stress field	105
A.5 Conclusion.....	112
A.6 Reference of Appendix A.....	113

LIST OF TABLES

Table 2.1 Singular index λ for different material combinations	19
Table 2.2 Ratio of stress for different problems ($t/W=0.01$)	22
Table 2.3 Dimensionless SIF F_σ at the end of interface for a bonded strip.....	24
Table 2.4 Ratio of $\sigma_{ij0,FEM}^{BUTT} / \sigma_{ij0,FEM}^{PLT}$	25
Table 2.5 Ratio of $\sigma_{ij0,FEM}^{CYL} / \sigma_{ij0,FEM}^{PLT}$	25
Table 2.6 Material property	32
Table 2.7 Stress components of bonded cylinder and bonded plate	32
Table 2.8 The constituents of the non-singular terms of bonded cylinder	33
Table 2.9 Stress ratio of bonded cylinder and bonded plate	34
Table 3.1 Maximum value of $F_\sigma^{CYL} / F_\sigma^{PLT}$	44
Table 3.2 Minimum value of $F_\sigma^{CYL} / F_\sigma^{PLT}$	45
Table 3.3 Maximum value of $\sigma_{z0,FEM}^{CYL} / \sigma_{y0,FEM}^{PLT}$	45
Table 3.4 Minimum value of $\sigma_{z0,FEM}^{CYL} / \sigma_{y0,FEM}^{PLT}$	46
Table 4.1 Stress components at the end of interface for a bonded pipe with different inner radius	53
Table 4.2 FEM results for bonded pipe with $e_{min}=2^{-13}$	58
Table 4.3 FEM results for bonded pipe with $e_{min}=2^{-17}$	58
Table 4.4 Stress ratio for bonded plate and bonded pipe with different inner radius	60
Table 4.5 Maximum value of $F_\sigma^{PIPE} / F_\sigma^{PLT}$	66
Table 4.6 Minimum value of $F_\sigma^{PIPE} / F_\sigma^{PLT}$	67
Table 4.7 Maximum value of $\sigma_{z0,FEM}^{PIPE} / \sigma_{y0,FEM}^{PLT}$	67
Table 4.8 Minimum value of $\sigma_{z0,FEM}^{PIPE} / \sigma_{y0,FEM}^{PLT}$	68

Table 5.1 Material properties of several typical metals and ceramics	74
Table 5.2 Dundurs' parameters (α , β) for different combinations of metals and ceramics	75
Table 5.3 Singular index λ for different combinations between metals and ceramics	75
Table 5.4. Material Properties depending on temperature	80
Table 5.5 Stress ratio of bonded axi-symmetric problem and reference problem	86
Table 5.6 K_{σ} for 8YZ at 1000°C (axi-symmetric model)	89
Table 5.7 K_{σ} for 8YZ at 1000°C (plane strain model)	90
Table 5.8 $K_{\sigma}^{plane} / K_{\sigma}^{axial-symmetric}$ of 8YZ at 1000°C	90
Table A.1 Material Properties depending on temperature	101
Table A.2 Stress distribution on the interface and the ratio of the stress	105
Table A.3 This table shows that K_{σ} value of the influence factor changes with time for top coating 8YZ	107
Table A.4 K_{σ} for 8YZ at 1000°C of two layers model	109
Table A.5 K_{σ} at 1000°C of three layers model when fixed $H_1=0.075\text{mm}$ [$\text{MPa} \cdot \text{m}^{0.1127}$]	110
Table A.6 K_{σ} at 1000°C of three layers model when fixed $H_2=0.075\text{mm}$ [$\text{MPa} \cdot \text{m}^{0.1127}$]	111

LIST OF FIGURES

Fig. 1.1 The electrical device Chip Scale Package	1
Fig. 1.2 Application of composite in Boeing 787 air plane	2
Fig. 1.3 The debonding from the end of adhesive joint of Chip Scale Package (CSP).....	3
Fig. 1.4 Several forms of composite material interface failure.....	3
Fig. 1.5 Several typical problems of stress concentration	6
Fig. 1.6 Structure of (a) bonded cylinder, (b) bonded pipe.....	7
Fig. 1.7 Hearth roll used in continuous annealing furnace for producing steel sheet	8
Fig. 1.8 Bonded structure of hearth roll.....	8
Fig. 2.1 Several bonded structures.....	17
Fig. 2.2 Stress near the end of interface calculated by FEM	20
Fig. 2.3 Unknown problem and given reference problem in same FE mesh pattern	21
Fig. 2.4 F_σ for a boned strip in Fig. 2.1(a)	23
Fig. 2.5 (α, β) space	23
Fig. 2.6 Singular stress at the end of interface for plane strain problem.....	26
Fig. 2.7 Singular stress at the end of interface for axi-symmetric problem.....	26
Fig. 2.8 Effect of mesh pattern on the stress distribution along the interface	30
Fig. 2.9 FEM model for bonded strip	31
Fig. 2.10 FEM model for bonded cylinder	31
Fig. 3.1 Bonded plate and bonded cylinder	37
Fig. 3.2 v_2 VS. v_1 under $(\alpha, \beta)=(0.5,0.2)$	38
Fig. 3.3 E_2/E_1 VS. v_1 under $(\alpha, \beta)=(0.5,0.2)$	39
Fig. 3.4 $\sigma_{z0,FEM}^{CYL} / \sigma_{y0,FEM}^{PLT}$ and $F_\sigma^{CYL} / F_\sigma^{PLT}$ VS. v_1 under $(\alpha, \beta)=(0.5,0.2)$	39
Fig. 3.5 Infinite value of $F_\sigma^{CYL} / F_\sigma^{PLT}$ at equal pair.....	40
Fig. 3.6 Maximum value of $F_\sigma^{CYL} / F_\sigma^{PLT}$ and $\sigma_{z0,FEM}^{CYL} / \sigma_{y0,FEM}^{PLT}$ when $\beta=0.2$	42
Fig. 3.7 Maximum value of $F_\sigma^{CYL} / F_\sigma^{PLT}$ and $\sigma_{z0,FEM}^{CYL} / \sigma_{y0,FEM}^{PLT}$ when $\beta=0.2$	42

Fig. 3.8 Maximum value of $F_{\sigma}^{CYL}/F_{\sigma}^{PLT}$ and $\sigma_{z0,FEM}^{CYL}/\sigma_{y0,FEM}^{PLT}$ in (α, β) map	43
Fig. 3.9 Minimum value of $F_{\sigma}^{CYL}/F_{\sigma}^{PLT}$ and $\sigma_{z0,FEM}^{CYL}/\sigma_{y0,FEM}^{PLT}$ in (α, β) map	44
Fig. 3.10 Material combinations in (α, β) space	46
Fig. 4.1 Bonded plate and bonded pipe	50
Fig. 4.2 Pipe with different thickness of wall	52
Fig. 4.3 Inner point and outer point at the end of interface for a bonded pipe.....	52
Fig. 4.4 σ_r at end of interface	54
Fig. 4.5 σ_z at end of interface.....	54
Fig. 4.6 σ_{θ} at end of interface.....	55
Fig. 4.7 τ_{rz} at end of interface	55
Fig. 4.8 FEM mesh for bonded pipe	57
Fig. 4.9 Stress ratio for bonded pipe with different inner radius and bonded plate	59
Fig. 4.10 v_2 and E_2/E_1 VS. v_1 under $(\alpha, \beta)=(0.5,0.2)$	61
Fig. 4.11 $\sigma_{z0,FEM}^{PIPE}/\sigma_{y0,FEM}^{PLT}$ and $F_{\sigma}^{PIPE}/F_{\sigma}^{PLT}$ VS. v_1 under $(\alpha, \beta)=(0.5,0.2)$	62
Fig. 4.12 Infinite value of $F_{\sigma}^{PIPE}/F_{\sigma}^{PLT}$ at equal pair	63
Fig. 4.13 Maximum value of $\sigma_{z0,FEM}^{PIPE}/\sigma_{y0,FEM}^{PLT}$ and $F_{\sigma}^{PIPE}/F_{\sigma}^{PLT}$ when $\beta=0.2$	64
Fig. 4.14 Maximum value of $\sigma_{z0,FEM}^{PIPE}/\sigma_{y0,FEM}^{PLT}$ and $F_{\sigma}^{PIPE}/F_{\sigma}^{PLT}$ when $\beta=0.3$	64
Fig. 4.15 Maximum value of $\sigma_{z0,FEM}^{PIPE}/\sigma_{y0,FEM}^{PLT}$ and $F_{\sigma}^{PIPE}/F_{\sigma}^{PLT}$ in (α, β) map	65
Fig. 4.16 Minimum value of $\sigma_{z0,FEM}^{PIPE}/\sigma_{y0,FEM}^{PLT}$ and $F_{\sigma}^{PIPE}/F_{\sigma}^{PLT}$ in (α, β) map.....	66
Fig. 5.1 Hearth roll used in CAL	72
Fig. 5.2 Material combinations of metal and ceramics in (α, β) space	75
Fig. 5.3 Specimen for thermal shock test and the test conditions	76
Fig. 5.4 Thermal shock test specified by JIS8304(2007).....	79
Fig. 5.5 Relationship between material properties and temperature	80
Fig. 5.6 Analytical model and FEM mesh	81

Fig. 5.7 Relationship between temperature and singular index λ	82
Fig. 5.8 Comparing known problem and unknown problem	84
Fig. 5.9 Basic axi-symmetric problem and bonded plate.....	85
Fig. 5.10 Analysis model and local FEM mesh.....	87
Fig. 5.11 Stress history at the end of interface around the water cooling	88
Fig. 5.12 K_{σ} for each constant thickness H of top coating.....	89
Fig. A.1 Specimen for thermal shock test and the test conditions	99
Fig. A.2 Results of thermal shock test.....	100
Fig. A.3 Analytical model and FEM mesh	101
Fig. A.4 Relationship between various material properties and temperature	103
Fig. A.5 Comparing known problem and unknown problem	104
Fig. A.6 Stress and intensity of the singular stress at the end of interface.....	107
Fig. A.7 K_{σ} value of the influence factor changes with time	108
Fig. A.8 K_{σ} for 20YZ, 12YZ, 8YZ at 1000°C with varying ceramic coat thickness H when h=0.1mm	109
Fig. A.9 Three layers ceramic coating model used to analysis.....	110
Fig. A.10 K_{σ} at 1000°C of three layers model when fixed $(H_1+H_2)=0.15\text{mm}$, $h=0.075\text{mm}$	111
Fig. A.11 Comparison of the results for the three-layer and two-layer	112
Fig. A.12 Relationship between Nc and K_{σ}	112

NOMENCLATURE

E_j	Young's modulus of material j
e_{min}	minimum element size of FE model
F_σ	dimensionless intensity of stress singularity
G_j	shear modulus of material j
H	height of the FE model for each material
ISSF	intensity of singular stress field
K_σ	intensity of stress singularity
r	radial axis
R	distance from the end of interface
R_i	inner radius of the roller
SIF	stress intensity factor
SIFs	stress intensity factors
t	thickness of bond layer in a butt joint
W	width of the FE model
α, β	Dundurs' parameters
ε_θ	circumferential strain
θ	circumferential axis
κ_j	Kolosov constant of material j
λ	order of stress singularity (singular index)
$\sigma_{z0, FEM}^{Axial}, \tau_{rz0, FEM}^{Axial}$	FE stresses at the end of interface for axi-symmetric problem
$\sigma_{y0, FEM}^{PLT}, \tau_{xy0, FEM}^{PLT}$	FE stresses at the end of interface for reference problem
ν_j	Poisson's ratio of material j
z	axial axis

Chapter 1 Introduction

1.1 Research Backgrounds

Modern technology has led to the employing of composites and bonded structures/multiple layers in automotive and aerospace industries as well as in microelectronics packaging. The significant size and weight reduction offered by the chip scale packages (CSP) makes it ideal for the use in mobile devices like cell phones, laptops, palmtops, and digital cameras. The advantages offered by CSP include smaller size (reduced footprint and thickness), lesser weight, relatively easier assembly process, lower over-all production costs and improvement in electrical performance.

Fig.1.1 demonstrated a wire-bonded uBGA ball grid array chip scale packaging solution [1]. A typical chip scale packaging process starts with the mounting of the die on the interposer using epoxy. The die is then wire-bonded to the interposer using gold or aluminum wires. Plastic encapsulation then follows to protect the die and wires, usually by transfer molding. After encapsulation, solder balls are attached to the bottom side of the interposer. Finally, the parts are separated from the lead frame.

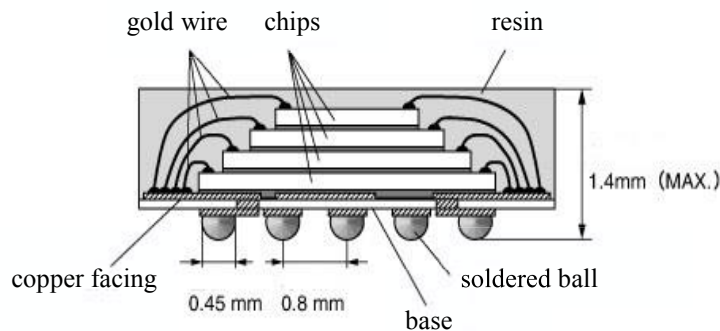


Fig. 1.1 The electrical device Chip Scale Package

Also composites are widely used in aviation industries. The Advance Composite Material(ACM) was first applied in the manufacturing of F-14 jet fighter since 1960s. The application of ACM in the development of F-18 fighter became more mature. Until F-22, up to 24% of composite were used in the building of the body. In civil aviation,

Boeing first has composite used in the manufacturing of the rudder on B767 air plane, and in the new B787 air plane, up to 50% of composites were used. Air Bus has also developed its own new air crafts with composites are widely used such as A380 and the new A350XWB.[2-8]

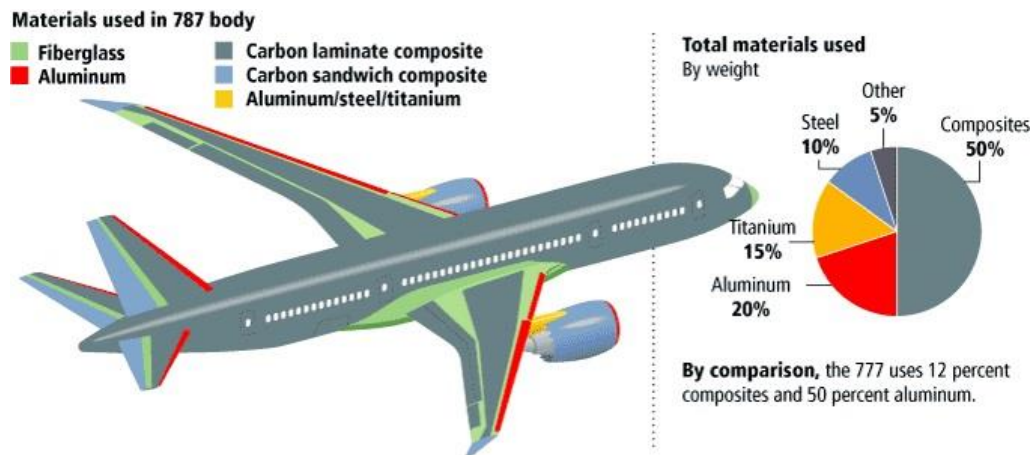


Fig. 1.2 Application of composite in Boeing 787 air plane

However, a mismatch of different materials properties may cause stress singularity at the edge of an interface between different materials, which leads to failure of bonding part in structures. As can be seen from Fig. 1.1, quite a lot interfaces exist inside the CSP assemblies. Stress concentration happens along the interfaces due to the discontinuous of material property and geometric configuration. And cyclic pressure and temperature as well as humidity will increase the speed of delamination. Therefore, there is an increasing concern that the CSP assemblies may not meet the mechanical and the thermal cycling reliability requirements. In Fig. 1.3, the cross-section image reveals delamination after the 3x JEDEC 260° C reflow test. Delamination initiates at the interface between the underfill and the flux residue, and then propagated along the solder mask [9].

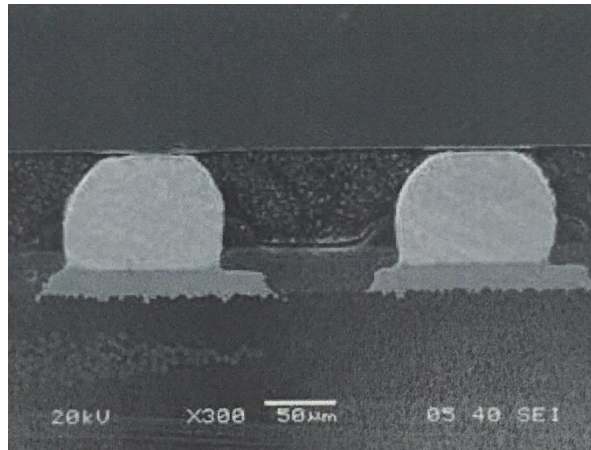


Fig. 1.3 The debonding from the end of adhesive joint of Chip Scale Package (CSP)[9]

Fig. 1.4 illustrates several forms of composite material interface failure. The reliability evaluations based on fracture mechanics on the interface problems composites win quite a lot of attentions. The strength analysis and the failure criteria of bonded structures are becoming more and more important.

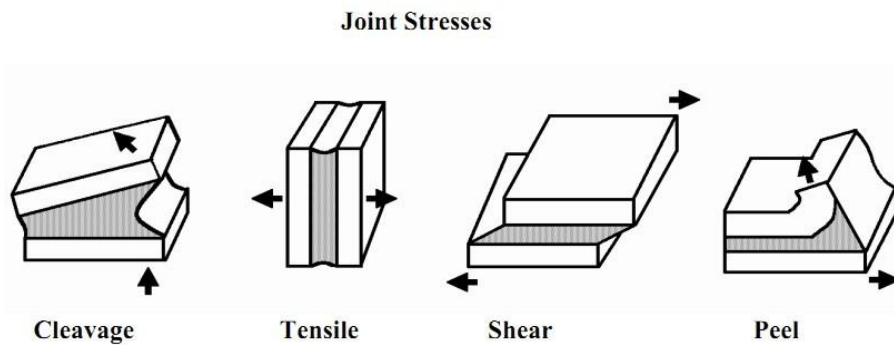


Fig. 1.4 Several forms of composite material interface failure

1.2 Studies history

For elastic fracture mechanics concepts to the debonding strength evaluation between dissimilar materials, Williams [10] was the first to determine the characteristic oscillating stress singularity at the crack tip in the elastic interfacial crack problem. Then, elastic solutions around the interface crack tip to specific problems were discussed by Erdogan [11, 12], England [13], and Rice and Sih [14]. Bogy [15] revealed that the stresses at the interface corner approach infinity (stress singularity) in elastic bi-material planes. This qualitatively explained why the failures of the bonded structures

mostly initiate from the interface corner in the engineering.

From the view of linear elastic theory, the stress singularity occurring at end of interface is an important feature for the biomaterial composites. The intersection points of the free boundary and interface is the singular point of elastic stress, which is also the starting point of interface crack. So far, many studies have been done to evaluate this kind of singularity. For 2-D models of dissimilar materials structure, the characteristic equation, which controls the order of singularity, was derived [15-27]. And especially, Dundurs et al. proposed two elastic mismatch parameters α , β which can be used to express the singularity of a material combination [21, 22]. The Dundurs' parameters α , β are defined as the following equation.

$$\alpha = \frac{G_1(\kappa_2 + 1) - G_2(\kappa_1 + 1)}{G_1(\kappa_2 + 1) + G_2(\kappa_1 + 1)}, \quad \beta = \frac{G_1(\kappa_2 - 1) - G_2(\kappa_1 - 1)}{G_1(\kappa_2 + 1) + G_2(\kappa_1 + 1)},$$

$$\kappa_j = \begin{cases} \frac{3 - \nu_j}{1 + \nu_j} & (\text{plane stress}) \\ 3 - 4\nu_j & (\text{plane strain}) \end{cases}, \quad G_j = \frac{E_j}{2(1 + \nu_j)} \quad (j = 1, 2)$$

Here, G_j , E_j and ν_j denote shear modulus, Young's modulus and Poisson's ratio for material j in the bonded structure, respectively. The ISSFs for the aforementioned problem in plane strain or plane stress are only determined by these problems. Thus these parameters are very important for the later research of biomaterial problems. And Boggy et al. made great efforts on the research of singular index λ [15-20], which is the root of the following equation. Here α , β are Dundurs' parameters.

$$\left[\sin^2\left(\frac{\pi}{2}\lambda\right) - \lambda^2 \right] \beta^2 + 2\lambda^2 \left[\sin^2\left(\frac{\pi}{2}\lambda\right) - \lambda^2 \right] \alpha\beta + \lambda^2(\lambda^2 - 1)\alpha^2 + \frac{\sin^2(\pi\lambda)}{4} = 0$$

In the engineering design, to understand the existence of singularity at the end of interface or the intensity of singularity is very important. However, there are still confusion about the singular stress field around end of interface [28,29], strength evaluation method and the evaluation parameters has not been established. Particularly, the present research usually limited with plane problem, however, the axi-symmetric problems or 3-D problems are also not rare. And there are only few researches on strength evaluation for these cases.

The small peel near or on the interface are called crack. The analysis of interfacial crack and its theoretical solution were first started by Williams [30] and Irwin [31] from 1957, at the same time, they founded system of linear elastic fracture mechanics for homogeneous materials. Then Williams [26] was be first to determine the characteristic oscillating stress singularity at the crack tip in the elastic interfacial crack problem, Then, elastic solutions around the interface crack tip to specific problems were discussed by Erdogan [32,34], England [35].

During 1960s, based on Erdogan [32, 34], Rice and Sih'[36,37] study and Muskhelishvili' [38] elasticity theory, the research on the analytic solutions for crack at the interface of dissimilar isotropic materials in 2D problem was popular. In which, the stress intensity factors of an interface crack problem was defined in the form of a complex number.

However, because of the difficulty in explaining the oscillatory of singularity and confusion of definition, the strength evaluation method of dissimilar materials can't be established without linear fracture mechanics theory for interfacial crack problem. But from around 1985, since new composite material, such as ceramics and microelectronic device were widely used, and strength evaluation of these composites were required and became important again. Recently, some researchers proposed the method for accurately calculating the intensity of the singular stress field for the butt joints (Fig. 1.5(d)) and the single lap joints [39, 40], and reported that the debonding strengths of the adhesive joints can be expressed with $K_\sigma = K_{\sigma c}$ [39, 41, 42], where K_σ is the intensity of singular stress field, $K_{\sigma c}$ is the critical value of the K_σ . Because the K_σ is suitable for evaluating the adhesive strength of the bonded structure, it is expected that it becomes possible to calculate the K_σ of the various bonded structures easily.

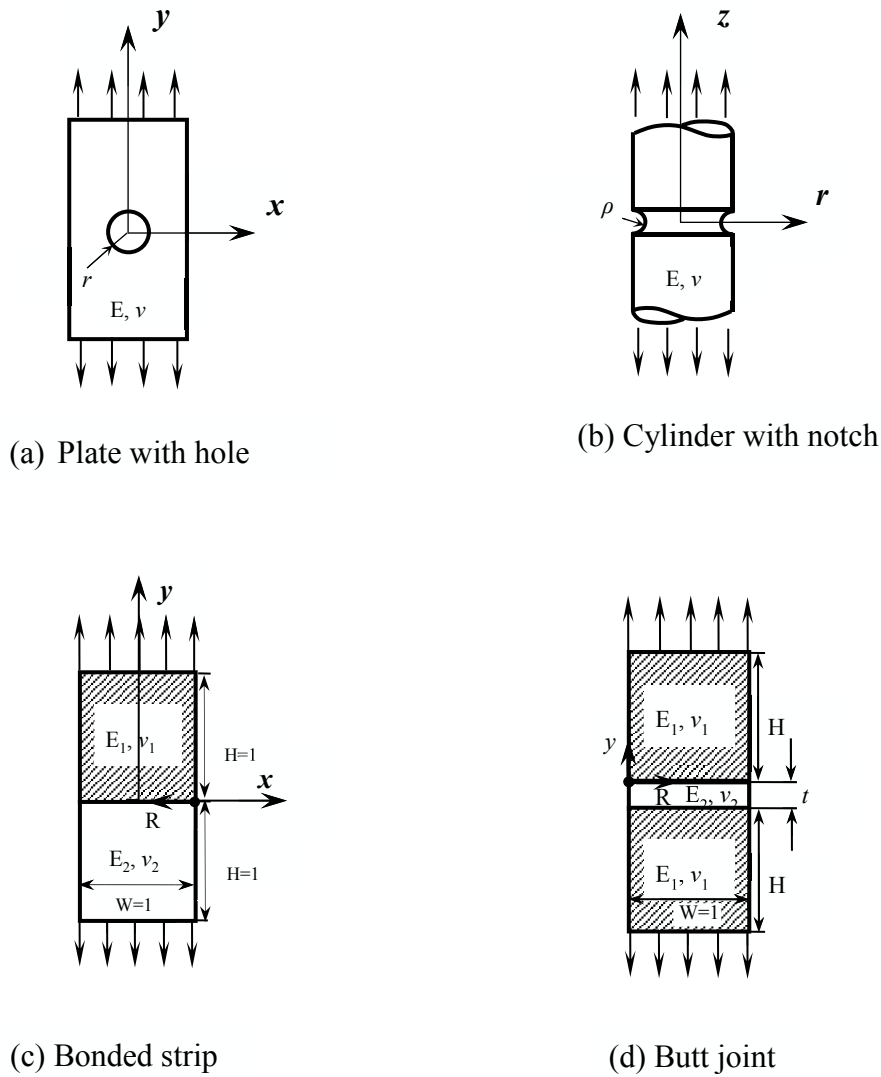


Fig. 1.5 Several typical problems of stress concentration

1.3 Research Purposes

In the standard testing method, the specimens such as the bonded plates(Fig. 1.5(c)) and the bonded cylinders(Fig. 1.6(a)) are often adopted. It is well known that the asymptotic solutions of the bonded cylinder and the bonded plate are similar. However, they are not completely same. For example, for the famous stress concentration problem of a plate with hole(Fig. 1.5(a)), the SIF is independent of material and the size of the hole. While for the cylinder with notch(Fig. 1.5(b)), if the geometry boundary condition is same, the SIF is only controlled by the Poisson's ratio of the material, which means we can determine the ISSF as long as we got the Poisson's ratio of the material.

Furthermore, for the bimaterial bonded structure in plane state(Fig. 1.5(c)), the SIF depends on both materials' properties, therefore the Dundurs' parameters α , β are necessary to express the ISSF. And as we all know, the ISSF for each set of α , β is constant although the material combinations under these parameters can vary. However the situation in bonded axi-symmetric problems are little different from the aforementioned problems. Special stress concentration occurs at the interface corner edge of the axi-symmetric bonded structures [44, 45], and the non-singular term is included in the asymptotic solution of the bonded cylinder [46]. Even though the bonded cylinder and the bonded plate in plane strain condition have same order of stress singularity [43]. The researchers proposed the method for accurately and easily calculating the intensity of the singular stress field for the bonded plate by solving the ISSFs under (α, β) space. However, it is not examined whether the method can be applied to the bonded axi-symmetric problems. Thus this study will focus on the ISSFs of axi-symmetric problems under (α, β) space.

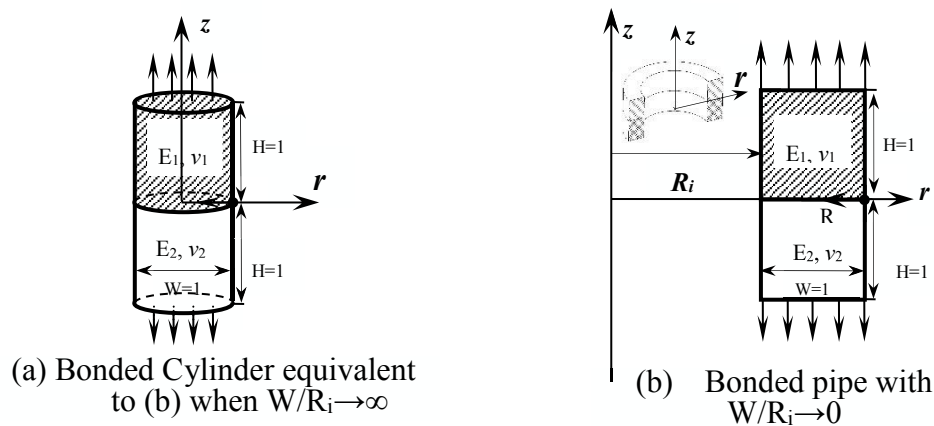


Fig. 1.6 Structure of (a) bonded cylinder, (b) bonded pipe

In this research, FE analyses are performed on the bonded plate (Fig. 1.5(c)) and the bonded cylinder/pipe (Figs. 1.6(a),(b)) which are subdivided by the same mesh pattern, and the differences between them will be clarified from the results. And the method for accurately calculating the intensity of the singular stress field for the bonded axi-symmetric problems will be obtained. The intensity of the singular stress field for the bonded axi-symmetric problems will be calculated by changing the material

combinations systematically and be compared with that for the bonded plate. Generally, it is well known that the stress state in the bonded pipe can be regarded as the plane strain condition when the inner radius of the bonded pipe R_i approaches infinite. However, since the existence of circumferential strain and non-singular terms of stress, there is difference between the singular stress fields of bonded pipe and the bonded plate in the plane strain condition, so it's necessary to compare and clarify them.

By using the aforementioned results for bonded axi-symmetric structures, a practical engineering problem will be studied in the last part of this research. Figure 1.7 shows the structure of a hearth rolls used in continuous annealing furnace for producing steel sheet. It's common to apply spraying coating on the hearth rolls. Figure 1.8 shows the quarter structure of the roller, is a sandwich bonded structure. After long term of use under high temperature, the spray coating will peel off. The last part of this study will focus on how to improve the strength of the spray coating under thermal shock.



Fig. 1.7 Hearth roll used in continuous annealing furnace for producing steel sheet

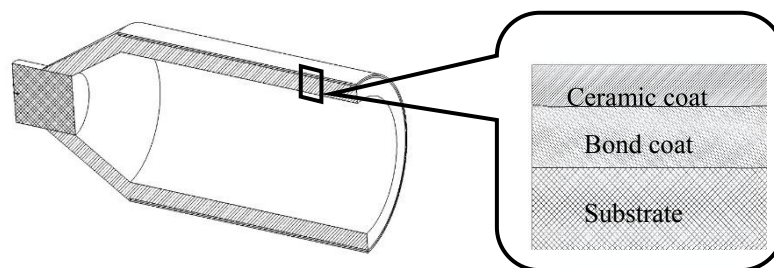


Fig. 1.8 Bonded structure of hearth roll

1.4 Overview of chapters

The bonded axi-symmetric structures have been widely used in the steel and petroleum industries recent years. However, as is known that there is stress singularity at the end of interface for different materials, which may result in the failure of the joint. The intensity of singular stress is discussed for bonded plate under arbitrary material combination [47]. Few studies are available for the intensity of bonded structures in axi-symmetric problems, and no results with varying material combination. Thus this study will focus on the analysis of ISSFs for axi-symmetric bonded problems.

FEM is not suitable for the solution of bimaterial problems due to the mesh dependence of singular stress near the end of interface. However FEM is still useful in the analysis of singular stress problems since FEM error can be eliminated in proportional method proposed by Nisitani[48]. This method can accurately obtain the ISSFs of bonded structure as long as the solution of reference problem is accurate enough. As we know, the reference problem has already been analytically solved by body force method[47]. This research will extend this method to the bonded axi-symmetric problems. However, the difference between plane problems and axi-symmetric problems make the application of proportional method quite difficult since the existence of non-singular stress. Thus this research will concentrate on addressing these issues and the ISSFs of different axi-symmetric problems with arbitrary material combinations will be investigated, and in addition, this method will be applied in the analysis of a practical engineering problem.

The paper is composed of total 6 chapters and organized as follows.

Chapter 1 gives the introduction of applications of composites and bonded structures in aviation industry, microelectronic packaging, and steel process equipment. Also the application and importance of bonded axi-symmetric structure are investigated. For example the application in thermal spray coating roll used in contentious annealing furnace and bonded joint of riser pipe in offshore oil equipment. With the extensive application of the technology, structural failure problems are emerging, which requires further study. Then the issues of the research on singularity in the bonded structures are

reviewed, and it's found that there are only few papers concentrated on the analysis of ISSFs for bonded axi-symmetric problems. Then the research purpose of this thesis, analysis of singular stress intensity for bonded axi-symmetric structures, is introduced.

In chapter 2, the proportional method is introduced. It is known that FEM is not suitable for the solution of bimaterial problems due to the mesh dependence of singular stress near the end of interface. However FEM is still useful in the analysis of singular stress problems since FEM error can be eliminated by applying the proportional method. This study extends the method to the bonded axi-symmetric problems. However, the difference between bonded plane problems and axi-symmetric problems make the application of proportional method quite difficult since the existence of non-singular stress due to non-zero circumferential strain ε_{θ} . Then the derivation of non-singular stress is carried on and eliminated from the stress components calculated by FEM to extend this method and break through the limitation. At last the method is verified by numerical analysis.

In chapter 3, the ISSF for the bonded cylinder is first calculated by changing the material combination systematically after the extension of the proportional method in axi-symmetric problems. And then the results are compared with that of plane strain problem and the differences were elaborated. It is found that the ISSFs of axi-symmetric problem cannot be governed by the Dundurs' parameters, therefore, the maximum and minimum values of the ISSFs are considered and shown in tables and charts in the space of Dundurs' parameters.

Chapter 4 mainly focuses on another type of axi-symmetric bonded structure, bonded pipe. The effect of inner radius on ISSF is also discussed. Generally, it is thought that the bonded pipe with an infinite inner diameter is equivalent to the plane strain problem, but actually they are quite different. Therefore, the results of bonded pipe with infinite inner diameter are compared with the plane strain problem. As is done in analysis of bonded cylinder in chapter 3, the maximum and minimum values of the ISSF are considered and shown in tables and charts in the space of Dundurs' parameters.

Chapter 5 applies the previous method to a practical engineering problem. By

using the aforementioned analysis method for bonded axi-symmetric structures, a pipe shaped hearth roll used in continuous annealing furnace for producing steel sheet is investigated. It's common to apply spraying coating on the hearth roll. However, after long term of use under high temperature and thermal shock, the spray coating, which is a sandwich bonded structure, will peel off. Thus Chapter 5 focuses on how to improve the strength of the spray coating under thermal shock. In the research of spray coating, the analysis method for bonded pipe with circumferential interface is applied in this practical engineering problem. It is found that thinner top coating always has better thermal shock resistance. And for each constant top coating thickness, the singular stress intensity reaches its minimum value when the coating thickness ratio of top coating and the bond coating $H/h \cong 2$, which is in accord with previous research for plane strain state and experimental results in engineering. Here H and h represent the top coating thickness and bond coating thickness respectively.

In the last chapter of this thesis, chapter 6, main conclusions of this study are summarized for analysis of bonded cylinder and bonded pipe, and its application in the optimum design of thermal spray coating.

1.5 Reference of Chapter 1

[1] Tessera Technologies (no date), 1iBGA. Chip Scale Packaging Solution [online]

Available from

<http://www.tessera.com/technologies/microelectronics/semiconductor>

[packaging/CSP/Pages/ubga-wire.aspx](http://www.tessera.com/technologies/microelectronics/semiconductor/packaging/CSP/Pages/ubga-wire.aspx) [Accessed 4th Jan 2012]

[2] 柳澤誠一:航空機の構造接着とシーリング技術, 工業材料, 43-10 (1995), 118-125.

[3] 柳澤誠一:航空・宇宙分野への応用, 接着, 46-12 (2002), 540-546.

[4] J. M. Anglin: Aircraft Applications, Engineered Materials Handbook Volume I Composites, ASM International (1987), 801.

[5] J. McGuire and R. Varanasi : Boeing Structural Design and Technology

- Improvements, SAMPEJ., 38-3(2002) 51-57.
- [6] Hinrichsen: A 380-Flagship Aircraft for the New Century, SAMPEJ., 38-3 (2002), 8-12.
- [8] 酒井康行: 超大型旅客機 A 380 の構造材料技術, 日本複合材料学会誌, 29-5 (2003), 171-176.
- [8] 平野英樹, 新版複合材料技術総覧, 産業技術サービスセンター, (2011), pp.155-177.
- [9]Zhao, R., Ji, Q., Carson, G, Todd, M. and Shi, Cx, 2007, Flux and underfill compatibility in a lead-free environment. [online] Available from <http://www.electroiq.com/articles/ap/print/volume-16/issue-6/features/the-back-end-process/flux-and-underfill-compatibility-in-a-lead-free-environment.html> [Accessed 4th Jan2012]
- [10] Williams, M.L., The stress around a fault or crack in dissimilar media. Bull. Seismol. Soc. America, 1959; 49: 199-208
- [11] Erdogan, F., Stress distribution in non-homogeneous elastic plane with cracks. Trans. ASME., Series E, J. Appl. Mech., 1963; 30:232-236.
- [12] Erdogan, F., Stress distribution in bonded dissimilar materials with cracks. Trans. ASME., Series E, J. Appl. Mech., 1965;32:403-410.
- [13] England, A.H., A crack between dissimilar media. Trans. ASME., Series E, J. Appl. Mech., 1965;32:400-402.
- [14] Rice, J.R. and Sih, G.C., Plane problems of cracks in dissimilar media. Trans. ASME., Series E, J. Appl. Mech., 1965;32:418-423.
- [15] Bogy, D. B., Edge Bonded Dissimilar Orthogonal Elastic Wedges under Normal and Shear Loadings, Journal of Applied Mechanics, 35 (1968), 146-154.
- [16] Bogy, D. B., On the Problem of Edge Bonded Elastic Quarter Planes Loaded at Boundary, Journal of Solids and Structures, 6 (1970), 1287-1313.
- [17]Bogy, D.B., Two Edge Bonded Elastic Wedges of Different Materials and Wedge Angles under Surface Tensions, Journal of Applied Mechanics, 38 (1971), 377-386.
- [18] Bogy, D. B., The Plane Solution for Joined Dissimilar Elastic Semistrips under Tensions, Journal of Applied Mechanics, 42 (1975), 93-98.

- [19] Bogy, D. B. , On the Problems of a Loaded Crack Terminating at a Material Interface, Bogy, D. B. , Edge Bonded Dissimilar Orthogonal Elastic Wedges under Normal and Shear Loadings, *Journal of Applied Mechanics*, 35 (1968), 146-154.
- [20] Bogy, D. B., The Plane Elastostatic Solution for a Symmetric Loaded Crack in a Strip Composite, *Int. J. Engng. Sci.*, 11 (1973), 985-966.
- [21] Dundurs, J., Discussion of edge bonded dissimilar orthogonal elastic wedges under normal and shear loading, *Journal of Applied Mechanics*, 36 (1969) 650-652.
- [22] Dundurs, J., Effect of Elastic Constants on Stress in a Composite under Plane Deformations, *Journal of Composite Materials*, 1(1967), 310.
- [23] Hein, V. L., Erdogan, F., Stress Singularity in a Two Materials Wedge, *Journal of Fracture Mechanics*, 7 (1971), 317-329.
- [24] Comninou, M., Dundurs, J., A Closed Crack Tip Terminating at an Interface, *Journal of Applied Mechanics*, 46 (1979), 97-100.
- [25] Lin, K.Y., Mar, J. W. , Finite Element Analysis of Stress Intensity Factors for Cracks at a Bimaterial Interface, *Journal of Fracture*, 12-4(1976)521-531.
- [26] Williams, M. L., The Stress around a Fault or Crack in Dissimilar Media. *Bulletin of the Seismological Society of America*, 49-2(1959), 199-204.
- [27] Williams, M. L., Stress Singularities Resulting from Various Boundary Conditions in Angular Corners of Plates in Extension, *Trans, of ASME*, 74(1952)526-528.
- [28] 服部敏雄, 坂田荘司等, 応力特異場パラメータを用いた接着界面強度評価, *日本機械学会論文集 A*, 54-499(1988), 597-603.
- [29] 服部敏雄, 応力特異場パラメータを用いた接着継手の強度評価, *日本機械学会論文集 A*, 56-523(1990), 618-623.
- [30] Williams, M. L., *Journal of Applied Mechanics*, *Trans. ASME*,24-1(1957),109.
- [31] Irwin, G. R., *Handbuch der Physik*, 6 (1988), 551, *Spring-Verlag*.
- [32] Erdogan, F., Stress Distribution in a Nonhomogeneous Elastic Plane with Cracks, *Journal of Applied Mechanics*, 30(1963), 232-238.
- [33] Erdogan, F., Stress Distribution in Bonded Dissimilar Materials with Cracks, *Journal of Applied Mechanics*, 32 (1965), 403-411.

- [34] Erdogan, F., Stress Distribution in Bonded Dissimilar Materials Containing Circular or Ring-shaped Cavities, *Journal of Applied Mechanics*, 32 (1965), 829-836.
- [35] England, A. H., A Crack between Dissimilar Media, *Journal of Applied Mechanics*, 32 (1965), 400-407.
- [36] Sih, G. C. , Rice, J. R., The Bending of Plates of Dissimilar Materials with Cracks, *Journal of Applied Mechanics*, 31 (1964), 477-483.
- [37] Rice, J.R., Sih, G. C., Plane Problems of Cracks in Dissimilar Media, *Journal of Applied Mechanics*, 32(1965), 418-423.
- [38] Muskhelishvili, N. I., Some Basic Problems of Mathematical Theory of Elasticity, 4th. ed(1963), Noordhoff.
- [39] Miyazaki, T., Noda, N. -A., Li, R., Uchikoba, T., Sano, Y., Debonding criterion for single lap joints from the intensity of singular stress field, *Journal of the Japan Institute of Electronics Packaging*, Vol. 16, No. 2 (2013), pp. 143 - 151(in Japanese).
- [40] Zhang, Y., Noda, N. -A., Wu, P., Duan, M., Corrigendum to “A mesh-independent technique to evaluate stress singularities in adhesive joints”, *International Journal of Adhesion and Adhesives*, Vol. 60, No. 774 (2015), pp. 130.
- [41] Miyazaki, T., Noda, N. -A., Uchikoba, T., Li, R., Sano, Y., Proposal of a Convenient and Accurate Method for Evaluation of Debonding Strength, *Transactions of the Society of Automotive Engineers of Japan*, Vol. 45, No. 5 (2014), pp. 895 - 901 (in Japanese).
- [42] Noda, N. -A., Miyazaki, T., Uchikoba, T., Li, R., Sano, Y., Takase, Y., Debonding strength evaluation in terms of the intensity of singular stress at the interface corner with and without fictitious crack, *International Journal of Adhesion and Adhesives*, Vol. 61 (2015), pp. 46 - 64.
- [43] Noda, N., Tsuji, T., Stress singularities in edge-bonded dissimilar wedges : Three dimensional axisymmetrical elastic problems, *Transactions of the Japan Society of Mechanical Engineers, Series A*, Vol. 58, No. 546 (1992), pp. 275 – 278 (in Japanese).
- [44] Hu, Q., Sato, Y., Watanabe, K., Dependence of stress state on elastic constants in axisymmetric dissimilar materials, *Transactions of the Japan Society of Mechanical*

Engineers, Series A, Vol. 65, No. 633 (1999), pp. 1010 – 1017 (in Japanese).

[45] Hu, Q., Watanabe, K., A study on fundamental properties of elastic parameters related to stress field for dissimilar materials, Transactions of the Japan Society of Mechanical Engineers, Series A, Vol. 69, No. 679 (2003), pp. 594 - 601 (in Japanese).

[46] Li, Y. L., Hu, S. Y., Munz, D., Yang, Y. Y., Asymtotic description of the stress field around the bond edge of a cylindrical joint, Archive of Applied Mechanics, Vol. 68, No. 7-8(1998), pp. 552-565.

[47] Chen, D.H., Nisitani, H., 1993. Intensity of singular stress field near the interface edge point of a bonded strip. Trans. JSME 59, 2682-2686

[48] Teranishi T, Nisitani H. Determination of highly accurate values of stress intensity factor in a plate of arbitrary form by FEM. Trans JSME 1999;A65:16–21.

Chapter 2 Extended proportional method and the basic reference problem for the analysis of axi-symmetric problems

2.1 Introduction

Adhesive bonding usually has been used in various industries such as automobile, marine and airplanes, for example the application in thermal spray coating roll used in contentious annealing furnace and bonded joint of riser pipe in offshore oil equipment. It has been wide used since it has number of advantages over the traditional pipe joint, such as no welding residual stress, lightweight, lower costs, easy to process and corrosion-resistant [1-3]. With the rapid growth in the use of adhesive bonding, many research works have been done to establish the evaluation criteria of this kind of adhesive joint. Arenas and Afendi et al. have researched the effect of adhesive thickness on the adhesive joint [4-6]. Sandwich adhesive specimen and its bending tests have also been studied [7]. A.A. Neves et al. studied the effect of adhesive thickness and material properties on a bonded cylinder specimen [8]. However, there are few studies on bonded axi-symmetric structure. Especially there are few studies focus on the intensity of singular stress at the end of inter face for the bonded axi-symmetric structure.

As is known to all, the improper selection of material combination will cause stress singularity at the end of interface, which may result in the failure of the joint. Thus a rational selection of material combination is crucial to the strength of the adhesive pipe joint. Chen et al. have investigated the intensity of stress singularity for arbitrary material combination in a boned strip [9]. So far only few researches have considered the stress intensity of adhesive axi-symmetric problems, and no result of arbitrary material combination has been obtained.

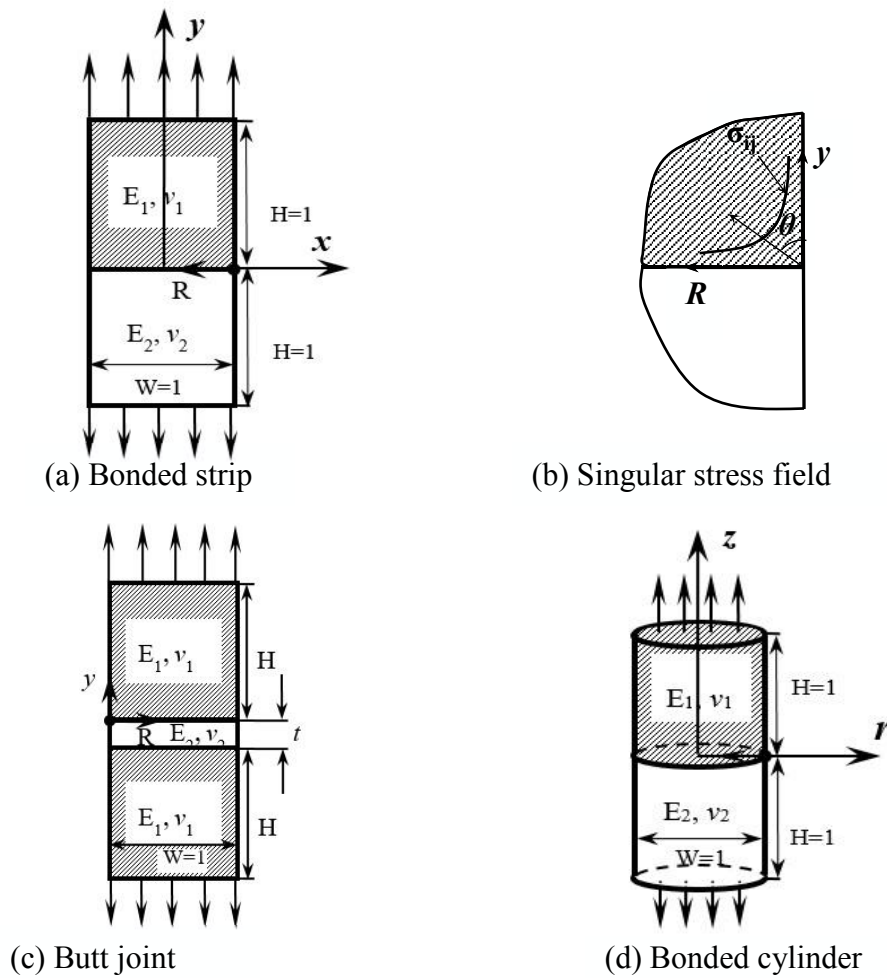


Fig. 2.1 Several bonded structures

In order to obtain the stress intensity near the corner interface, a basic result is necessary. Teranishi and Nisitani proposed a highly accurate numerical method named the proportional method (crack tip stress method) to determine the stress intensity factor of a homogenous plate shown in Fig. 2.1(a) [10]. Anyway, this method cannot be used directly into the problem of bonded axi-symmetric problems(Fig. 2.1(d)) since there are non-singular terms in stress components. In this thesis, the stress intensity will be evaluated by using an extended proportional method. Therefore this chapter will mainly focus on how to extend the method and break through the limitation in axi-symmetric problems. The difference between plane strain/stress problems and axi-symmetric

problems will be discussed. The derivation of non-singular stress will be carried on and then the improved proportional method is proposed and verified by several examples. FEM is also employed in this research.

2.2 Numerical analysis method

Fig. 2.1(a) shows the structure of the bonded strip under plain strain condition, which is the reference problem of this research. For this structure, it's known to all that the stress at the end of interface goes infinity with its singularity of $\sigma_{ij} \propto 1/R^\lambda$ (Fig. 2.1(b)), in which R is the distance from the end of interface in a dissimilar materials bonded structure. Here λ is singular index, which is the root of Eq. (2.1). As for α and β in Eq. (2.1) are known as Dundurs' parameters which are expressed by the following Eq. (2.2)[11,12], here ν is Possion's ratio and $G = E/2(1+\nu)$ is shear modulus.

$$\left[\sin^2\left(\frac{\pi}{2}\lambda\right) - \lambda^2 \right] \beta^2 + 2\lambda^2 \left[\sin^2\left(\frac{\pi}{2}\lambda\right) - \lambda^2 \right] \alpha\beta + \lambda^2 (\lambda^2 - 1) \alpha^2 + \frac{\sin^2(\pi\lambda)}{4} = 0 \quad (2.1)$$

$$\alpha = \frac{G_1(\kappa_2 + 1) - G_2(\kappa_1 + 1)}{G_1(\kappa_2 + 1) + G_2(\kappa_1 + 1)}, \quad \beta = \frac{G_1(\kappa_2 - 1) - G_2(\kappa_1 - 1)}{G_1(\kappa_2 + 1) + G_2(\kappa_1 + 1)},$$

$$\kappa_j = \begin{cases} \frac{3 - \nu_j}{1 + \nu_j} (\text{plane stress}) \\ 3 - 4\nu_j (\text{plane strain}) \end{cases} \quad (j = 1, 2) \quad (2.2)$$

The intensity of singular stress K_σ at the end of interface is then expressed as

$$K_\sigma = \lim_{R \rightarrow 0} \left[R^{1-\lambda} \times \sigma_{\theta=\pi/2}(R) \right] \quad (2.4)$$

And the dimensionless SIF F_σ is then defined as the following equation.

$$F_\sigma = \frac{K_\sigma}{\sigma(W)^{1-\lambda}} = \frac{\lim_{R \rightarrow 0} \left[R^{1-\lambda} \times \sigma_{\theta=\pi/2}(R) \right]}{\sigma(W)^{1-\lambda}} \quad (2.5)$$

The singular index λ for different material combinations are shown in Table 2.1.

Chapter 2

Table 2.1 Singular index λ for different material combinations

α	$\beta=-0.4$	$\beta=-0.3$	$\beta=-0.2$	$\beta=-0.1$	$\beta=0$	$\beta=0.1$	$\beta=0.2$	$\beta=0.3$	$\beta=0.4$
-1	0.8073	0.7205	0.6646	0.6247	0.5946				
-0.95	0.8536	0.7576	0.6975	0.6550	0.6232				
-0.9	0.9008	0.7941	0.7295	0.6845	0.6511				
-0.8	1.0000	0.8655	0.7916	0.7415	0.7048				
-0.7	1.1174	0.9348	0.8510	0.7961	0.7564				
-0.6		1.0000	0.9071	0.8480	0.8060	0.7746			
-0.5		1.0558	0.9580	0.8966	0.8532	0.8210			
-0.4		1.0913	1.0000	0.9403	0.8974	0.8655			
-0.3		1.0964	1.0276	0.9761	0.9371	0.9075			
-0.2		1.0756	1.0360	1.0000	0.9699	0.9457	0.9269		
-0.1			1.0251	1.0083	0.9921	0.9777	0.9659		
0			1.0000	1.0000	1.0000	1.0000	1.0000		
0.1			0.9269	0.9777	0.9921	1.0083	1.0251		
0.2			0.9659	0.9457	0.9699	1.0000	1.0360	1.0756	
0.3				0.9075	0.9371	0.9761	1.0276	1.0964	
0.4				0.8655	0.8974	0.9403	1.0000	1.0913	
0.5				0.8210	0.8532	0.8966	0.9580	1.0558	
0.6				0.7746	0.8060	0.8480	0.9071	1.0000	
0.7					0.7564	0.7961	0.8510	0.9348	1.1174
0.8					0.7048	0.7415	0.7916	0.8655	1.0000
0.9					0.6511	0.6845	0.7295	0.7941	0.9008
0.95					0.6232	0.6550	0.6975	0.7576	0.8536
1					0.5946	0.6247	0.6646	0.7205	0.8073

Red: $\lambda < 1$; Black: $\lambda = 1$; Green: $\lambda > 1$

The aforementioned proportional method mainly focus on the ratio of SIFs $K_{\sigma}^A / K_{\sigma}^B$, here A and B represent two different problems. Considering Eq. (2.4), the ratio of SIFs is finally controlled by the ratio of singular stress at the end of interface if the

two problems have same singular index λ , or in other words, have same material combinations. Eq. (2.6) shows the relationship of the ratios.

$$\frac{K_{\sigma}^A}{K_{\sigma}^B} = \frac{\lim_{R \rightarrow 0} \left[R^{1-\lambda_A} \times \sigma_{\theta|\theta=\pi/2}^A(R) \right]}{\lim_{R \rightarrow 0} \left[R^{1-\lambda_B} \times \sigma_{\theta|\theta=\pi/2}^B(R) \right]} = \lim_{R \rightarrow 0} \frac{R^{1-\lambda_A} \sigma_{\theta|\theta=\pi/2}^A(R)}{R^{1-\lambda_B} \sigma_{\theta|\theta=\pi/2}^B(R)} = \lim_{R \rightarrow 0} \frac{\sigma_{\theta|\theta=\pi/2}^A(R)}{\sigma_{\theta|\theta=\pi/2}^B(R)} \quad (2.6)$$

Assuming the SIFs of problems A have been analytically given in advance, while that for problem B is yet to be solved. The unknown SIF of problem B can be obtained as long as the ratio of singular stress is given. Since we cannot get the real value of singular stress, thus instead, FEM value is used. But there is still difficulty as is shown in Eq. (2.4) and Fig. 2.2, the stress near the end of interface tends to go infinite, while the stress calculated by FEM is finite and increases with decreasing the element size.

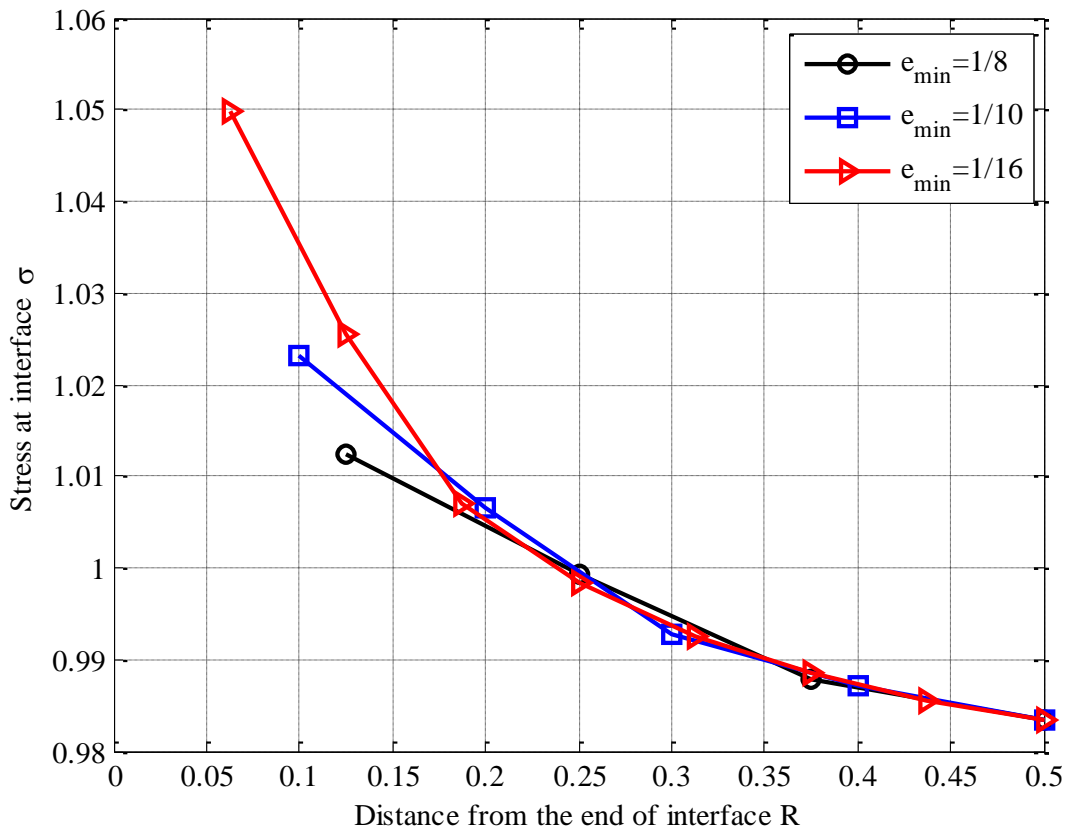


Fig. 2.2 Stress near the end of interface calculated by FEM

Although the FEM value does not equal to the real one, the ratio of FEM stress $\sigma_{ij}^A/\sigma_{ij}^B$ is still available since the error of FEM value can be eliminated if same

mesh pattern is applied to the different problems.

Take the bonded strip and butt joint shown in Fig. 2.1(a) and (c) as an example. Here we assume butt joint and bonded strip as the unknown problem and given reference problem respectively. Same material property and FE mesh pattern are applied to the two problems (Fig. 2.3).

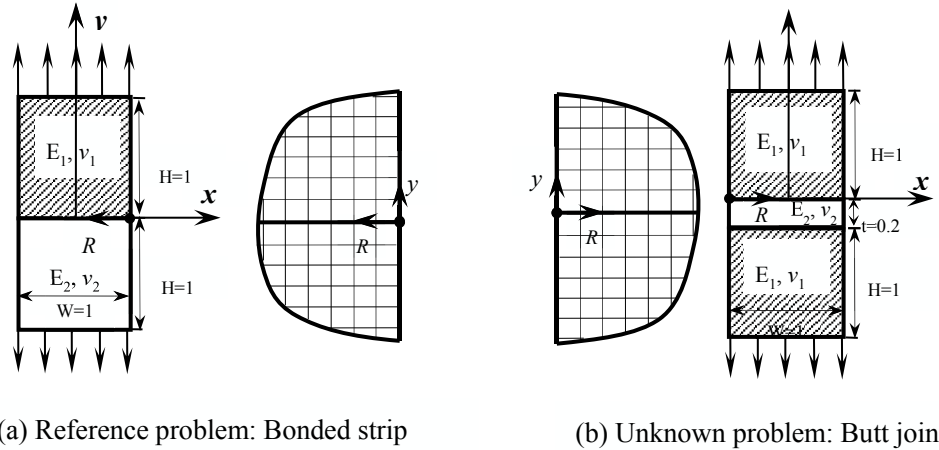


Fig. 2.3 Unknown problem and given reference problem in same FE mesh pattern

Table 2.2 shows the results of this example, as we can see, the stress near the end of interface is quite different when the mesh size is different, and it increases with decreasing the minimum element size. However the ratio of stress $\sigma_{y,FEM}^{BUTT} / \sigma_{y,FEM}^{PLT}$ almost keeps constant, which means the stress ratio is independent of mesh size. And it is also found that the stress ratio $\sigma_{y,FEM}^{BUTT} / \sigma_{y,FEM}^{PLT}$ almost keeps constant along the interface.

Table 2.2 Ratio of stress for different problems ($t/W=0.01$)

Fine mesh $e_{\min}=1/3^8$		Rough mesh $e_{\min}=1/3^4$	
R/W	$\sigma_{y,FEM}^{BUTT} \left(\frac{\sigma_{y,FEM}^{BUTT}}{\sigma_{y,FEM}^{PLT}} \right)$	R/W	$\sigma_{y,FEM}^{BUTT} \left(\frac{\sigma_{y,FEM}^{BUTT}}{\sigma_{y,FEM}^{PLT}} \right)$
0	1.640 (0.609)	0	1.246 (0.609)
$1/3^8$	1.365 (0.609)	$1/3^4$	1.306 (0.609)
$2/3^8$	1.320 (0.609)	$2/3^4$	1.001 (0.608)
$3/3^8$	1.286 (0.609)	$3/3^4$	0.975 (0.608)
$4/3^8$	1.262 (0.609)	$4/3^4$	0.956 (0.608)
$5/3^8$	1.243 (0.609)	$5/3^4$	0.942 (0.607)

Then we can assume when the element size approaches zero, which means the FEM results is equal to the real one, the ratio still keeps constant and is equal to real results. Recall Eq. (2.6), the ratio of the two different problems is given as

$$\frac{K_{\sigma}^A}{K_{\sigma}^B} = \lim_{R \rightarrow 0} \frac{\sigma_{\theta=\pi/2}^A(R)}{\sigma_{\theta=\pi/2}^B(R)} = \frac{\sigma_{ij,FEM}^A}{\sigma_{ij,FEM}^B} \quad (2.7)$$

Thus the SIF of unknown problem B can be obtained.

$$K_{\sigma}^B = K_{\sigma}^A \times \frac{\sigma_{ij,FEM}^B}{\sigma_{ij,FEM}^A} \quad (2.8)$$

Zhang et al. applied this method to the research on the effect of adhesive thickness on the interface of singular stress at the butt joint shown in Fig. 2.1(c)[13].

2.3 Intensity of singular stress for bonded strip as a reference solution

In the previous sector, it is found that the ratio of interface stress distribution can be given very accurately by using FEM. However, to obtain the intensity of singular stress, a reference solution is necessary. Chen-Nisitani [9] and Noda et. al [14] have analyzed the intensity of singular stress in a bonded strip in Fig. 2.1(a) accurately by using the body force method. Fig.2.4 and Table 2.3 indicate the results for bonded strip.

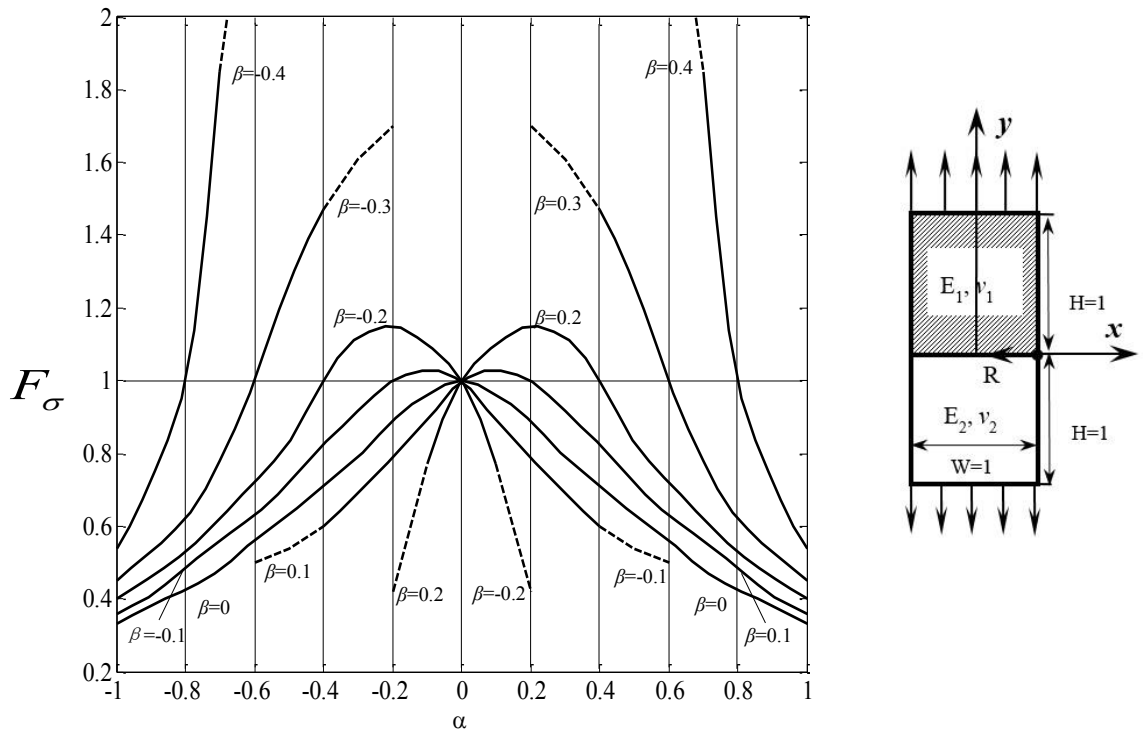


Fig. 2.4 F_σ for a bonded strip in Fig. 2.1(a)

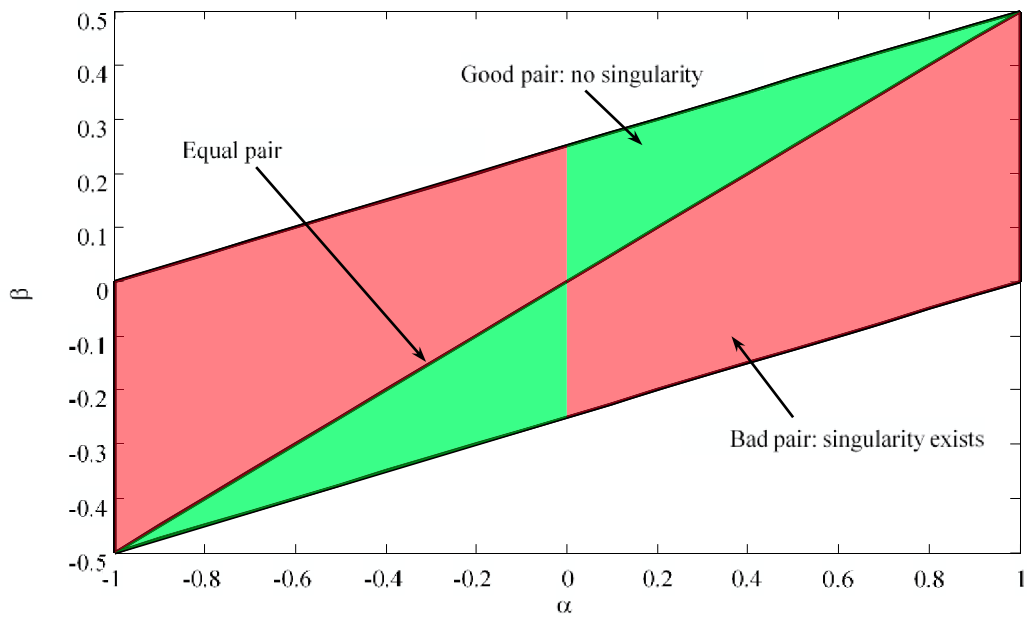


Fig. 2.5 (α, β) space

Chapter 2

Table 2.3 Dimensionless SIF F_σ at the end of interface for a bonded strip

α	$\beta=-0.4$	$\beta=-0.3$	$\beta=-0.2$	$\beta=-0.1$	$\beta=0$	$\beta=0.1$	$\beta=0.2$	$\beta=0.3$	$\beta=0.4$
-1.00	0.540	0.446	0.395	0.357	0.332	-	-	-	-
-0.90	0.726	0.534	0.456	0.412	0.381	-	-	-	-
-0.80	1.000	0.636	0.538	0.487	0.45	-	-	-	-
-0.70	1.855	0.800	0.626	0.558	0.486	-	-	-	-
-0.60	-	1.000	0.724	0.638	0.559	0.505	-	-	-
-0.50	-	1.264	0.842	0.722	0.635	0.551	-	-	-
-0.40	-	1.467	1.000	0.822	0.718	0.615	-	-	-
-0.30	-	1.609	1.118	0.913	0.796	0.697	-	-	-
-0.20	-	1.690	1.153	1.000	0.889	0.797	0.404	-	-
-0.10	-	-	1.103	1.037	0.955	0.890	0.767	-	-
0.00	-	-	1.000	1.000	1.000	1.000	1.000	-	-
0.10	-	-	0.767	0.890	0.955	1.037	1.103	-	-
0.20	-	-	0.404	0.797	0.889	1.000	1.153	1.690	-
0.30	-	-	-	0.697	0.796	0.913	1.118	1.609	-
0.40	-	-	-	0.615	0.718	0.822	1.000	1.467	-
0.50	-	-	-	0.551	0.635	0.722	0.842	1.264	-
0.60	-	-	-	0.505	0.559	0.638	0.724	1.000	-
0.70	-	-	-	-	0.486	0.558	0.626	0.800	1.855
0.80	-	-	-	-	0.450	0.487	0.538	0.636	1.000
0.90	-	-	-	-	0.381	0.412	0.456	0.534	0.726
1.00	-	-	-	-	0.332	0.357	0.395	0.446	0.540

Red: Bad pair; **Black:** Equal pair; **Green:** Good pair

It is confirmed that when $\alpha(\alpha-2\beta)>0$, the stress at the end of interface goes to infinite with different intensity depending on α, β ; stress goes to constant when $\alpha(\alpha-2\beta)=0$; stress goes to 0 when $\alpha(\alpha-2\beta)<0$, which correspond the cases of $0<\lambda<1$, $\lambda=1$ and $\lambda>1$. These three material combination conditions are thus called bad pair, equal pair and good pair. Fig. 2.5 shows the (α, β) space, in which the green area and red area

represent the good pair and bad pair respectively.

2.4 Extended proportional method in bonded axi-symmetric problems

Sector 2.3 introduced the proportional method and sector 2.4 provided the accurate solution of bonded strip as the reference problem. However, it comes to the problem when directly apply this method to axi-symmetric problem. Take bonded cylinder (Fig. 2.1(d)) as an example. Table 2.4 and Table 2.5 shows the examples of stress ratio for butt joint(Fig. 2.1(c)) and bonded cylinder (Fig. 2.1(d)) over bonded strip. Here we can see in Table 2.4, if the two problems have the same FEM mesh pattern, all the stress components ratio $\sigma_{ij}^{BUTT}/\sigma_{ij}^{PLT}$ should be consistent with each other and independent of element size when FEM is employed. While in Table 2.5, which shows the results for bonded cylinder over bonded strip, the ratios of all stress components do not consist with each other. The ratios of $\sigma_{z0,FEM}$ and $\sigma_{\theta0,FEM}$ are quite different from that of $\sigma_{r0,FEM}$ and $\tau_{rz,FEM}$. This is nature for axi-symmetric problem which needs additional discussion for the analysis.

Table 2.4 Ratio of $\sigma_{ij0,FEM}^{BUTT}/\sigma_{ij0,FEM}^{PLT}$ ($E_1 = 1000, \nu_1 = 0.25548042, E_2 = 113.79748, \nu_2 = 0.20656946$)

	$\sigma_{x0,FEM}^{BUTT}/\sigma_{x0,FEM}^{PLT}$		$\sigma_{y0,FEM}^{BUTT}/\sigma_{y0,FEM}^{PLT}$		$\sigma_{z0,FEM}^{BUTT}/\sigma_{z0,FEM}^{PLT}$		$\tau_{xy,FEM}^{BUTT}/\tau_{xy,FEM}^{PLT}$	
	Mat. 1	Mat. 2	Mat. 1	Mat. 2	Mat. 1	Mat. 2	Mat. 1	Mat. 2
$e_{\min} = 2^{-13}$	0.5253	0.5254	0.5254	0.5254	0.5254	0.5253	0.5253	0.5254
$e_{\min} = 2^{-17}$	0.5250	0.5253	0.5252	0.5252	0.5252	0.5252	0.5252	0.5253

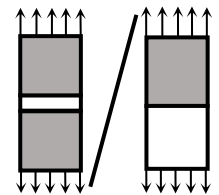
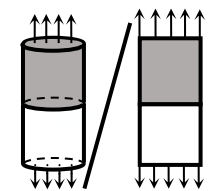


Table 2.5 Ratio of $\sigma_{ij0,FEM}^{CYL}/\sigma_{ij0,FEM}^{PLT}$ ($E_1 = 1000, \nu_1 = 0.25548042, E_2 = 113.79748, \nu_2 = 0.20656946$)

	$\sigma_{r0,FEM}^{CYL}/\sigma_{r0,FEM}^{PLT}$		$\sigma_{z0,FEM}^{CYL}/\sigma_{z0,FEM}^{PLT}$		$\sigma_{\theta0,FEM}^{CYL}/\sigma_{\theta0,FEM}^{PLT}$		$\tau_{rz,FEM}^{CYL}/\tau_{rz,FEM}^{PLT}$	
	Mat. 1	Mat. 2	Mat. 1	Mat. 2	Mat. 1	Mat. 2	Mat. 1	Mat. 2
$e_{\min} = 2^{-13}$	0.996	<u>0.992</u>	<u>0.198</u>	0.996	0.996	<u>0.991</u>	<u>0.901</u>	0.996
$e_{\min} = 2^{-17}$	0.996	<u>0.993</u>	<u>0.445</u>	0.996	0.996	<u>0.992</u>	<u>0.930</u>	0.996



For the plain strain problem shown in Fig. 2.6 which is used as the reference problem, the stress near the end of interface can be expressed as

$$\begin{cases} \sigma_i^{PLT} = \frac{K^{PLT}}{R^{1-\lambda}} (i = x, y, z) \\ \tau_{xy}^{PLT} = \frac{K^{PLT}}{R^{1-\lambda}} \end{cases} \quad (2.9)$$

Here R is the distance from the end of interface.

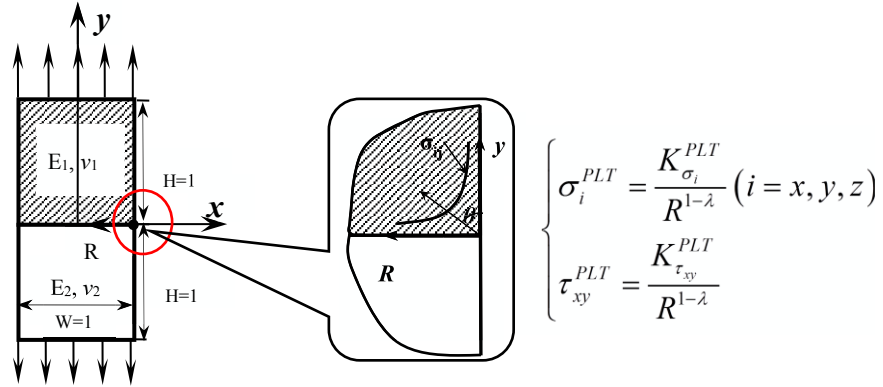


Fig. 2.6 Singular stress at the end of interface for plane strain problem

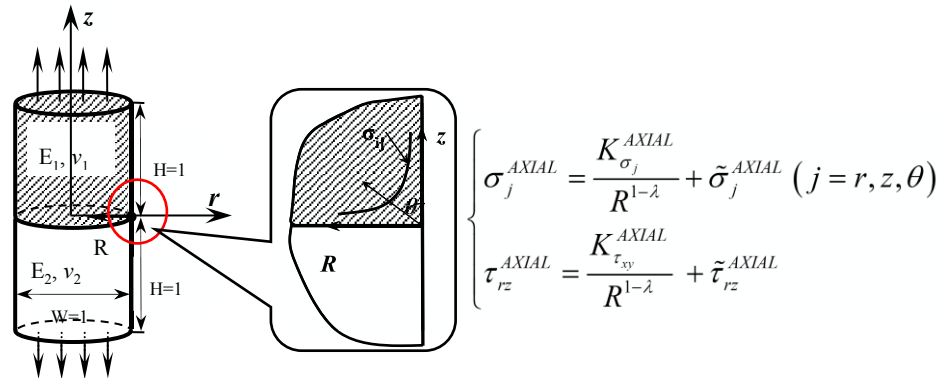


Fig. 2.7 Singular stress at the end of interface for axi-symmetric problem

And for the plain strain problem as shown in Fig. 2.7, the strain of z direction is zero. While for the axis symmetric problem, the strain of θ direction on the outer face of the pipe can be expressed as

$$\varepsilon_{\theta} = \frac{u_r}{r} \neq 0 \quad (2.10)$$

which can lead to non-zero stresses [15], and then the stress of the unknown problem shown in Fig. 2.7 is expressed as:

$$\begin{cases} \sigma_j^{AXIAL} = \frac{K_{\sigma_j}^{AXIAL}}{R^{1-\lambda}} + \tilde{\sigma}_j^{AXIAL} = \hat{\sigma}_j^{AXIAL} + \tilde{\sigma}_j^{AXIAL} \quad (j = r, z, \theta) \\ \tau_{rz}^{AXIAL} = \frac{K_{\tau_{rz}}^{AXIAL}}{R^{1-\lambda}} + \tilde{\tau}_{rz}^{AXIAL} = \hat{\tau}_{rz}^{AXIAL} + \tilde{\tau}_{rz}^{AXIAL} \end{cases} \quad (2.11)$$

In Eq. (2.11) $\hat{\sigma}_{ij}^{AXIAL}$ and $\tilde{\sigma}_{ij}^{AXIAL}$ represents the singular terms and non-singular terms of stress respectively. If the proportional method is suitable for the new unknown problem shown in Fig. 2.7, the values in Table 2.5 should have consistence when the non-singular terms is eliminated. And next how to eliminate the non-singular terms will be introduced.

At the end of interface, the first term is the singular stress, and the second terms in Eq. (2.11) have the expressions as

$$\left(\tilde{\sigma}_{r0}^{AXIAL} \right)^{\text{mat1}}, \left(\tilde{\sigma}_{z0}^{AXIAL} \right)^{\text{mat1}}, \left(\tilde{\sigma}_{\theta0}^{AXIAL} \right)^{\text{mat1}}, \left(\tilde{\tau}_{rz}^{AXIAL} \right)^{\text{mat1}} \text{ in material 1;}$$

$$\left(\tilde{\sigma}_{r0}^{AXIAL} \right)^{\text{mat2}}, \left(\tilde{\sigma}_{z0}^{AXIAL} \right)^{\text{mat2}}, \left(\tilde{\sigma}_{\theta0}^{AXIAL} \right)^{\text{mat2}}, \left(\tilde{\tau}_{rz}^{AXIAL} \right)^{\text{mat2}} \text{ in material 2.}$$

All these 8 stress components should meet the boundary conditions of bonded interface and free edge of the outer surface. And the compatibility of deformation should also be satisfied. As a result, these components should conform to the following equations.

$$\left(\tilde{\sigma}_{r0}^{AXIAL} \right)^{\text{mat1}} = \left(\tilde{\sigma}_{r0}^{AXIAL} \right)^{\text{mat2}} = \left(\tilde{\tau}_{rz}^{AXIAL} \right)^{\text{mat1}} = \left(\tilde{\tau}_{rz}^{AXIAL} \right)^{\text{mat2}} = 0 \quad (2.12)$$

$$\left(\tilde{\sigma}_{z0}^{AXIAL} \right)^{\text{mat1}} = \left(\tilde{\sigma}_{z0}^{AXIAL} \right)^{\text{mat2}} = \tilde{\sigma}_{z0}^{AXIAL} \quad (2.13)$$

$$\left(\tilde{\epsilon}_{\theta0}^{AXIAL} \right)^{\text{mat1}} = \left(\tilde{\epsilon}_{\theta0}^{AXIAL} \right)^{\text{mat2}} = \tilde{\epsilon}_{\theta0}^{AXIAL} \quad (2.14)$$

$$\left(\tilde{\epsilon}_{r0}^{AXIAL} \right)^{\text{mat1}} = \left(\tilde{\epsilon}_{r0}^{AXIAL} \right)^{\text{mat2}} = \tilde{\epsilon}_{r0}^{AXIAL} \quad (2.15)$$

Transpose Eq. (2.14), and substitute Eqs. (2.12), (2.13) into it gives

$$\left(\tilde{\epsilon}_{\theta0}^{AXIAL} \right)^{\text{mat1}} - \left(\tilde{\epsilon}_{\theta0}^{AXIAL} \right)^{\text{mat2}} = \frac{1}{E_1} \left[\left(\tilde{\sigma}_{\theta0}^{AXIAL} \right)^{\text{mat1}} - \nu_1 \left(\tilde{\sigma}_{z0}^{AXIAL} \right)^{\text{mat2}} \right] - \frac{1}{E_2} \left[\left(\tilde{\sigma}_{\theta0}^{AXIAL} \right)^{\text{mat2}} - \nu_2 \left(\tilde{\sigma}_{z0}^{AXIAL} \right)^{\text{mat2}} \right] = 0$$

Thus

$$\left(\frac{\nu_1}{E_1} - \frac{\nu_2}{E_2} \right) \tilde{\sigma}_{z0}^{AXIAL} = \frac{\left(\tilde{\epsilon}_{\theta0}^{AXIAL} \right)^{\text{mat1}}}{E_1} - \frac{\left(\tilde{\epsilon}_{\theta0}^{AXIAL} \right)^{\text{mat2}}}{E_2} \quad (2.16)$$

Similarly, for Eq. (2.15), there is

$$(\tilde{\varepsilon}_{r0}^{AXIAL})^{\text{mat1}} - (\tilde{\varepsilon}_{r0}^{AXIAL})^{\text{mat2}} = \frac{1}{E_1} \left[(\tilde{\sigma}_{r0}^{AXIAL})^{\text{mat1}} - \nu_1 (\tilde{\sigma}_{z0}^{AXIAL})^{\text{mat1}} \right] - \frac{1}{E_2} \left[(\tilde{\sigma}_{\theta 0}^{AXIAL})^{\text{mat2}} - \nu_2 (\tilde{\sigma}_{z0}^{AXIAL})^{\text{mat2}} \right] = 0$$

Substitute Eq. (2.16) into it gives

$$\frac{(\tilde{\sigma}_{\theta 0}^{AXIAL})^{\text{mat1}}}{(\tilde{\sigma}_{\theta 0}^{AXIAL})^{\text{mat2}}} = \frac{1 + \nu_2}{1 + \nu_1} \cdot \frac{E_1}{E_2} \quad (2.18)$$

From Eq. (2.16) and Eq. (2.17) we can obtain

$$\frac{(\tilde{\sigma}_{\theta 0}^{AXIAL})^{\text{mat1}}}{\tilde{\sigma}_{z0}^{AXIAL}} = - \frac{\nu_1 - \frac{E_1}{E_2} \nu_2}{\frac{\nu_1 - \nu_2}{1 + \nu_2}} \quad (2.19)$$

and

$$\frac{(\tilde{\sigma}_{\theta 0}^{AXIAL})^{\text{mat2}}}{\tilde{\sigma}_{z0}^{AXIAL}} = - \frac{\nu_2 - \frac{E_2}{E_1} \nu_1}{\frac{\nu_2 - \nu_1}{1 + \nu_2}} \quad (2.20)$$

For axis symmetric problem under cylindrical coordinate system, there is

$$\begin{cases} \varepsilon_r = \frac{\partial u_r}{\partial r} \\ \varepsilon_\theta = \frac{u_r}{r} \\ \gamma_{rz} = \frac{\partial u_r}{\partial z} + \frac{\partial u_z}{\partial r} \end{cases} \quad (2.21)$$

Recall Eq. (2.14) we can obtain:

$$\begin{aligned} (\tilde{\varepsilon}_{\theta 0}^{AXIAL})^{\text{mat1}} &= (\tilde{\varepsilon}_{\theta 0}^{AXIAL})^{\text{mat2}} = \tilde{\varepsilon}_{\theta 0}^{AXIAL} = \varepsilon_\theta = \frac{u_r}{r} \\ &= \frac{1}{E_1} \left\{ (\tilde{\sigma}_{\theta 0}^{AXIAL})^{\text{mat1}} - \nu_1 \left[(\tilde{\sigma}_{r0}^{AXIAL})^{\text{mat1}} + (\tilde{\sigma}_{z0}^{AXIAL})^{\text{mat1}} \right] \right\} = - \frac{(1 + \nu_1) \nu_1 E_2 - (1 + \nu_2) \nu_2 E_1}{(\nu_1 - \nu_2) E_1 E_2} \tilde{\sigma}_{z0}^{AXIAL} \end{aligned}$$

Thus

$$\begin{aligned} (\tilde{\sigma}_{z0}^{AXIAL})^{\text{mat1}} &= (\tilde{\sigma}_{z0}^{AXIAL})^{\text{mat2}} = \tilde{\sigma}_{z0}^{AXIAL} \\ &= - \frac{(\nu_1 - \nu_2) E_1 E_2}{(1 + \nu_1) \nu_1 E_2 - (1 + \nu_2) \nu_2 E_1} \frac{u_r}{r} = - \frac{(\nu_1 - \nu_2) E_1 E_2}{(1 + \nu_1) \nu_1 E_2 - (1 + \nu_2) \nu_2 E_1} \frac{u_{r0}^{AXIAL}}{(W/2)} \end{aligned} \quad (2.22)$$

Substituting Eq. (2.22) into Eqs. (2.19), (2.20) gives

$$(\tilde{\sigma}_{\theta 0}^{AXIAL})^{\text{mat1}} = \frac{(1 + \nu_2) (\nu_1 E_2 - \nu_2 E_1) E_1}{(1 + \nu_1) \nu_1 E_2 - (1 + \nu_2) \nu_2 E_1} \frac{u_{r0}^{AXIAL}}{(W/2)} \quad (2.23)$$

$$(\tilde{\sigma}_{\theta 0}^{AXIAL})^{\text{mat2}} = \frac{(1 + \nu_1) (\nu_1 E_2 - \nu_2 E_1) E_2}{(1 + \nu_1) \nu_1 E_2 - (1 + \nu_2) \nu_2 E_1} \frac{u_{r0}^{AXIAL}}{(W/2)} \quad (2.24)$$

And recall Eq. (2.12)

$$\left(\tilde{\sigma}_{r0}^{AXIAL}\right)^{\text{mat1}} = \left(\tilde{\sigma}_{r0}^{AXIAL}\right)^{\text{mat2}} = \left(\tilde{\tau}_{rz}^{AXIAL}\right)^{\text{mat1}} = \left(\tilde{\tau}_{rz}^{AXIAL}\right)^{\text{mat2}} = 0 \quad (2.25)$$

Until now, all eight non-singular terms have been solved since the displacement u_{r0}^{AXIAL} is independent of mesh size. And next sector will verify this result by eliminating these non-singular terms in the stress ratio

2.5 Discussion on the similarity of singular stress field and FEM model

The previous discussion verifies that the proportional method is suitable for analyzing the problem in Fig. 2.7. The intensity of singular stress for axi-symmetric problems F_{σ}^{AXIAL} can be expressed as

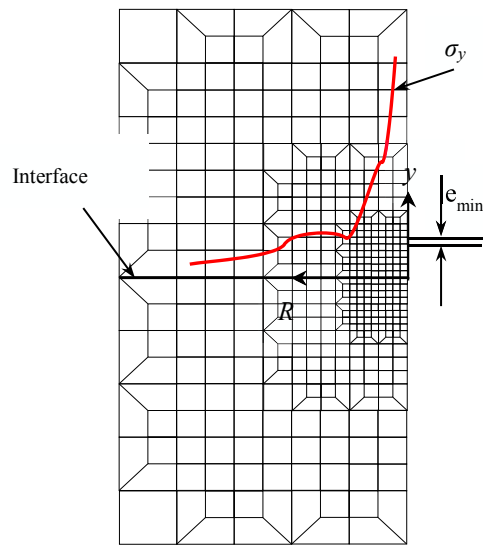
$$F_{\sigma}^{AXIAL} = \frac{\sigma_{ij,FEM}^{AXIAL} - \tilde{\sigma}_{ij}^{AXIAL}}{\sigma_{ij,FEM}^{PLT}} F_{\sigma}^{PLT} \quad (2.26)$$

in which F_{σ}^{PLT} has already been solved accurately. The only unknown parameter is the ratio of $\frac{\sigma_{ij,FEM}^{AXIAL} - \tilde{\sigma}_{ij}^{AXIAL}}{\sigma_{ij,FEM}^{PLT}}$, or the value of $\sigma_{ij,FEM}^{PLT}$, $\sigma_{ij,FEM}^{AXIAL}$ and $u_{r0,FEM}$. Therefore FEM will next be used to get the stress value at the end of interface.

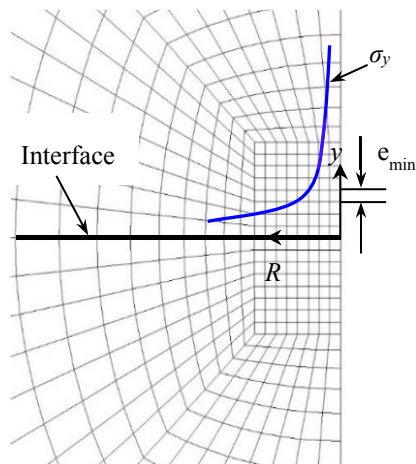
Very fine mesh will be used, since we need to get the approximate solution of singular stress as accurate as possible and verify the mesh size independence of result. We can't use same mesh size for both singular zone and other area because the limitation of hardware. Therefore the mesh with variable element size will be used. Fig. 2.8(a) show one type of mesh with fine mesh around the end of interface and rough mesh for other area. This kind of mesh pattern was often used in most previous study. However, numerical results showed unsmooth distribution for this kind of mesh since there is error caused by distortional element, especially along the interface. In this research, the mesh shown in Fig. 2.8(b) is used. There is no distortional element along the interface with all element size varies gradually on the interface, smooth stress will be obtained as a result.

Figure 2.9 and 2.10 show the FEM models of the bonded structure (same mesh pattern for both bonded strip and bonded axi-symmetric structure). In order to confirm

the mesh dependence of the solution, two mesh sizes are used, with the minimum element size of 2^{-13} and 2^{-17} respectively.



(a) Abrupt mesh



(b) Gradient mesh

Fig. 2.8 Effect of mesh pattern on the stress distribution along the interface

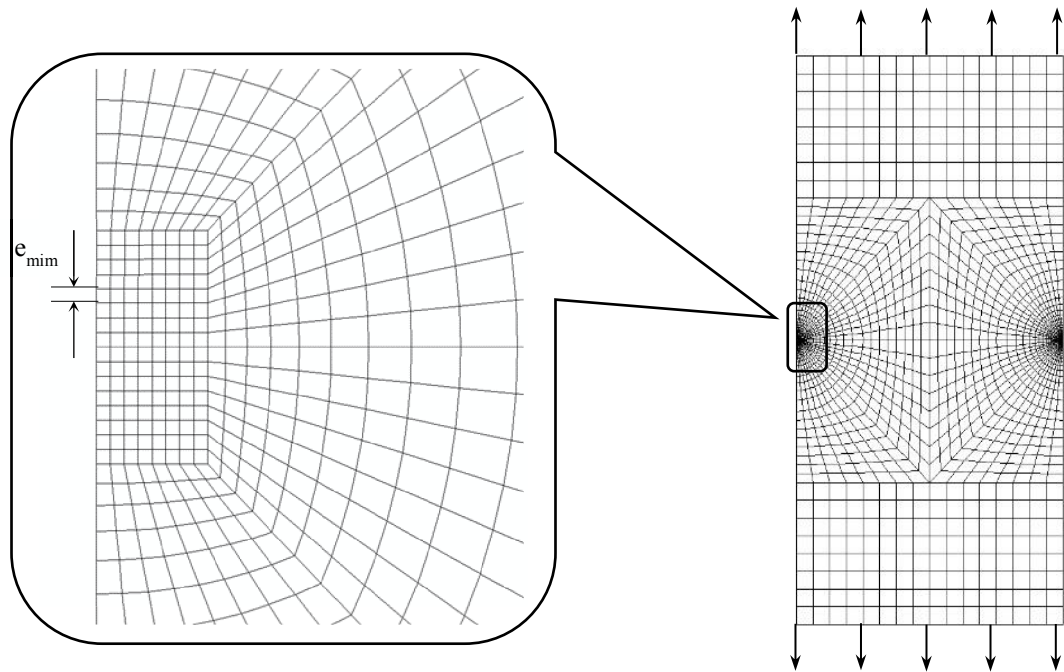


Fig. 2.9 FEM model for bonded strip

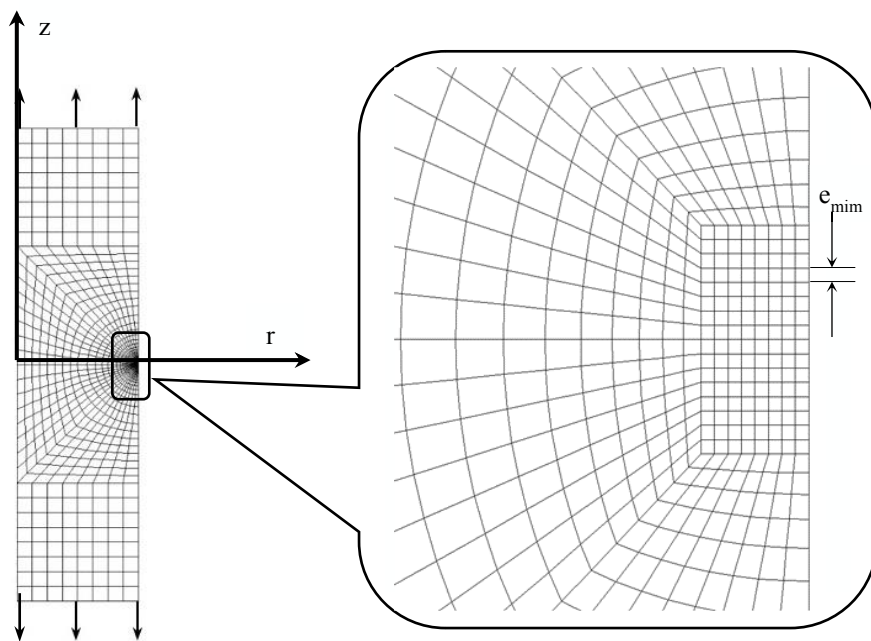


Fig. 2.10 FEM model for bonded cylinder

The linear elastic analyses are performed on the bonded plate as shown in Fig. 2.6

Chapter 2

and the bonded cylinder as shown in Fig. 2.7. The plane strain condition is assumed in the case of the bonded plate. The square four nodes elements are used in the vicinity of the interface corner edge.

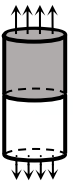

Table 2.6 shows Young's modulus E_j , Poisson's ratio ν_j , under the Dundurs' parameters $(\alpha, \beta)=(0.8,0.3)$, where the subscript j differentiates the materials 1 and 2.

Table 2.6 Material property

Material 1		Material 2		α	β	λ
E_1	E_2	ν_1	ν_2			
1000	115.57895	0.28500	0.21043	0.8	0.3	0.8655

Table 2.7 shows the stress components of the bonded cylinder and bonded plate. The stresses of bonded cylinder $\sigma_{z=0,FEM}^{CYL}$, $\tau_{rz=0,FEM}^{CYL}$ and the stresses of bonded plate $\sigma_{y=0,FEM}^{PLT}$, $\tau_{xy=0,FEM}^{PLT}$ should be continuous at the interface. However, in the FE analysis, the stresses in material 1 do not correspond with those in the material 2 since the existence of stress singularity. Therefore in this research, those stresses in materials 1 and 2 are averaged.

Table 2.7 Stress components of bonded cylinder and bonded plate

	e_{min}	$\sigma_{r=0,FEM}^{CYL}$		$\sigma_{z=0,FEM}^{CYL}$		$\sigma_{\theta\theta,FEM}^{CYL}$		$\tau_{rz=0,FEM}^{CYL}$		$u_{r=0,FEM}^{CYL}$	
		Mat.1	Mat.2	Mat.1	Mat.2	Mat.1	Mat.2	Mat.1	Mat.2	Mat.1	Mat.2
	2^{-13}	-0.7255	0.4469	2.9569		0.1816	0.5941	0.1974		-2.6802E-04	
	2^{-17}	-1.0527	0.6488	4.3011		0.5080	0.8922	0.2862		-2.6812E-04	
	e_{min}	$\sigma_{x=0,FEM}^{PLT}$		$\sigma_{y=0,FEM}^{PLT}$		$\sigma_{z=0,FEM}^{PLT}$		$\tau_{xy=0,FEM}^{PLT}$		--	
		Mat.1	Mat.2	Mat.1	Mat.2	Mat.1	Mat.2	Mat.1	Mat.2		
	2^{-13}	-0.7228	0.4454	2.9679		0.7212	0.6582	0.1966			
	2^{-17}	-1.0493	0.6467	4.3091		1.0471	0.9557	0.2853			

And then, the eliminating of the non-singular terms will be introduced. The

Chapter 2

displacement of the first node locating at the end of interface (outer surface) is

$$\begin{cases} u_r = -2.6802 \times 10^{-4}, & e_{\min} = 2^{-13} \\ u_r = -2.6812 \times 10^{-4}, & e_{\min} = 2^{-17} \end{cases}$$

And outer radius $r=0.5$, thus

$$\begin{cases} \varepsilon_{\theta} = \frac{u_r}{r} = \frac{-2.6802 \times 10^{-4}}{0.5} = -5.3604 \times 10^{-4}, & e_{\min} = 2^{-13} \\ \varepsilon_{\theta} = \frac{u_r}{r} = \frac{-2.6812 \times 10^{-4}}{0.5} = -5.3624 \times 10^{-4}, & e_{\min} = 2^{-17} \end{cases}$$

Substitute ε_{θ} into Eqs. (2.22)-(2.24), the non-singular terms can be obtained.

Table 2.8 shows the constituents of the non-singular terms. The components $\tilde{\sigma}_{ij}^{CYL}$ and $\hat{\sigma}_{ij}^{CYL}$ represent the singular terms and non-singular terms respectively.

Table 2.8 The constituents of the non-singular terms of bonded cylinder

		$\sigma_{r0,FEM}^{CYL}$		$\sigma_{z0,FEM}^{CYL}$		$\sigma_{\theta0,FEM}^{CYL}$		$\sigma_{r0,FEM}^{CYL}$	
		Mat.1	Mat.2	Mat.1	Mat.2	Mat.1	Mat.2	Mat.1	Mat.2
2^{-13}	$\hat{\sigma}_{ij}^{CYL}$	-0.7255	0.4469	2.9787		0.7238	0.6606	0.1974	
	$\tilde{\sigma}_{ij}^{CYL}$	0	0	-0.0218		-0.5422	-0.0665	0	
	$\sigma_{ij0,FEM}^{CYL}$	-0.7255=	0.4469=	2.9569=		0.1816=	0.5941=	0.1974=	
		-0.7255+0	0.4469+0	2.9787-0.0218		0.7238-0.5422	0.6606-0.0665	0.1974+0	
2^{-17}	$\hat{\sigma}_{ij}^{CYL}$	-1.0527	0.6488	4.3011		0.5080	0.8922	0.2862	
	$\tilde{\sigma}_{ij}^{CYL}$	0.0000	0.0000	-0.0218		-0.5424	-0.0666	0.0000	
	$\sigma_{ij0,FEM}^{CYL}$	-1.0527=	0.6488=	4.3011=		0.5080=	0.8922=	0.2862=	
		-1.0527+0	0.6488+0	4.3229-0.0218		1.0504-0.5424	0.9588-0.0666	0.2862+0	

As is shown in Table 2.8, the non-singular terms $\tilde{\sigma}_{ij}^{CYL}$ are mesh independent while the singular terms $\hat{\sigma}_{ij}^{CYL}$ are mesh dependent. Since the non-singular stresses are now uniquely determined by the radial displacement $u_{r0,FEM}^{CYL}$ by Eqs. (2.23-2.25), the proportional method can be applied to the bonded cylinder through the subtraction process for eliminating the non-singular stress from the stress calculated by FEM.

Chapter 2

Table 2.9 shows the stress ratio of bonded cylinder and bonded plate, both direct ratio and singular term ratio. As we can see, the stress ratios for the singular stresses $\hat{\sigma}_{ij}^{CYL} / \hat{\sigma}_{ij}^{PLT}$ (non-singular stress eliminated) are same for each stress components (4 significant digits), which verified the derivation of the non-singular terms. The result when $e_{\min}=2^{-17}$ also shows the same good consistency as that of $e_{\min}=2^{-13}$. It is also found that the ratios are almost independent of element size.

Table 2.9 Stress ratio of bonded cylinder and bonded plate

e_{\min}	$\sigma_{r0,FEM}^{CYL} / \sigma_{r0,FEM}^{PLT}$		$\sigma_{z0,FEM}^{CYL} / \sigma_{y0,FEM}^{PLT}$		$\sigma_{\theta0,FEM}^{CYL} / \sigma_{z0,FEM}^{PLT}$		$\tau_{rz0,FEM}^{CYL} / \tau_{xy0,FEM}^{PLT}$	
	Mat.1	Mat.2	Mat.1	Mat.2	Mat.1	Mat.2	Mat.1	Mat.2
2^{-13}	$\frac{-0.7255-0}{-0.7228}$ = 1.0037	$\frac{0.4469-0}{0.4454}$ = 1.0035	$\frac{2.9569-(-0.0218)}{2.9679}$ = 1.0036		$\frac{0.1816-(-0.5422)}{0.7212}$ = 1.0037	$\frac{0.5941-(-0.0665)}{0.7212}$ = 1.0036		$\frac{0.1974-0}{0.1966}$ = 1.0037
2^{-17}	$\frac{-1.0527-0}{-1.0493}$ = 1.0032	$\frac{0.6488-0}{0.6467}$ = 1.0032	$\frac{4.3011-(-0.0218)}{4.3091}$ = 1.0032		$\frac{0.5080-(-0.5424)}{1.0471}$ = 1.0032	$\frac{0.8922-(-0.0666)}{0.9557}$ = 1.0032		$\frac{0.2862-0}{0.2853}$ = 1.0032

2.6 Conclusions

The basic theory of bonded dissimilar materials structures was introduced and the key parameters and concepts in proportional method were also described. The reference problem of a bonded strip under plane strain/stress condition used in the proportional method were also introduced. The limitations of use of proportional method in bonded axi-symmetric problems was demonstrated and investigated in this chapter. Then the limitation of proportional method was broken through and an extended proportional method was proposed. Furthermore, FEM was employed to verify the derivation of non-singular terms and the reliability of the extended proportional method. The achievements of this chapter have been conclude as follows:

1. The axi-symmetric problems are different from plane strain/stress problems when directly apply the proportional method. The stress components of $\sigma_{z0,FEM}^{Axial}$ and

$\sigma_{\theta0,FEM}^{Axial}$ contain non-zero terms without singularity.

2. The non-singular terms are originated from the circumferential strain $\varepsilon_{\theta}^{Axial}$. Since this strain component is controlled by the radial displacement at the end of interface, which is mesh independent, the non-singular terms are constant composition of the stress component. To extend the proportional method to the bonded axi-symmetric problems, this terms have to be eliminated from the stress.

3. It is found that the ratios of the all stress components without non-singular stress are same with 4 significant digits, which verified the derivation of the non-singular terms. It is also found that the ratios are almost independent of element size. This means proportional method can be used to evaluate the ISSFs of bonded axi-symmetric problems.

4. Since the stress components σ_r^{AXIAL} and τ_{rz}^{AXIAL} do not contain non-singular terms, it will be easier to evaluate the ISSFs by using the ratio of these two stress components.

2.7 Reference of Chapter 2

[1] Barnes, T. A., Pashby, I. R., Joining Techniques for Aluminum Spaceframes Used in Automobiles: Part II-Adhesive Bonding and Mechanical Fasteners, Journal of Materials Processing Technology, Vol. 99 (2000), pp. 72 - 79.

[2] Higgins, A., Adhesive bonding of aircraft structures, International Journal of Adhesion and Adhesives, Vol. 20, No. 5 (2000), pp. 367 - 376.

[3] Petrie, E. M., Adhesives for the assembly of aircraft structures and components: Decades of performance improvement, with the new applications of the horizon, Metal Finishing, Vol. 106, No. 2 (2008), pp. 26 - 31.

[4] J. Arenas, J.J. Narbon, C. Alia. Optimum adhesive thickness in structural adhesives joints using statistical techniques based on Weibull distribution. International Journal of Adhesion&Adhesives, 30, 160-165 (2010).

[5] M. Afendi, T. Teramoto, H. B. Bakri. Strength prediction of epoxy adhesively bonded scarf joints of dissimilar adherends. International Journal of Adhesion&Adhesives, 31, 402-

- [6] Y. Suzuki. Transactions of the Japan Society of Mechanical Engineers, A-53, 514-522(1987).
- [7] D. Hunston, Z. Miyagi, C. Schultheisz, S. Zaghi. Mechanics of Time-Dependent Materials, 7, 71-88 (2003).
- [8] A.A. Neves, E. Courinho, A.Poitevin. Influence of joint component mechanical properties and adhesive layer thickness on stress distribution in micro-tensile bond strength specimens. Dental Materials, 25, 4-12 (2009).
- [9] Chen, D.H., Nisitani, H., 1993. Intensity of singular stress field near the interface edge point of a bonded strip. Trans. JSME 59, 2682-2686
- [10] Teranishi T, Nisitani H. Determination of highly accurate values of stress intensity factor in a plate of arbitrary form by FEM. Trans JSME 1999;A65:16–21.
- [11] D.B.Bogy: Trans. of the ASME Jour. of Applied Mech., 38(1971), 377.
- [12] D.B.Bogy: Trans. of the ASME Jour. of Applied Mech., 35(1968), 460.
- [13] Zhang Yu, Noda Nao-Aki, Takaishi Ken-Taro, Lan Xin. Effect of Adhesive Thickness on the Interface of Singular Stress at the Adhesive Dissimilar Joint. Trans. JSME Series A ,77(774), 360-372, 2011
- [14] Noda. N.A. Shirao. R.. Li. J. and Sugimoto. J.S.. Intensity of Singular Stress at the End of a Fiber under Pull-out Force. International Journal of Solids and Structures, Vol. 44. No. 13(2007). pp.4472-44911.
- [15] Li, Y. L., Hu, S. Y. Munz, D. Yang, Y. Y., Asymtotic description of the stress field around the bond edge of a cylindrical joint, Archive of Applied Mechanics, Vol. 68, No. 7-8 (1998) , pp. 552-565.

Chapter 3 Analysis on Intensity of Singular Stress for Cylinder in Comparison with Bonded Plate

3.1 Introduction

The intensities of the singular stress for the bonded plate and the butt joint under arbitrary material combinations have been investigated in the previous study[1]. Thus in this chapter, the intensity of the singular stress for the typical bonded axi-symmetric problem, bonded cylinder (Fig. 3.1(b)) in comparison with bonded plate (Fig. 3.1(a)) will be considered as well.

The previous discussion in chapter 2 verifies that the proportional method is suitable for analyzing the problem in Fig. 3.1(b). The dimensionless intensity of singular stress for axi-symmetric problems F_{σ}^{AXIAL} can be expressed as

$$F_{\sigma}^{AXIAL} = \frac{\sigma_{ij,FEM}^{AXIAL} - \tilde{\sigma}_{ij}^{AXIAL}}{\sigma_{ij,FEM}^{PLT}} F_{\sigma}^{PLT} \quad (3.1)$$

in which F_{σ}^{PLT} has already been solved accurately[3,4].

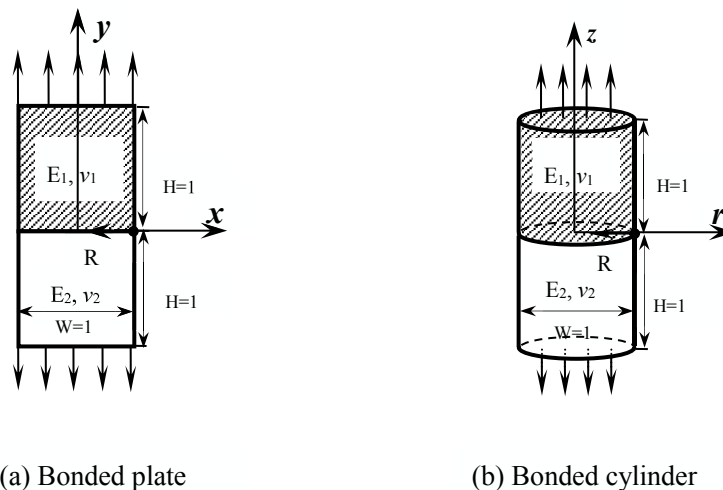


Fig. 3.1 Bonded plate and bonded cylinder

3.2 Difference of singularity between bonded plate and bonded cylinder

It's known that the singular stress field near the end of interface of two dimensional problems as shown in Figs. 3.1(a) is governed by Dundurs' parameters (α, β) uniquely regardless of the plane stress condition or the plane strain condition. However, the singular stress field of the axi-symmetric problem such as the bonded cylinder in Fig. 3.1(b) is not governed by (α, β). Fig. 3.2 and Fig 3.3 show the material combinations under the Dundurs' parameters (α, β)=(0.5,0.2). The properties of two materials are all expressed as the functions of ν_1 , which is the Poisson's ratio of material 1. Fig. 3.2 shows that ν_2 varies from 0.1177 to 0.3182 while ν_1 varies from 0 to 0.5; Fig. 3.3 shows that E_2/ E_1 varies from 0.3284 to 0.3994 while ν_1 varies from 0 to 0.5.

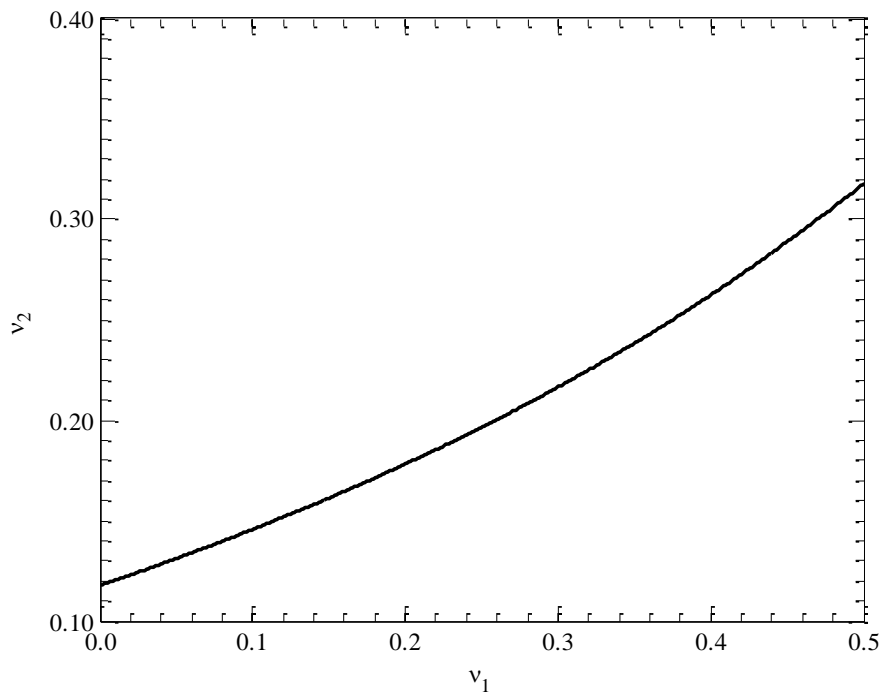


Fig. 3.2 ν_2 VS. ν_1 under (α, β)=(0.5,0.2)

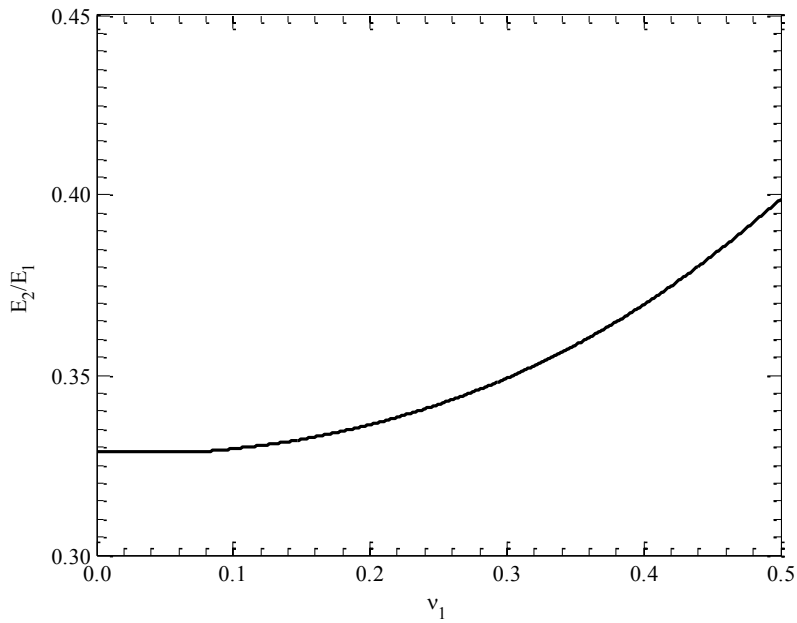


Fig. 3.3 E_2/E_1 VS. ν_1 under $(\alpha, \beta)=(0.5,0.2)$

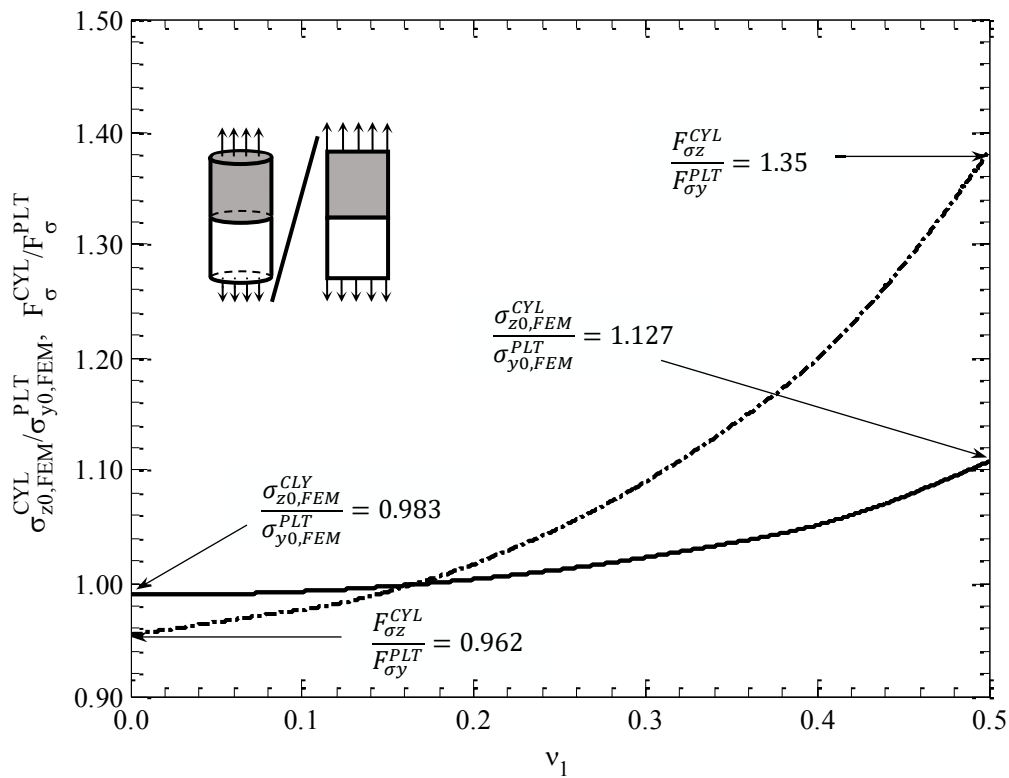


Fig. 3.4 $\sigma_{z0,FEM}^{CYL}/\sigma_{y0,FEM}^{PLT}$ and $F_{\sigma}^{CYL}/F_{\sigma}^{PLT}$ VS. ν_1 under $(\alpha, \beta)=(0.5,0.2)$

Fig. 3.4 is the stress ratio of the two problems shown in Fig. 3.1. The ratio for both direct stress and stress intensity factor varies with ν_1 . The value of $\sigma_{z0,FEM}^{CYL}/\sigma_{y0,FEM}^{PLT}$ varies

from 0.983 to 1.127 with the variation range of 14.7%, and the value of $F_{\sigma}^{CYL}/F_{\sigma}^{PLT}$ varies from 0.962 to 1.385 with the variation range of 40.3%. This means the Dundurs' parameters (α , β) cannot totally control the intensity of singular stress field close to the end of interface for a bonded cylinder.

Therefore the maximum and minimum value of $F_{\sigma}^{CYL}/F_{\sigma}^{PLT}$ should be considered.

3.3 Discussion of suitable prediction for debonding strength

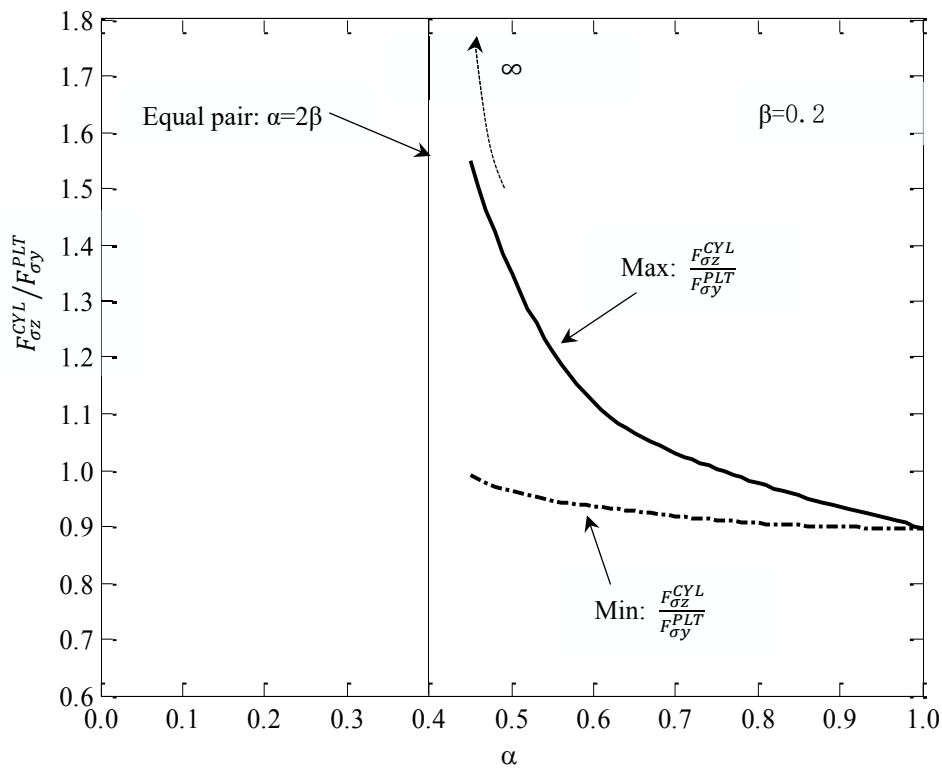


Fig. 3.5 Infinite value of $F_{\sigma}^{CYL}/F_{\sigma}^{PLT}$ at equal pair

Fig. 3.5 shows the value of $F_{\sigma_z}^{CYL}/F_{\sigma_y}^{PLT}$ when $\beta=0.2$ is fixed. Both maximum and minimum value are plotted in the figure. As is shown in the figure, the maximum value of $F_{\sigma_z}^{CYL}/F_{\sigma_y}^{PLT}$ tends to go infinite when it closes to the equal pair: $\alpha=2\beta$.

Let's check Eq. 2.22-2.24. Under the condition of $\alpha = 2\beta$, it can be found that when $\nu_1 = 0.5$, which corresponds to the maximum value of $F_{\sigma_z}^{CYL}/F_{\sigma_y}^{PLT}$, the denominators of these equations become 0 and therefore the non-singular terms diverge to ∞ . That's

the reason for the infinite value when it closes to the equal pair.

As we all know, for equal pair and good pair, there is no singularity, therefore, there is no meaning for $F_{\sigma_z}^{CYL}/F_{\sigma_y}^{PLT}$ under good and equal pair. For the prediction of debonding strength of the bonded structure in good pair and close to equal pair, the direct ratio of stress $\sigma_{z0, FEM}^{CYL}/\sigma_{y0, FEM}^{PLT}$ is more suitable. Thus for different region we use different value to evaluate the debonding strength.

The stress singularity occurs at the corner edge point for bad pair; in this case, $F_{\sigma_z}^{CYL}/F_{\sigma_y}^{PLT}$ is useful for the prediction of the debonding strength. But for equal pair and good pair, there is no singularity, Therefore, the direct ratio of stress $\sigma_{z0, FEM}^{CYL}/\sigma_{y0, FEM}^{PLT}$, which contains the influence of the non-singular stress, is more useful than the $F_{\sigma_z}^{CYL}/F_{\sigma_y}^{PLT}$ under equal and good pair. Fig. 3.6 show the maximum value of $F_{\sigma_z}^{CYL}/F_{\sigma_y}^{PLT}$ and $\sigma_{z0, FEM}^{CYL}/\sigma_{y0, FEM}^{PLT}$ in α space when $\beta=0.2$ is fixed. In bad pair region, the $F_{\sigma_z}^{CYL}/F_{\sigma_y}^{PLT}$ represents the solid line which means the suitable prediction of debonding strength, while in good pair and close to equal pair, $\sigma_{z0, FEM}^{CYL}/\sigma_{y0, FEM}^{PLT}$ should be used and represented as solid line. Fig. 3.7 shows the same situation for the results when $\beta=0.3$.

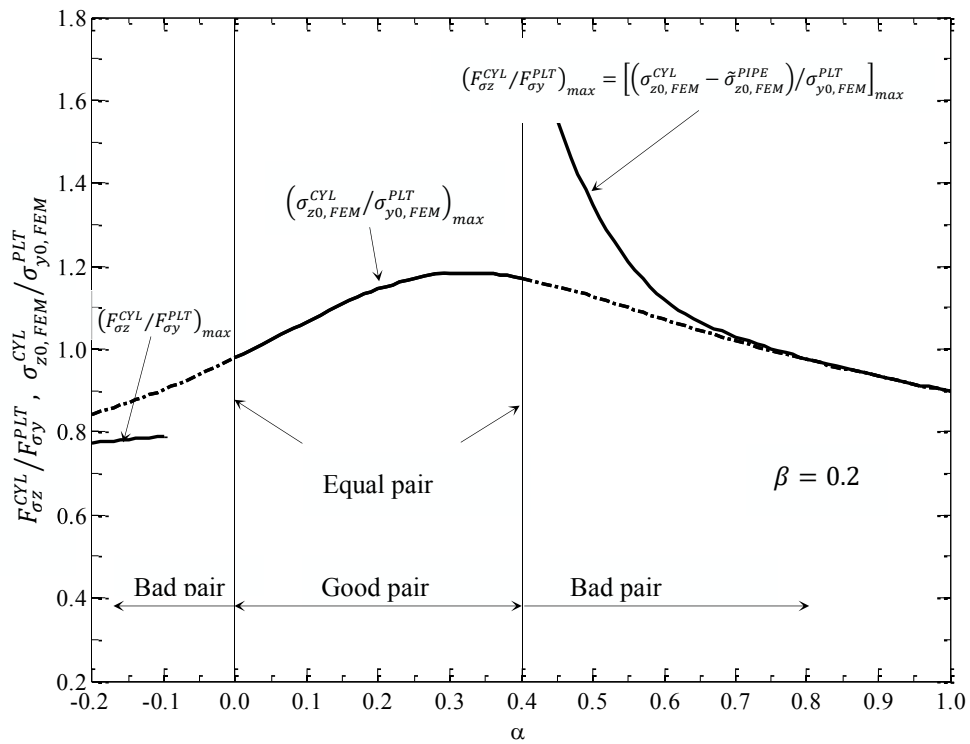


Fig. 3.6 Maximum value of $F_{\sigma}^{CYL}/F_{\sigma}^{PLT}$ and $\sigma_{z0,FEM}^{CYL}/\sigma_{y0,FEM}^{PLT}$ when $\beta=0.2$

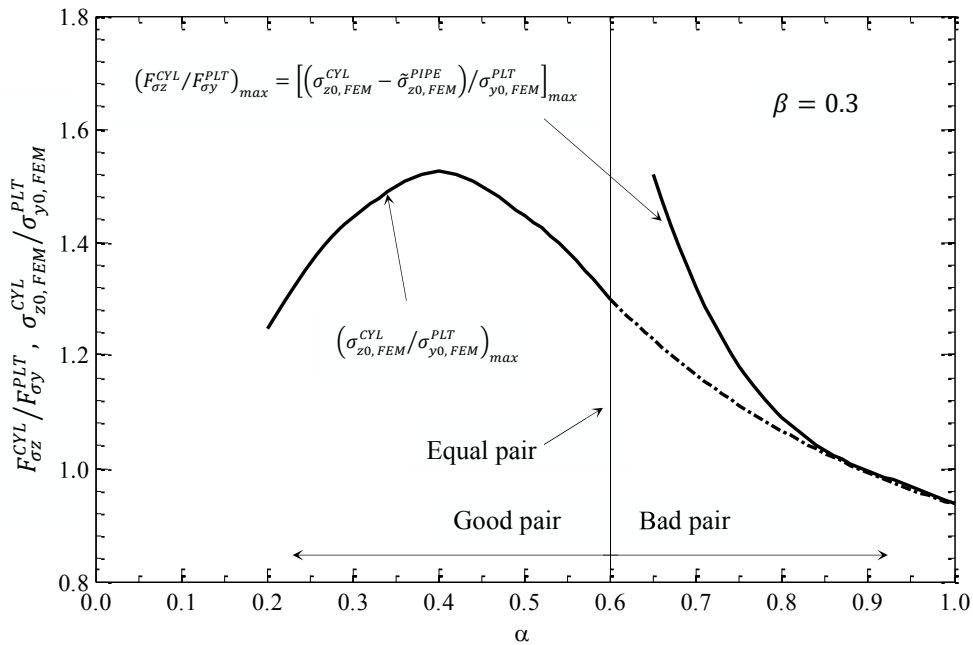


Fig. 3.7 Maximum value of $F_{\sigma}^{CYL}/F_{\sigma}^{PLT}$ and $\sigma_{z0,FEM}^{CYL}/\sigma_{y0,FEM}^{PLT}$ when $\beta=0.2$

3.4 Analysis results for bonded cylinder under arbitrary material combinations

As is discussed in the previous sector, different regions will use different value to evaluate the debonding strength. In this research, both $F_{\sigma_z}^{CYL}/F_{\sigma_y}^{PLT}$ and $\sigma_{z0,FEM}^{CYL}/\sigma_{y0,FEM}^{PLT}$ will be considered, both in maximum and minimum values. Fig. 3.8 and Fig. 3.9 show the maximum and minimum value of $F_{\sigma_z}^{CYL}/F_{\sigma_y}^{PLT}$ and $\sigma_{z0,FEM}^{CYL}/\sigma_{y0,FEM}^{PLT}$ by changing the material combinations systematically in (α, β) space.

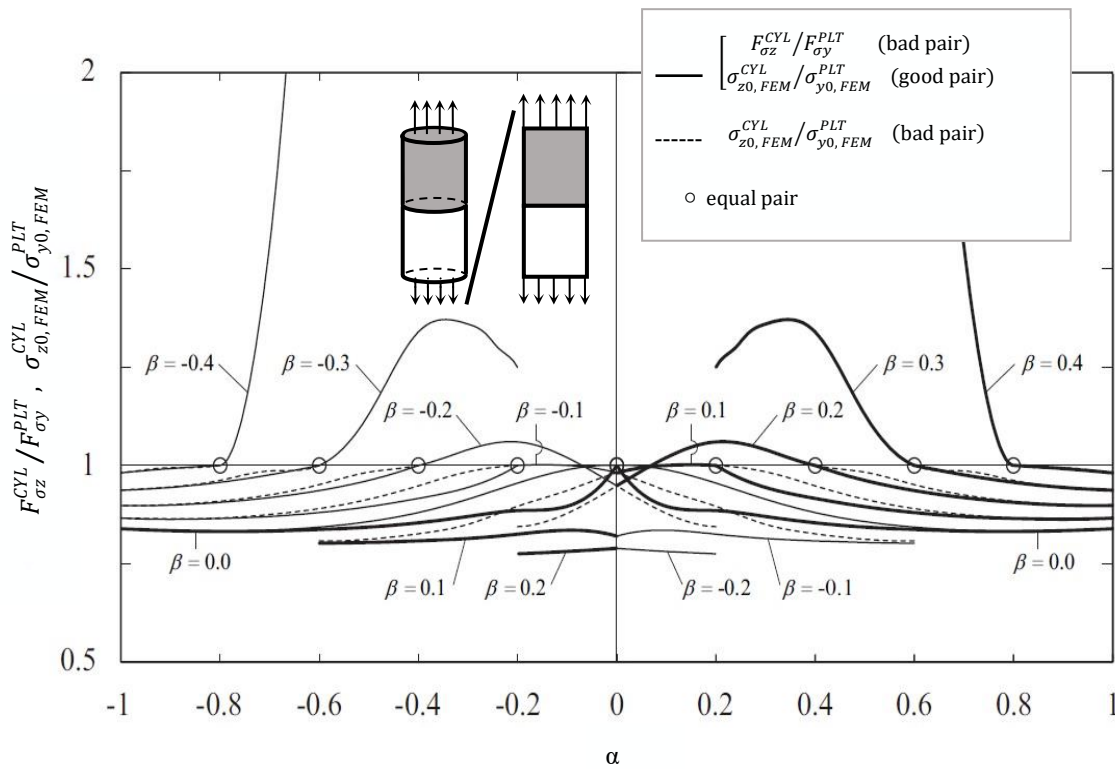


Fig. 3.8 Maximum value of $F_{\sigma_z}^{CYL}/F_{\sigma_y}^{PLT}$ and $\sigma_{z0,FEM}^{CYL}/\sigma_{y0,FEM}^{PLT}$ in (α, β) map

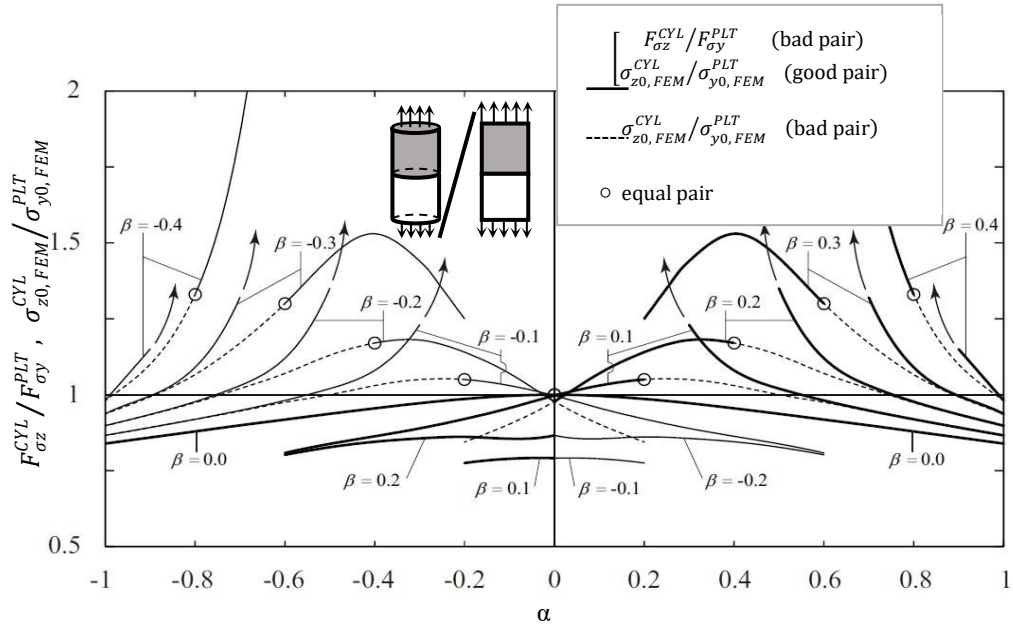


Fig. 3.9 Minimum value of $F_{\sigma}^{CYL} / F_{\sigma}^{PLT}$ and $\sigma_{z0,FEM}^{CYL} / \sigma_{y0,FEM}^{PLT}$ in (α, β) map

The results for maximum and minimum value of $F_{\sigma z}^{CYL} / F_{\sigma y}^{PLT}$ and $\sigma_{z0,FEM}^{CYL} / \sigma_{y0,FEM}^{PLT}$ are also shown in Table 3.1-Tabal 3.4.

Table 3.1 Maximum value of $F_{\sigma}^{CYL} / F_{\sigma}^{PLT}$

$\alpha \backslash \beta$	-0.2	-0.1	0	0.1	0.2	0.3	0.4	0.45
0.1	0.789	0.855	0.996					
0.2	0.775	0.861	0.986					
0.3		0.856	0.972	1.230				
0.4		0.845	0.955	1.080				
0.5		0.827	0.937	1.020	1.350			
0.6		0.802	0.918	0.981	1.120			
0.7			0.899	0.948	1.030	1.320		
0.8			0.879	0.919	0.977	1.090		
0.9			0.859	0.892	0.935	0.996	1.150	
1			0.839	0.866	0.898	0.937	0.981	0.995

Chapter 3

Table 3.2 Minimum value of $F_{\sigma}^{CYL} / F_{\sigma}^{PLT}$

$\beta \backslash \alpha$	-0.2	-0.1	0	0.1	0.2	0.3	0.4	0.45
0.1	0.781	0.835	0.896					
0.2	0.775	0.825	0.885					
0.3		0.814	0.870	0.944				
0.4		0.808	0.854	0.916				
0.5		0.804	0.843	0.895	0.962			
0.6		0.802	0.837	0.880	0.936			
0.7			0.833	0.870	0.918	0.976		
0.8			0.832	0.865	0.906	0.957		
0.9			0.834	0.863	0.899	0.944	0.992	
1			0.839	0.866	0.898	0.937	0.981	0.995

Table 3.3 Maximum value of $\sigma_{z0,FEM}^{CYL} / \sigma_{y0,FEM}^{PLT}$

$\beta \backslash \alpha$	-0.2	-0.1	0	0.1	0.2	0.3	0.4	0.45
0	0.978	0.997	1.000	0.997	0.978			
0.1	0.903	0.956	0.996	1.032	1.065			
0.2	0.844	0.920	0.986	1.052	1.145	1.246		
0.3		0.889	0.972	1.050	1.184	1.444		
0.4		0.863	0.955	1.031	1.172	1.525		
0.5		0.838	0.937	1.000	1.127	1.447		
0.6		0.808	0.918	0.975	1.071	1.299	3.117	
0.7			0.899	0.946	1.020	1.165	1.862	
0.8			0.879	0.919	0.974	1.066	1.327	2.276
0.9			0.859	0.892	0.934	0.993	1.098	1.237
1			0.839	0.866	0.898	0.937	0.981	0.995

Chapter 3

Table 3.4 Minimum value of $\sigma_{z0,FEM}^{CYL} / \sigma_{y0,FEM}^{PLT}$

$\beta \backslash \alpha$	-0.2	-0.1	0	0.1	0.2	0.3	0.4	0.45
0	0.948	0.981	1.000	0.981	0.948			
0.1	0.878	0.936	0.989	1.000	1.022			
0.2	0.844	0.898	0.955	1.000	1.060	1.246		
0.3		0.850	0.914	0.984	1.036	1.358		
0.4		0.826	0.880	0.948	1.000	1.343		
0.5		0.812	0.857	0.914	0.983	1.134		
0.6		0.808	0.843	0.890	0.951	1.000	3.117	
0.7			0.835	0.875	0.925	0.986	1.564	
0.8			0.833	0.866	0.909	0.962	1.000	2.276
0.9			0.834	0.864	0.900	0.945	0.994	1.000
1			0.839	0.866	0.898	0.937	0.981	0.995

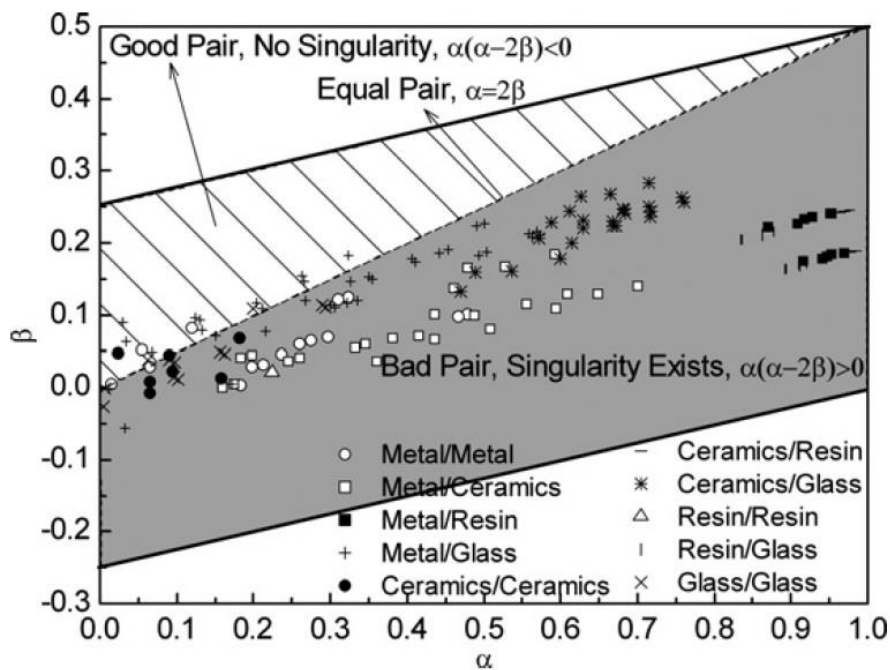


Fig. 3.10 Material combinations in (α, β) space

Fig. 3.10 shows the (α, β) for the several typical engineering materials[5]. Most of the material combinations are distributed in $0 < \beta < 0.3$. When $0 < \beta < 0.3$, the value of

$\left(\sigma_{z0, FEM}^{CYL}/\sigma_{y0, FEM}^{PLT}\right)_{max}$ is approximately located as the following range

$$0.8 \leq \frac{\sigma_{z0, FEM}^{CYL}}{\sigma_{y0, FEM}^{PLT}} \leq 1.5 \quad (3.2)$$

Comparing Fig. 3.9 with Fig. 3.8, it is found that the range of $\sigma_{z0, FEM}^{CYL}/\sigma_{y0, FEM}^{PLT}$ is quite different for different (α, β) . The differences between $\left(\sigma_{z0, FEM}^{CYL}/\sigma_{y0, FEM}^{PLT}\right)_{max}$ and

$\left(\sigma_{z0, FEM}^{CYL}/\sigma_{y0, FEM}^{PLT}\right)_{min}$ is approximately obtained as follow.

$$\frac{\left(\sigma_{z0, FEM}^{CYL}/\sigma_{y0, FEM}^{PLT}\right)_{max} - \left(\sigma_{z0, FEM}^{CYL}/\sigma_{y0, FEM}^{PLT}\right)_{min}}{\left(\sigma_{z0, FEM}^{CYL}/\sigma_{y0, FEM}^{PLT}\right)_{max} + \left(\sigma_{z0, FEM}^{CYL}/\sigma_{y0, FEM}^{PLT}\right)_{min}} \leq 0.1 \quad (3.3)$$

It is difficult to discuss whether they are governed by Dundurs' parameters (α, β) if the differences between $\left(\sigma_{z0, FEM}^{CYL}/\sigma_{y0, FEM}^{PLT}\right)_{max}$ and $\left(\sigma_{z0, FEM}^{CYL}/\sigma_{y0, FEM}^{PLT}\right)_{min}$ is large. However, since the differences between them are less than about 10% as shown in Eq. (3.3), the validity of the discussion is verified and the effect of the material combination can be put in order by Dundurs' parameters (α, β) .

3.5 Conclusion and discussion

In this chapter, the intensities of the singular stress field for the bonded cylinder was analyzed by applying the proportional method verified by last chapter. The results were calculated by changing the material combination systematically under (α, β) space. The results of bonded cylinder has been compared with that of plane strain problem and the difference was elaborated. After that, the maximum and minimum values of $F_{\sigma z}^{CYL}/F_{\sigma y}^{PLT}$ and $\sigma_{z0, FEM}^{CYL}/\sigma_{y0, FEM}^{PLT}$ are shown in tables and charts in the space of Dundurs' parameters.

The achievements of this chapter have been conclude as follows:

1. The axi-symmetric problems are different from plane strain/stress problems. The singular stress field near the end of interface of two dimensional problems as shown in Figs. 3.1(a) is governed by Dundurs' parameters (α, β) uniquely regardless of the plane stress condition or the plane strain condition. However, the singular stress field

of bonded cylinder in Fig. 3.1(b) is not governed by (α, β) . Therefore the maximum and minimum value of $F_{\sigma}^{CYL}/F_{\sigma}^{PLT}$ should be considered.

2. For bonded cylinder, the maximum value of $F_{\sigma_z}^{CYL}/F_{\sigma_y}^{PLT}$ tends to go infinite when it closes to the equal pair: $\alpha=2\beta$, and for equal pair and good pair, there is no singularity, therefore, there is no meaning for $F_{\sigma_z}^{CYL}/F_{\sigma_y}^{PLT}$ under good and equal pair. For the prediction of debonding strength of the bonded structure in good pair and close to equal pair, the direct ratio of stress $\sigma_{z0, FEM}^{CYL}/\sigma_{y0, FEM}^{PLT}$ is more suitable since it contains the influence of the non-singular stress. Thus for different region we use different value to evaluate the debonding strength.

3. For most material combinations which are distributed in $0<\beta<0.3$ under the (α, β) space, the value of $\left(\sigma_{z0, FEM}^{CYL}/\sigma_{y0, FEM}^{PLT}\right)_{max}$ is approximately located as the following range

$$0.8 \leq \frac{\sigma_{z0, FEM}^{CYL}}{\sigma_{y0, FEM}^{PLT}} \leq 1.5$$

4. Since the differences between $\left(\sigma_{z0, FEM}^{CYL}/\sigma_{y0, FEM}^{PLT}\right)_{max}$ and $\left(\sigma_{z0, FEM}^{CYL}/\sigma_{y0, FEM}^{PLT}\right)_{min}$ is less than about 10%, the effect of the material combination can be put in order by Dundurs' parameters (α, β) .

3.6 Reference of Chapter 3

[1] Zhang, Y., Noda, N. -A., Wu, P., Duan, M., Corrigendum to A mesh-independent technique to evaluate stress singularities in adhesive joints, *International Journal of Adhesion and Adhesives*, Vol. 60, No. 774 (2015), pp. 130.

[3] Chen, D.H., Nisitani, H., 1993. Intensity of singular stress field near the interface edge point of a bonded strip. *Trans. JSME* 59, 2682-2686.

[4] Noda, N.A., Shirao, R., Li, J. and Sugimoto, J.S., Intensity of Singular Stress at the End of a Fiber under Pull-out Force. *International Journal of Solids and Structures*, Vol.

Chapter 3

44. No. 13(2007). pp.4472-44911.

[5] Yuuki, R., Xu, J. -Q, Liu, J. -Q., Analysis of Stress Singularity at Interface Edge in Dissimilar Materials, Seisan Kenkyu, Vol. 44, No. 4 (1992), pp. 206 - 210

Chapter 4 Analysis on Intensity of Singular Stress for Bonded Pipe in Comparison with Bonded Plate

4.1 Introduction

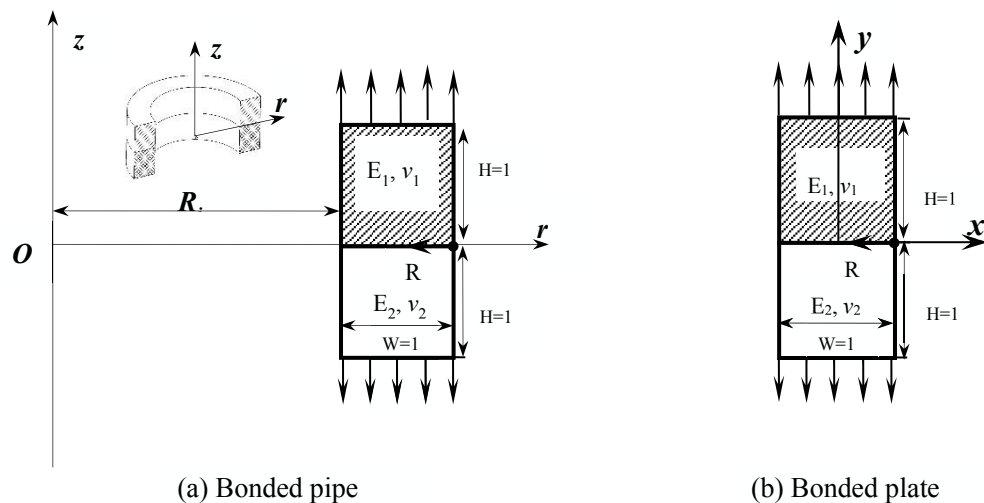


Fig. 4.1 Bonded plate and bonded pipe

The adhesive pipe joints have been widely used in offshore, steel process equipment recent years, for example the application in thermal spray coating roll used in contentious annealing furnace and bonded joint of riser pipe in offshore oil equipment, since it has number of advantages over the traditional pipe joint, such as no welding residual stress, lightweight, lower costs, easy to process and corrosion-resistant. With the rapid growth in the use of adhesive joint, many research works have been done to establish the evaluation criteria of this kind of adhesive joint. Arenas and Afendi et al. have researched the effect of adhesive thickness on the adhesive joint [1,2,5]. Sandwich adhesive specimen and its bending tests have also been studied [4]. A.A. Neves et al. studied the effect of adhesive thickness and material properties on a bonded cylinder specimen [6]. However, there are few studies on adhesive pipe. Especially there is no study focuses on the intensity of singular stress at the end of inter face for

the bonded pipe.

The intensity of singular stress near the end of interface for a bonded cylinder has been analyzed in last chapter based on the known reference bonded plate under arbitrary material combinations. And thus in this chapter, another bonded axi-symmetrical problem, bonded pipe, will be analyzed. There are many kinds of bonded pipe, while in this research the basic model of bonded pipe(Fig. 4.1(a)) will be considered. In which, R_i is the inner radius of the pipe and W is the thickness of the pipe corresponding the width of the bonded plate. Same as the previous analysis, the bonded plate is chosen as the reference problem in Fig. 4.1(b))

4.2 Effect of inner radius R_i on stress distribution of bonded pipe

Since the inner radius R_i is different for different kind of pipe, or in other words, the ratio of R_i/W is an important parameter for different pipe. Small R_i/W means pipe with thick wall (Fig. 4.2(a)) and large R_i/W represents pipe with thin wall (Fig. 4.2(b)).

To find the effect of R_i on stress distribution of bonded pipe, the width or the thickness of the pipe will be fixed as $W=1$, and the inner radius will be changed from $0 \rightarrow \infty$, which means R_i/W changes from $0 \rightarrow \infty$. The stress at the end of interface will be investigated.

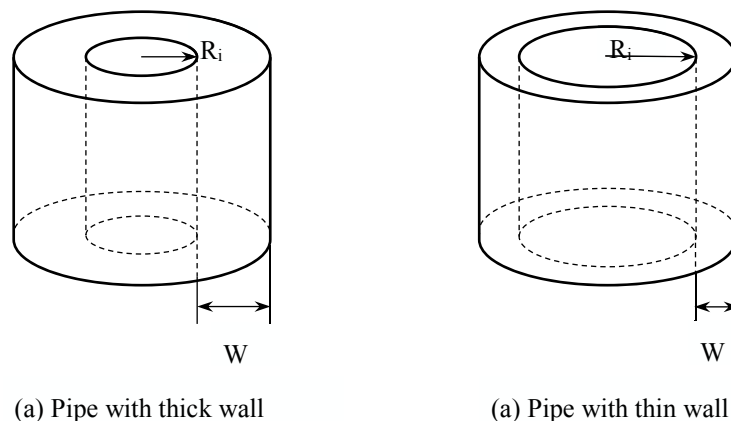


Fig. 4.2 Pipe with different thickness of wall

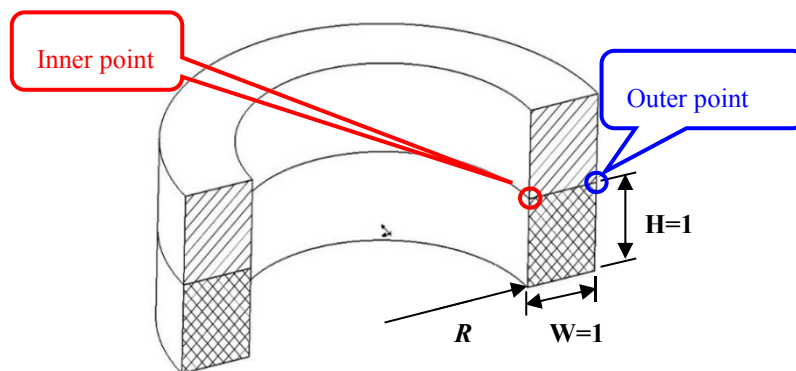


Fig. 4.3 Inner point and outer point at the end of interface for a bonded pipe

Chapter 4

Table. 4.1 Stress components at the end of interface for a bonded pipe with different inner radius

$\frac{\sigma}{R_i/W}$	Inner point				Outer point			
	$\sigma_{r0, FEM}^{PIPE}$	$\sigma_{z0, FEM}^{PIPE}$	$\sigma_{\theta0, FEM}^{PIPE}$	$\tau_{rz0, FEM}^{PIPE}$	$\sigma_{r0, FEM}^{PIPE}$	$\sigma_{z0, FEM}^{PIPE}$	$\sigma_{\theta0, FEM}^{PIPE}$	$\tau_{rz0, FEM}^{PIPE}$
0.001×2^0	-0.0840	1.7897	0.0853	-0.1187	-0.1525	3.2310	0.4123	0.2149
0.001×2^1	-0.0921	1.9518	0.1121	-0.1300	-0.1528	3.2381	0.4133	0.2154
0.001×2^2	-0.0999	2.1136	0.1349	-0.1410	-0.1534	3.2507	0.4147	0.2162
0.001×2^3	-0.1072	2.2647	0.1498	-0.1511	-0.1544	3.2708	0.4156	0.2175
0.001×2^4	-0.1136	2.3988	0.1541	-0.1601	-0.1555	3.2949	0.4123	0.2191
0.001×2^5	-0.1196	2.5255	0.1529	-0.1686	-0.1560	3.3038	0.3959	0.2198
0.001×2^6	-0.1261	2.6637	0.1619	-0.1778	-0.1543	3.2675	0.3602	0.2175
0.001×2^7	-0.1324	2.7974	0.1848	-0.1866	-0.1509	3.1921	0.3175	0.2126
0.001×2^8	-0.1370	2.8940	0.2085	-0.1930	-0.1475	3.1195	0.2849	0.2078
0.001×2^9	-0.1396	2.9507	0.2248	-0.1967	-0.1452	3.0705	0.2655	0.2046
0.001×2^{10}	-0.1410	2.9809	0.2343	-0.1987	-0.1439	3.0425	0.2552	0.2028
0.001×2^{11}	-0.1418	2.9964	0.2393	-0.1997	-0.1432	3.0276	0.2500	0.2018
0.001×2^{12}	-0.1421	3.0042	0.2420	-0.2003	-0.1428	3.0199	0.2473	0.2013
0.001×2^{13}	-0.1423	3.0081	0.2433	-0.2005	-0.1427	3.0160	0.2460	0.2010
0.001×2^{14}	-0.1424	3.0101	0.2439	-0.2007	-0.1426	3.0140	0.2453	0.2009
0.001×2^{15}	-0.1424	3.0111	0.2443	-0.2007	-0.1425	3.0130	0.2449	0.2008
0.001×2^{16}	-0.1425	3.0116	0.2444	-0.2007	-0.1425	3.0126	0.2448	0.2008
0.001×2^{17}	-0.1425	3.0118	0.2445	-0.2008	-0.1425	3.0123	0.2447	0.2008
0.001×2^{18}	-0.1425	3.0119	0.2446	-0.2008	-0.1425	3.0122	0.2447	0.2008
0.001×2^{19}	-0.1425	3.0120	0.2446	-0.2008	-0.1425	3.0121	0.2446	0.2008
0.001×2^{20}	-0.1425	3.0120	0.2446	-0.2008	-0.1425	3.0121	0.2446	0.2008
0.001×2^{21}	-0.1425	3.0120	0.2446	-0.2008	-0.1425	3.0121	0.2446	0.2008
0.001×2^{22}	-0.1425	3.0120	0.2445	-0.2008	-0.1425	3.0121	0.2445	0.2008

The inner radius R_i cannot be 0 or ∞ in FEM, thus in this research the R_i/W will

be changed as $0.001 \times 2^0 \sim 0.001 \times 2^{22}$. Table 4.1 shows the result of stress components with different R_i/W . All results are plotted in semi-log figure as shown in Figs. 4.4-4.7. As is shown in the figures, the stress components converged when $R_i/W \geq 0.001 \times 2^{16}(65.536)$, and also same stress component at inner point and outer point coincide each other when $R_i/W \geq 0.001 \times 2^{16}(65.536)$, which means the change of inner radius or R_i/W has no effect on the stress components if it is large enough.

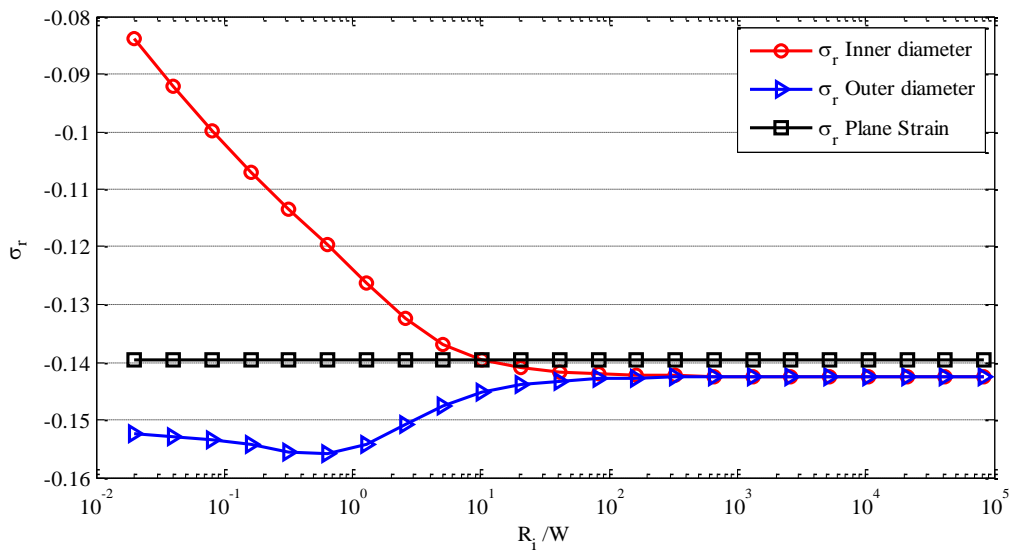


Fig. 4.4 σ_r at end of interface

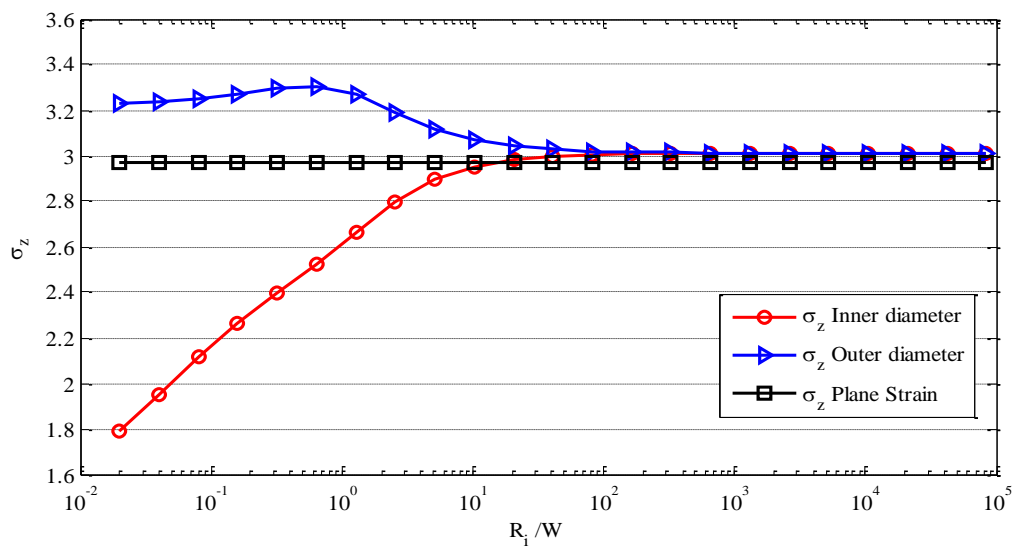


Fig. 4.5 σ_z at end of interface

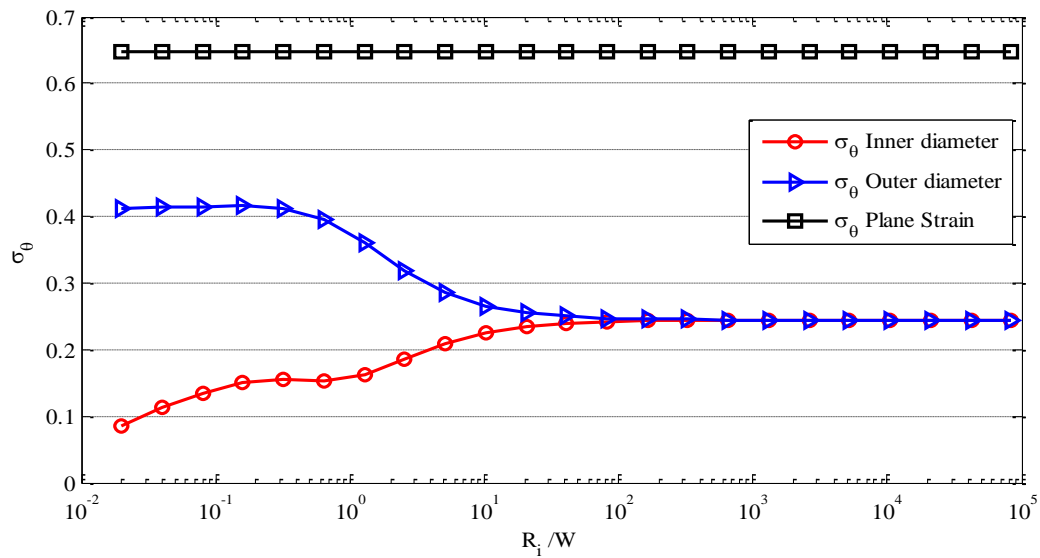


Fig. 4.6 σ_θ at end of interface

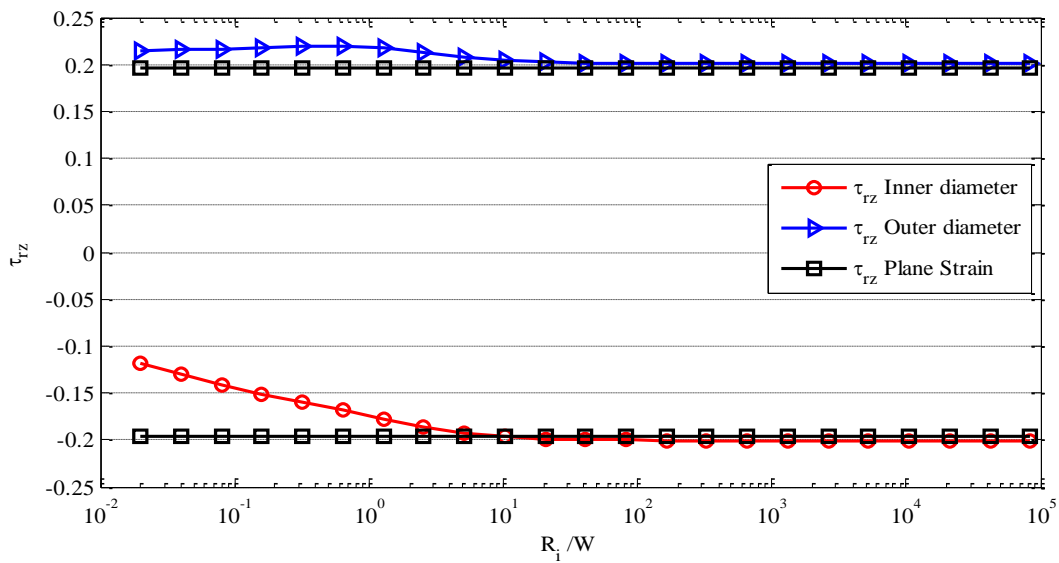


Fig. 4.7 τ_{rz} at end of interface

Usually we think the bonded pipe with a thin wall has some relationship with the plane strain problem. However, if we check the value of plane strain problem, it can be found that the bonded pipe with a large enough R_i/W doesn't coincide with plane strain problem although the two problems have same dimension. Thus the difference between these two kinds of problems will be discussed in this chapter.

4.3 Analysis method for bonded pipe

The analysis method for typical bonded axi-symmetric problem, bonded cylinder has been described in chapter 2. However, it has not been verified in the application of bonded pipe. Therefore this chapter will investigate the intensity of singular stress for a bonded pipe with the analysis method used in bonded cylinder.

As mentioned in chapter 2, the non-singular terms in the stress components for an axi-symmetric problem are expressed as

$$\begin{aligned} (\tilde{\sigma}_{z0}^{AXIAL})^{\text{mat1}} &= (\tilde{\sigma}_{z0}^{AXIAL})^{\text{mat2}} = \tilde{\sigma}_{z0}^{AXIAL} \\ &= -\frac{(v_1 - v_2)E_1E_2}{(1+v_1)v_1E_2 - (1+v_2)v_2E_1} \frac{u_r}{r} = -\frac{(v_1 - v_2)E_1E_2}{(1+v_1)v_1E_2 - (1+v_2)v_2E_1} \frac{u_{r0}^{AXIAL}}{(W/2)} \end{aligned} \quad (4.1)$$

$$(\tilde{\sigma}_{\theta 0}^{AXIAL})^{\text{mat1}} = \frac{(1+v_2)(v_1E_2 - v_2E_1)E_1}{(1+v_1)v_1E_2 - (1+v_2)v_2E_1} \frac{u_{r0}^{AXIAL}}{(W/2)} \quad (4.2)$$

$$(\tilde{\sigma}_{\theta 0}^{AXIAL})^{\text{mat2}} = \frac{(1+v_1)(v_1E_2 - v_2E_1)E_2}{(1+v_1)v_1E_2 - (1+v_2)v_2E_1} \frac{u_{r0}^{AXIAL}}{(W/2)} \quad (4.3)$$

$$(\tilde{\sigma}_{r0}^{AXIAL})^{\text{mat1}} = (\tilde{\sigma}_{r0}^{AXIAL})^{\text{mat2}} = (\tilde{\tau}_{rz}^{AXIAL})^{\text{mat1}} = (\tilde{\tau}_{rz}^{AXIAL})^{\text{mat2}} = 0 \quad (4.4)$$

Since the boundary condition at the edge surface and interface are same for both bonded pipe and bonded cylinder, Eqs. (4.1)-(4.4) can be satisfied in bonded pipe with different u_r left. An example is needed to verify the validation of derivation for non-singular terms in bonded pipe. Before that, the FEM mesh is shown in Fig. 4.8.

Same mesh pattern as used in chapter 2 is applied in the bonded pipe. Here the model with $R_i/W=105$ is used to verify the method since the stress components converge when R_i/W is large enough. Similarly, both models with the minimum element sizes 2^{-13} and 2^{-17} are used.

When $e_{\min}=2^{-13}$, the displacement of the first node locating at the end of interface (outer surface) is $u_r = -73.7971190230$

And outer radius $R_o=R_i+W=10000+1=100001$, thus

$$\varepsilon_{\theta} = \frac{u_r}{r} = \frac{-73.7971190230}{100001} = -7.3797 \times 10^{-4}$$

Substitute ε_{θ} into Eqs. (4.1)-(4.4), we have obtained the results of stress ratio of

different components as shown in Table 4.2.

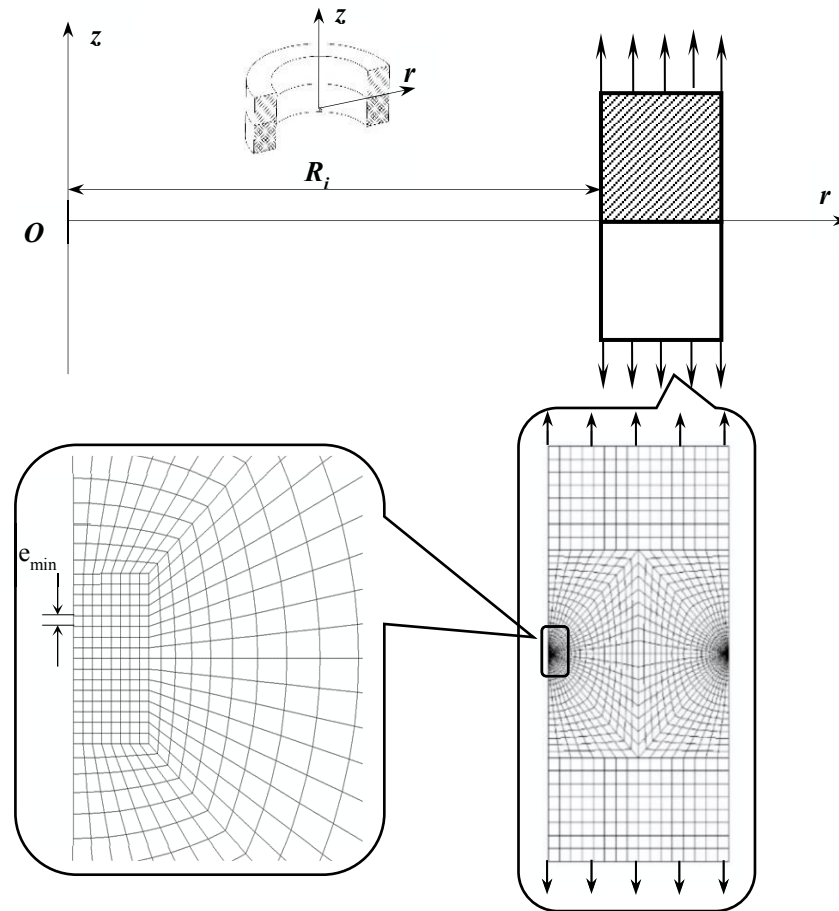


Fig. 4.8 FEM mesh for bonded pipe

It can be found that, as shown in Table 4.2, the stress ratios $\hat{\sigma}_{ij}^{PIPE} / \sigma_{ij}^{PLT}$ for the singular stresses (non-singular stress eliminated) are same for each stress components (4 significant digits), which verified the derivation of the non-singular terms for bonded pipe. Similar results has been obtained for the bonded cylinder in chapter 2.

The results for $e_{min}=2^{-17}$ also shows the same consistency and the same values of the ratio as shown in Table 4.3. It is therefore confirmed that the ratios are independent of element size; the accuracy is up to 4 decimal places.

Chapter 4

Table 4.2 FEM results for bonded pipe with $e_{\min}=2^{-13}$

$e_{\min} = 2^{-13}$	σ_x^{PLT} or σ_r^{PIPE}		σ_y^{PLT} or σ_z^{PIPE}		σ_z^{PLT} or σ_θ^{PIPE}		τ_{xy}^{PLT} or τ_{rz}^{PIPE}	
	Mat. 1	Mat. 2	Mat. 1	Mat. 2	Mat. 1	Mat. 2	Mat. 1	Mat. 2
$\hat{\sigma}_{ij}^{PIPE}$	-0.7412	0.4562	3.0313		0.6598	0.6600	0.2008	
$\tilde{\sigma}_{ij}^{PIPE}$	0.0000	0.0000	-0.0193		-0.7428	-0.0880	0.0000	
$\sigma_{ij}^{PIPE} = \hat{\sigma}_{ij}^{PIPE} + \tilde{\sigma}_{ij}^{PIPE}$	-0.7412	0.4562	3.0120		-0.0830	0.5720	0.2008	
σ_{ij}^{PLT}	-0.72612	0.44693	2.9699		0.64653	0.64654	0.1967	
$\hat{\sigma}_{ij}^{PIPE} / \sigma_{ij}^{PLT}$	1.0207	1.0207	1.0207		1.0206	1.0207	1.0207	
$\tilde{\sigma}_{ij}^{PIPE} / \sigma_{ij}^{PLT}$	0.0000	0.0000	-0.0065		-1.1489	-0.1360	0.0000	
$\sigma_{ij}^{PIPE} / \sigma_{ij}^{PLT}$	1.0207+ (0.0000)	1.0207+ (0.0000)	1.0207+ (-0.0065)		1.0206+ (-1.1489)	1.0207+ (-0.1360)	1.0207+ (0.0000)	

Table 4.3 FEM results for bonded pipe with $e_{\min}=2^{-17}$

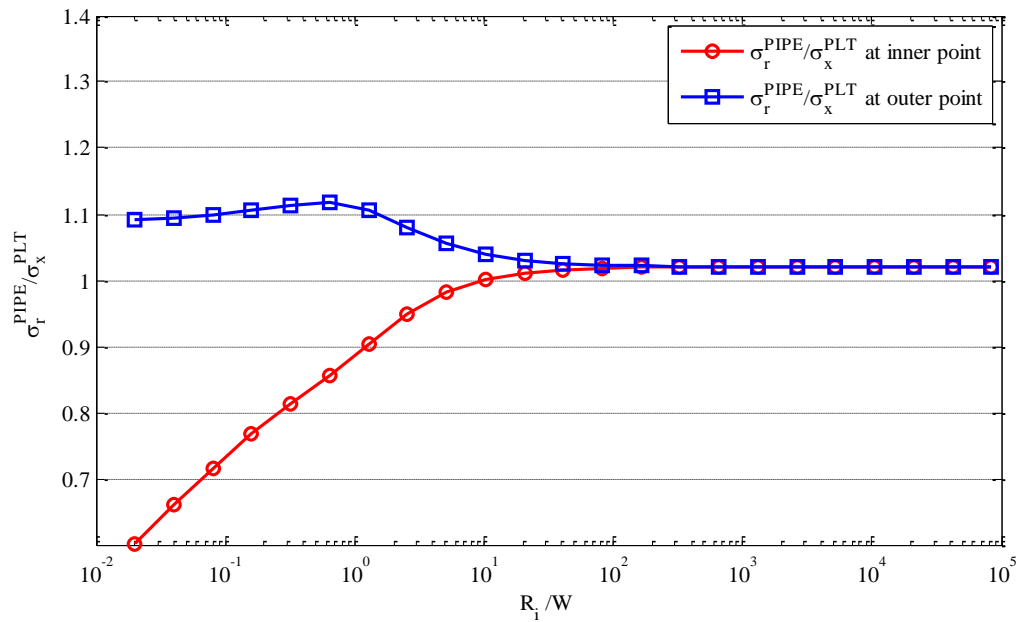
$e_{\min} = 2^{-17}$	σ_x^{PLT} or σ_r^{PIPE}		σ_y^{PLT} or σ_z^{PIPE}		σ_z^{PLT} or σ_θ^{PIPE}		τ_{xy}^{PLT} or τ_{rz}^{PIPE}	
	Mat. 1	Mat. 2	Mat. 1	Mat. 2	Mat. 1	Mat. 2	Mat. 1	Mat. 2
$\hat{\sigma}_{ij}^{PIPE}$	-1.0756	0.6622	4.3999		0.9578	0.9579	0.2913	
$\tilde{\sigma}_{ij}^{PIPE}$	0.0000	0.0000	-0.0193		-0.7427	-0.0879	0.0000	
$\sigma_{ij}^{PIPE} = \hat{\sigma}_{ij}^{PIPE} + \tilde{\sigma}_{ij}^{PIPE}$	-1.0756	0.6622	4.3806		0.2151	0.8700	0.2913	
σ_{ij}^{PLT}	-1.0542	0.64898	4.3120		0.93869	0.93876	0.2855	
$\hat{\sigma}_{ij}^{PIPE} / \sigma_{ij}^{PLT}$	1.0204	1.0204	1.0204		1.0203	1.0204	1.0204	
$\tilde{\sigma}_{ij}^{PIPE} / \sigma_{ij}^{PLT}$	0.0000	0.0000	-0.0044		-3.4535	-0.1011	0.0000	
$\sigma_{ij}^{PIPE} / \sigma_{ij}^{PLT}$	1.0204+ (0.0000)	1.0204+ (0.0000)	1.0204+ (-0.0044)		1.0203+ (-3.4535)	1.0204+ (-0.1011)	1.0204+ (0.0000)	

Since the results verified that the proportional method (crack tip stress method) is available for the problem in this research. Then the intensity of singular stress in bonded pipe F_σ^{PIPE} can be expressed as

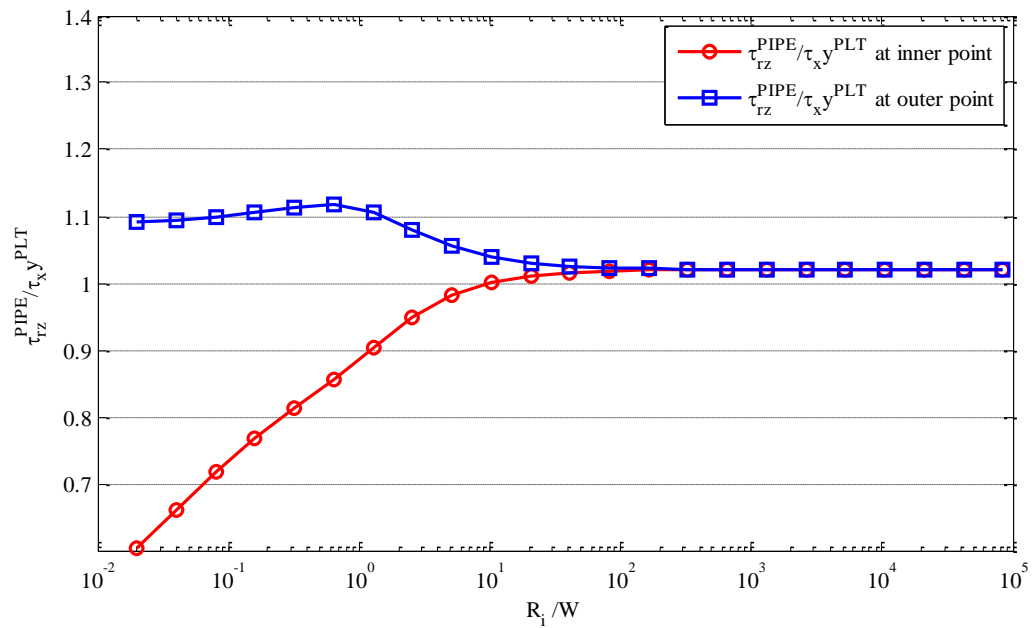
$$F_\sigma^{PIPE} = \frac{\sigma_{ij,FEM}^{PIPE} - \tilde{\sigma}_{ij,FEM}^{PIPE}}{\sigma_{ij,FEM}^{PLT}} F_\sigma^{PLT} \quad (4.5)$$

As expressed in Eq. 4.4, the stress components σ_r^{PIPE} and τ_{rz}^{PIPE} do not contain non-singular terms, it will be easier to evaluated the ISSFs by using the ratio of these two stress components. Table 4.4 shows the results of stress ratio for bonded plate and bonded pipe with different inner radius. And all data were plotted in Fig. 4.9. From

Table 4.4 and Fig. 4.9 it can be found that the stress ratio converges when $R_i/W \geq 0.001 \times 2^{16}$.



(a) $\sigma_r^{PIPE}/\sigma_x^{PLT}$



(b) $\tau_{rz}^{PIPE}/\tau_{xy}^{PLT}$

Fig. 4.9 Stress ratio for bonded pipe with different inner radius and bonded plate

Chapter 4

Table 4.4 Stress ratio for bonded plate and bonded pipe with different inner radius

Items R_i/W	Inner point				Outer point			
	$\sigma_{r0,FEM}^{PIPE}$	$\frac{\sigma_{r0,FEM}^{PIPE}}{\sigma_{x0,FEM}^{PLT}}$	$\tau_{rz0,FEM}^{PIPE}$	$\frac{\tau_{rz0,FEM}^{PIPE}}{\tau_{xy0,FEM}^{PLT}}$	$\sigma_{r0,FEM}^{PIPE}$	$\frac{\sigma_{r0,FEM}^{PIPE}}{\sigma_{x0,FEM}^{PLT}}$	$\tau_{rz0,FEM}^{PIPE}$	$\frac{\tau_{rz0,FEM}^{PIPE}}{\tau_{xy0,FEM}^{PLT}}$
0.02	-0.0840	0.6015	-0.1187	0.6032	-0.1525	1.0925	0.2149	1.0924
0.04	-0.0921	0.6596	-0.1300	0.6608	-0.1528	1.0949	0.2154	1.0948
0.08	-0.0999	0.7159	-0.1410	0.7167	-0.1534	1.0991	0.2162	1.0990
0.16	-0.1072	0.7678	-0.1511	0.7682	-0.1544	1.1059	0.2175	1.1058
0.32	-0.1136	0.8136	-0.1601	0.8138	-0.1555	1.1142	0.2191	1.1141
0.64	-0.1196	0.8568	-0.1686	0.8569	-0.1560	1.1175	0.2198	1.1174
1.28	-0.1261	0.9036	-0.1778	0.9037	-0.1543	1.1057	0.2175	1.1056
2.56	-0.1324	0.9487	-0.1866	0.9487	-0.1509	1.0807	0.2126	1.0807
5.12	-0.1370	0.9812	-0.1930	0.9812	-0.1475	1.0566	0.2078	1.0565
10.24	-0.1396	1.0002	-0.1967	1.0002	-0.1452	1.0402	0.2046	1.0402
20.48	-0.1410	1.0103	-0.1987	1.0103	-0.1439	1.0309	0.2028	1.0309
40.96	-0.1418	1.0155	-0.1997	1.0155	-0.1432	1.0259	0.2018	1.0259
81.92	-0.1421	1.0181	-0.2003	1.0181	-0.1428	1.0233	0.2013	1.0233
163.84	-0.1423	1.0194	-0.2005	1.0194	-0.1427	1.0220	0.2010	1.0220
327.68	-0.1424	1.0200	-0.2007	1.0200	-0.1426	1.0214	0.2009	1.0214
655.36	-0.1424	1.0204	-0.2007	1.0204	-0.1425	1.0210	0.2008	1.0210
1310.72	-0.1425	1.0205	-0.2007	1.0205	-0.1425	1.0209	0.2008	1.0209
2621.44	-0.1425	1.0206	-0.2008	1.0206	-0.1425	1.0208	0.2008	1.0208
5242.88	-0.1425	1.0207	-0.2008	1.0207	-0.1425	1.0207	0.2008	1.0207
10485.76	-0.1425	1.0207	-0.2008	1.0207	-0.1425	1.0207	0.2008	1.0207
20971.52	-0.1425	1.0207	-0.2008	1.0207	-0.1425	1.0207	0.2008	1.0207
41943.04	-0.1425	1.0207	-0.2008	1.0207	-0.1425	1.0207	0.2008	1.0207
83886.08	-0.1425	1.0207	-0.2008	1.0207	-0.1425	1.0207	0.2008	1.0207
Plate	$\sigma_{x0,FEM}^{PLT} = -0.13959$		$\tau_{xy0,FEM}^{PLT} = -0.19671$		$\sigma_{x0,FEM}^{PLT} = -0.13959$		$\tau_{xy0,FEM}^{PLT} = 0.19671$	

Therefore this research will mainly focus on the situation with large R_i/W , which

means the bonded pipe with very thin wall. And R_i/W is assumed as 10^5 in this research, so that we can compare the result with the plane strain problem, and also make a general contribution for the understanding of bonded pipe.

4.4 Difference of singularity between bonded plate and bonded pipe

It has been discussed that the singular stress field near the end of interface of a bonded cylinder can not be governed by Dundurs' parameters (α, β) uniquely, while the bonded plate under the plane stress condition or the plane strain condition can be controlled by these parameters. Thus in this chapter, whether the singular stress field of the bonded pipe shown in Fig. 4.1(a) is governed by (α, β) or not will be investigated.

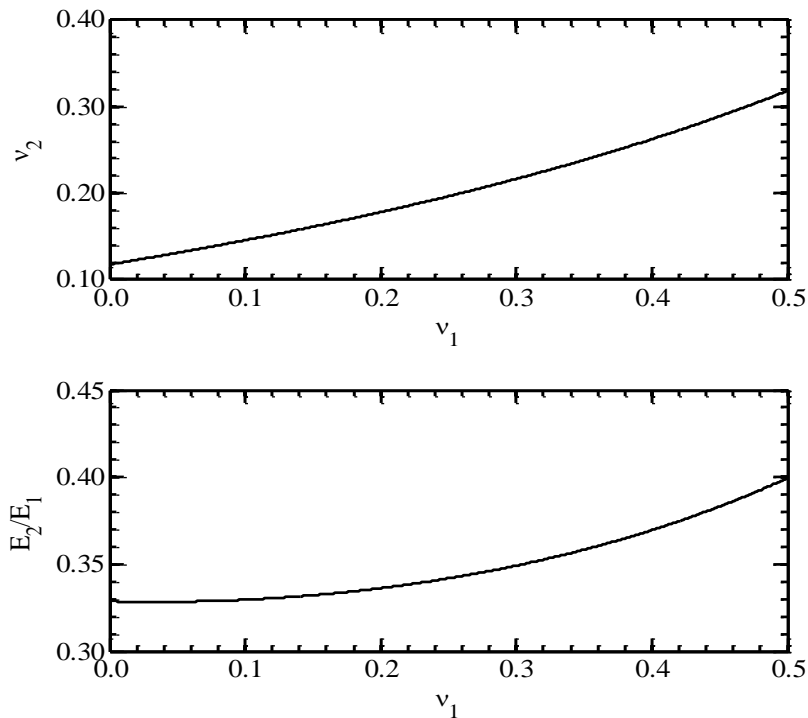


Fig. 4.10 v_2 and E_2/E_1 VS. v_1 under $(\alpha, \beta)=(0.5,0.2)$

Fig. 4.10 show the material combinations under the Dundurs' parameters (α, β)=(0.5,0.2). The properties of two materials are all expressed as the functions of v_1 , which is the Poisson's ratio of material 1. Fig. 4.10 shows that v_2 varies from 0.1177 to 0.3182 while v_1 varies from 0 to 0.5, and E_2/E_1 varies from 0.3284 to 0.3994 while v_1 varies from 0 to 0.5.

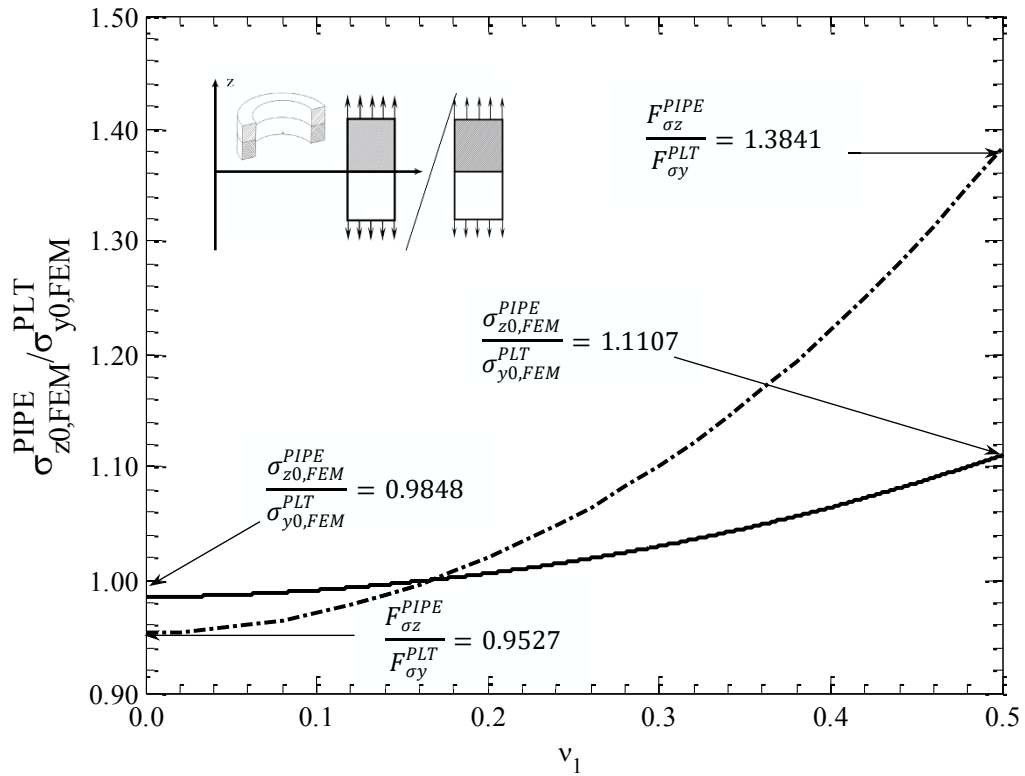


Fig. 4.11 $\sigma_{z0,FEM}^{PIPE} / \sigma_{y0,FEM}^{PLT}$ and $F_{\sigma}^{PIPE} / F_{\sigma}^{PLT}$ VS. ν_1 under $(\alpha, \beta)=(0.5,0.2)$

Fig. 4.11 is the stress ratio for bonded pipe with $R_i/W \rightarrow \infty$ and bonded plate. The ratio for both direct stress and stress intensity factor varies with ν_1 . Very close to the results of bonded cylinder, the value of $\sigma_{z0,FEM}^{PIPE} / \sigma_{y0,FEM}^{PLT}$ varies from 0.9848 to 1.1107 with the variation range of 12.8%, and the value of $F_{\sigma}^{PIPE} / F_{\sigma}^{PLT}$ varies from 0.9527 to 1.3841 with the variation range of 45.0%. This means the Dundurs' parameters (α, β) can not totally control the intensity of singular stress field close to the end of interface for a bonded pipe.

Therefore the maximum and minimum values of $F_{\sigma}^{PIPE} / F_{\sigma}^{PLT}$ should be considered as is discussed in chapter 3.

4.5 Discussion of suitable prediction for debonding strength

Fig. 4.12 shows the value of $F_{\sigma z}^{PIPE} / F_{\sigma y}^{PLT}$ when $\beta=0.2$ is fixed. Both maximum and minimum values are plotted in the figure. As is shown in the figure, the maximum

value of $F_{\sigma_z}^{PIPE}/F_{\sigma_y}^{PLT}$ tends to go infinite when it closes to the equal pair: $\alpha=2\beta$.

Let us check Eqs. (4.1)-(4.4), since the four equations are same as Eqs. (2.22)-(2.24), it can be found that when $\nu_1 = 0.5$, which corresponds to the maximum value of $F_{\sigma_z}^{PIPE}/F_{\sigma_y}^{PLT}$, the denominators of these equations become 0 and therefore the non-singular terms diverge to ∞ under the condition of $\alpha = 2\beta$,

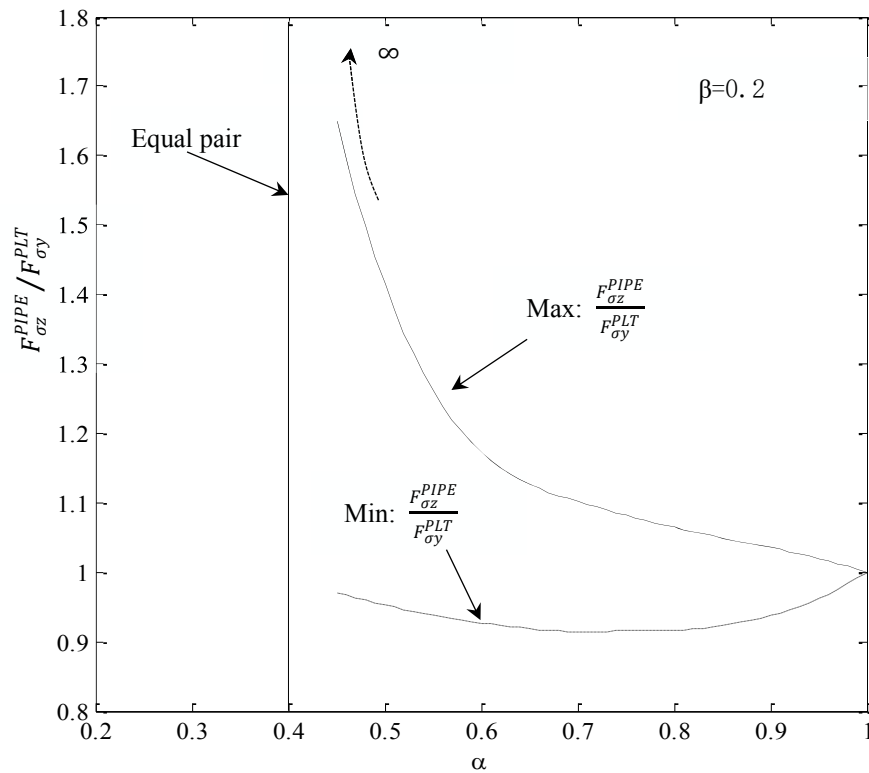


Fig. 4.12 Infinite value of $F_{\sigma_z}^{PIPE}/F_{\sigma_y}^{PLT}$ at equal pair

As discussed in chapter 3, for equal pair and good pair, there is no singularity, therefore, there is no meaning for $F_{\sigma_z}^{PIPE}/F_{\sigma_y}^{PLT}$ under good and equal pair. For the prediction of debonding strength of the bonded structure in good pair and close to equal pair, the direct ratio of stress $\sigma_{z0, FEM}^{PIPE}/\sigma_{y0, FEM}^{PLT}$ is more suitable. Thus for different region we use different value to evaluate the debonding strength of bonded pipe.

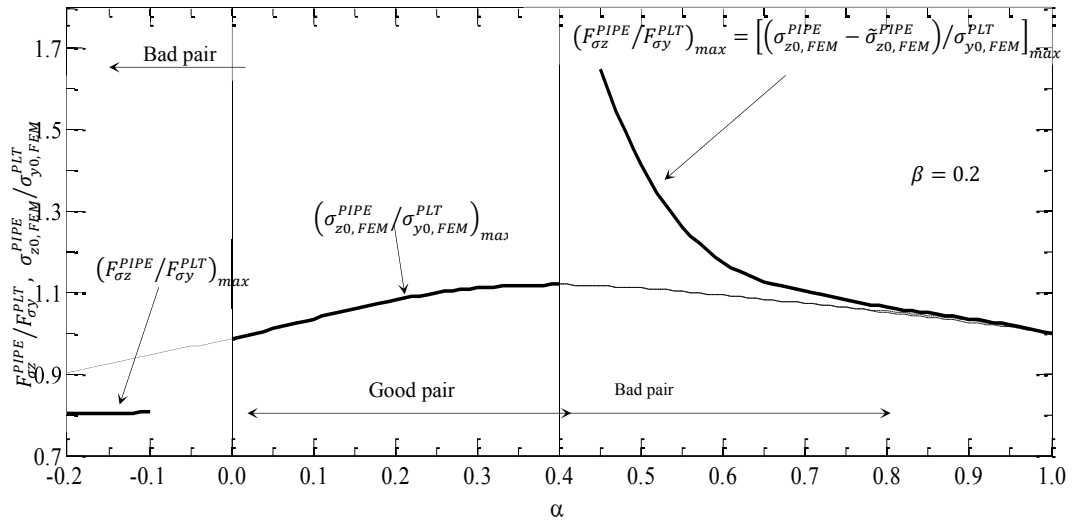


Fig. 4.13 Maximum value of $\sigma_{z0,FEM}^{PIPE}/\sigma_{y0,FEM}^{PLT}$ and $F_{\sigma_z}^{PIPE}/F_{\sigma_y}^{PLT}$ when $\beta=0.2$

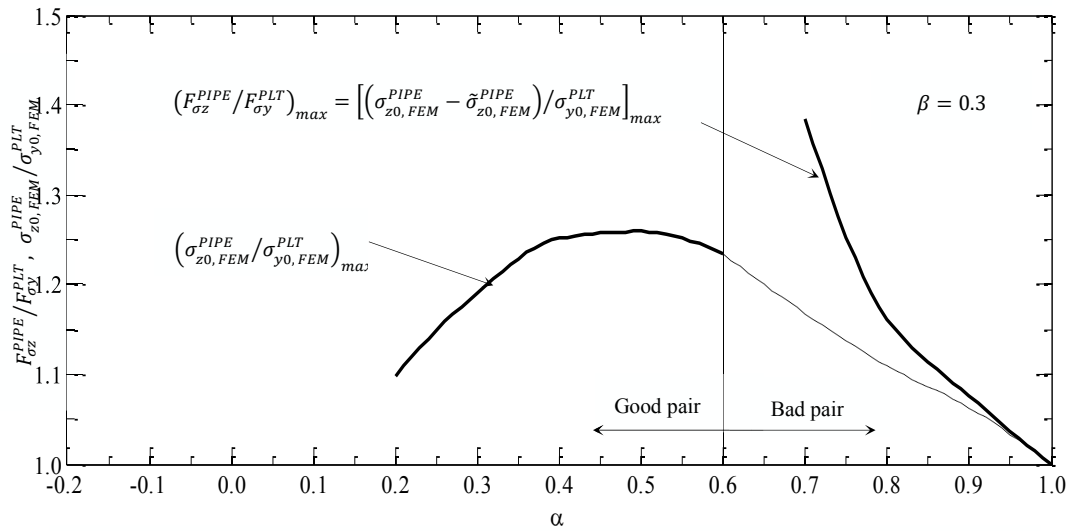


Fig. 4.14 Maximum value of $\sigma_{z0,FEM}^{PIPE}/\sigma_{y0,FEM}^{PLT}$ and $F_{\sigma_z}^{PIPE}/F_{\sigma_y}^{PLT}$ when $\beta=0.3$

The stress singularity occurs at the corner edge point for bad pair; in this case, $F_{\sigma_z}^{PIPE}/F_{\sigma_y}^{PLT}$ is useful for the prediction of the debonding strength. But for equal pair and good pair, there is no singularity, Therefore, the direct ratio of stress $\sigma_{z0,FEM}^{PIPE}/\sigma_{y0,FEM}^{PLT}$ which contains the influence of the non-singular stress is more useful than the $F_{\sigma_z}^{PIPE}/F_{\sigma_y}^{PLT}$ under equal and good pair. Fig. 4.13 shows the maximum value of $F_{\sigma_z}^{PIPE}/F_{\sigma_y}^{PLT}$ and $\sigma_{z0,FEM}^{PIPE}/\sigma_{y0,FEM}^{PLT}$ in α space when $\beta=0.2$ is fixed. In bad pair

region, the $F_{\sigma_z}^{PIPE}/F_{\sigma_y}^{PLT}$ represents the solid line which means the suitable prediction of debonding strength, while in good pair and close to equal pair, $\sigma_{z0,FEM}^{PIPE}/\sigma_{y0,FEM}^{PLT}$ should be used. Fig. 4.14 shows the same situation for the results when $\beta=0.2$.

4.6 Analysis results for bonded pipe under arbitrary material combinations

As is discussed in the previous sector, different regions will use different value to evaluate the debonding strength. In this research, both $F_{\sigma_z}^{PIPE}/F_{\sigma_y}^{PLT}$ and $\sigma_{z0,FEM}^{PIPE}/\sigma_{y0,FEM}^{PLT}$ will be considered, both in maximum and minimum values. Fig. 4.15 and Fig. 4.16 show the maximum and minimum values of $F_{\sigma_z}^{PIPE}/F_{\sigma_y}^{PLT}$ and $\sigma_{z0,FEM}^{PIPE}/\sigma_{y0,FEM}^{PLT}$ by changing the material combinations systematically in (α, β) space.

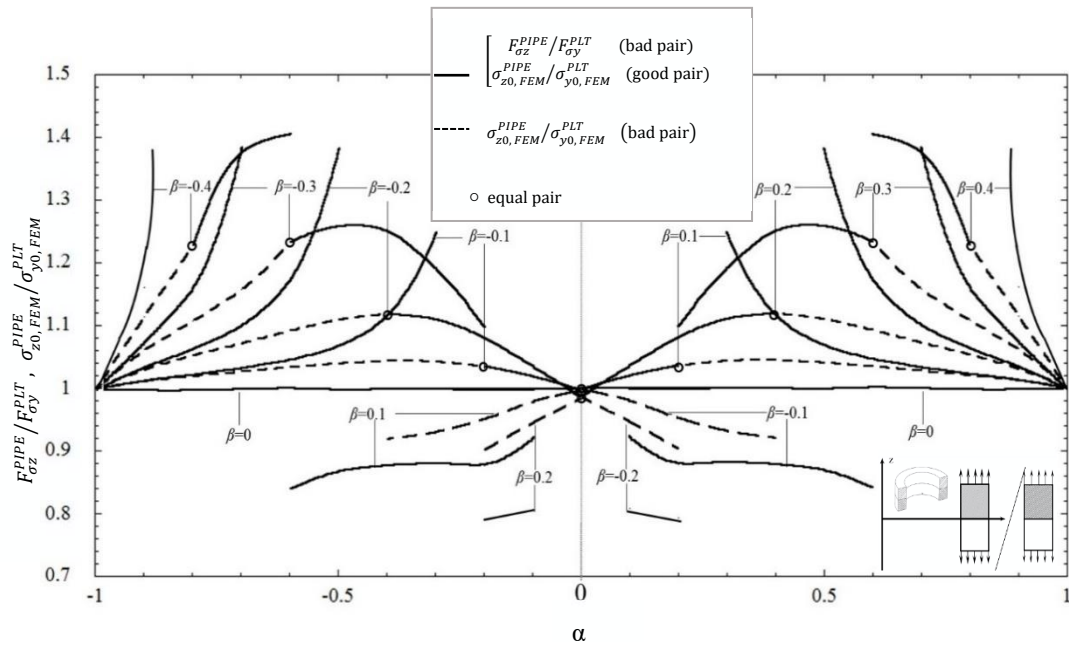


Fig. 4.15 Maximum value of $\sigma_{z0,FEM}^{PIPE}/\sigma_{y0,FEM}^{PLT}$ and $F_{\sigma_z}^{PIPE}/F_{\sigma_y}^{PLT}$ in (α, β) map

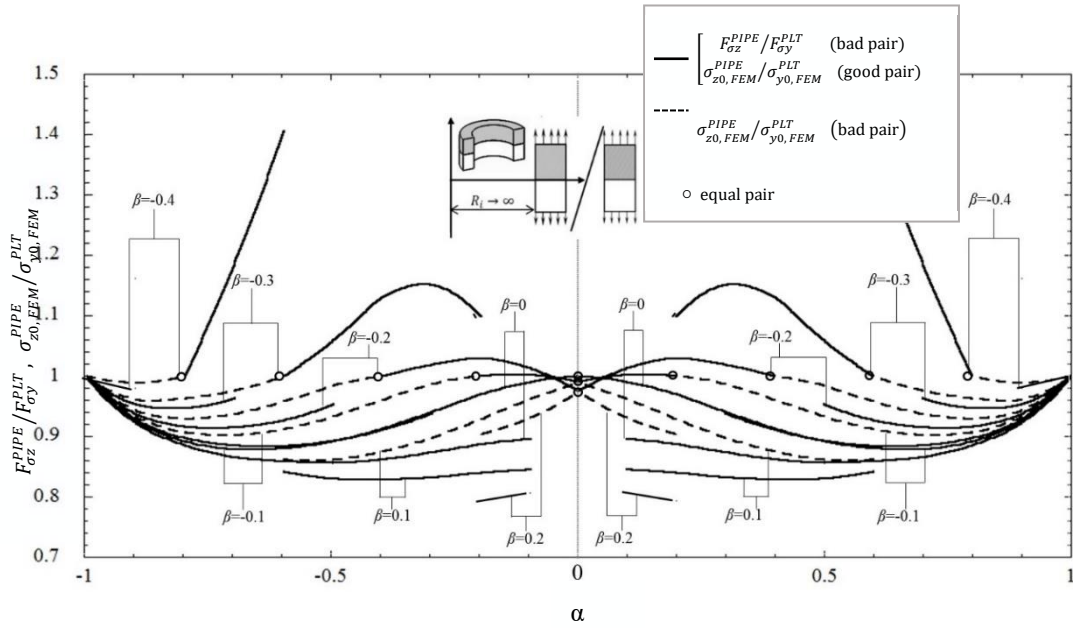


Fig. 4.16 Minimum value of $\sigma_{z0,FEM}^{PIPE}/\sigma_{y0,FEM}^{PLT}$ and $F_{\sigma}^{PIPE}/F_{\sigma}^{PLT}$ in (α, β) map

The results for maximum and minimum value of $F_{\sigma}^{PIPE}/F_{\sigma}^{PLT}$ and $\sigma_{z0,FEM}^{PIPE}/\sigma_{y0,FEM}^{PLT}$ are also shown in Table 4.5-Tabal 4.8.

Table 4.5 Maximum value of $F_{\sigma}^{PIPE}/F_{\sigma}^{PLT}$

$\beta \backslash \alpha$	-0.2	-0.1	0	0.1	0.2	0.3	0.4	0.45
0.1	0.808	0.923	0.999					
0.2	0.794	0.879	0.999					
0.3		0.882	1.000	1.249				
0.4		0.879	1.000	1.114				
0.5		0.870	0.999	1.069	1.382			
0.6		0.842	1.002	1.047	1.172			
0.7			1.000	1.034	1.101	1.383		
0.8			0.998	1.023	1.064	1.160		
0.9			0.998	1.014	1.035	1.075	1.210	
1			1.000	1.000	1.000	1.000	1.000	1.000

Chapter 4

Table 4.6 Minimum value of $F_{\sigma}^{PIPE} / F_{\sigma}^{PLT}$

β α	-0.2	-0.1	0	0.1	0.2	0.3	0.4	0.45
0.1	0.807	0.845	0.896					
0.2	0.794	0.840	0.888					
0.3		0.832	0.874	0.939				
0.4		0.829	0.862	0.911				
0.5		0.830	0.856	0.893	0.953			
0.6		0.842	0.859	0.884	0.927			
0.7			0.865	0.885	0.915	0.963		
0.8			0.885	0.897	0.916	0.947		
0.9			0.920	0.927	0.937	0.953	0.980	
1			1.000	1.000	1.000	1.000	1.000	1.000

Table 4.7 Maximum value of $\sigma_{z=0,FEM}^{PIPE} / \sigma_{y=0,FEM}^{PLT}$

β α	-0.2	-0.1	0	0.1	0.2	0.3	0.4	0.45
0	0.986	0.998	1.000	0.998	0.986			
0.1	0.947	0.981	1.000	1.020	1.036			
0.2	0.904	0.953	1.000	1.036	1.082	1.098		
0.3		0.932	1.000	1.044	1.111	1.191		
0.4		0.921	1.000	1.045	1.119	1.252		
0.5		0.898	1.000	1.041	1.111	1.259		
0.6		0.862	1.001	1.035	1.093	1.234	1.405	
0.7			1.000	1.028	1.073	1.158	1.377	
0.8			1.000	1.021	1.054	1.109	1.228	
0.9			1.000	1.013	1.032	1.063	1.116	1.162
1			1.000	1.000	1.000	1.000	1.000	1.000

Chapter 4

Table 4.8 Minimum value of $\sigma_{z0,FEM}^{PIPE}/\sigma_{y0,FEM}^{PLT}$

$\alpha \backslash \beta$	-0.2	-0.1	0	0.1	0.2	0.3	0.4	0.45
0	0.975	0.990	1.000	0.990	0.975			
0.1	0.931	0.963	0.992	1.002	1.013			
0.2	0.904	0.929	0.971	1.000	1.030	1.098		
0.3		0.898	0.941	0.988	1.019	1.152		
0.4		0.875	0.913	0.961	1.000	1.132		
0.5		0.861	0.892	0.933	0.985	1.059		
0.6		0.862	0.880	0.912	0.958	1.000	1.405	
0.7			0.878	0.902	0.937	0.976	1.186	
0.8			0.891	0.906	0.929	0.963	1.000	
0.9			0.924	0.931	0.942	0.960	0.989	1.000
1			1.000	1.000	1.000	1.000	1.000	1.000

For most of the material combinations distributed in $0 < \beta < 0.3$ [7], the value of

$\left(\sigma_{z0,FEM}^{PIPE}/\sigma_{y0,FEM}^{PLT}\right)_{max}$ is approximately located as the following range

$$1.0 \leq \frac{\sigma_{z0,FEM}^{PIPE}}{\sigma_{y0,FEM}^{PLT}} \leq 1.3 \quad (4.5)$$

Comparing the data in Table 4.15 with Table 4.16, it is found that the range of $\sigma_{z0,FEM}^{PIPE}/\sigma_{y0,FEM}^{PLT}$ is quite different for different (α, β) . The differences between

$\left(\sigma_{z0,FEM}^{PIPE}/\sigma_{y0,FEM}^{PLT}\right)_{max}$ and $\left(\sigma_{z0,FEM}^{PIPE}/\sigma_{y0,FEM}^{PLT}\right)_{min}$ is approximately obtained as follows.

$$\frac{\left(\sigma_{z0,FEM}^{PIPE}/\sigma_{y0,FEM}^{PLT}\right)_{max} - \left(\sigma_{z0,FEM}^{PIPE}/\sigma_{y0,FEM}^{PLT}\right)_{min}}{\left(\sigma_{z0,FEM}^{PIPE}/\sigma_{y0,FEM}^{PLT}\right)_{max} + \left(\sigma_{z0,FEM}^{PIPE}/\sigma_{y0,FEM}^{PLT}\right)_{min}} \leq 0.105 \quad (4.6)$$

Since the differences between $\left(\sigma_{z0,FEM}^{PIPE}/\sigma_{y0,FEM}^{PLT}\right)_{max}$ and $\left(\sigma_{z0,FEM}^{PIPE}/\sigma_{y0,FEM}^{PLT}\right)_{min}$ are less than about 10.5% as shown in Eq. (4.6), it can be

verified that the effect of the material combination can be put in order by Dundurs'

parameters (α, β).

4.7 Conclusion and discussion

In this chapter, the bonded pipe with different R_i/W were investigated and the effect of R_i/W on singular stress field has also been studied. After the verification of analysis method in bonded pipe, the intensities of the singular stress field for the bonded pipe was analyzed by applying the proportional method proposed in chapter 2. The results were calculated by changing the material combination systematically under (α, β) space. The results of bonded pipe has been compared with that of plane strain problem and the difference was elaborated. The difference between bonded pipe and bonded cylinder were also discussed. After that, the maximum and minimum values of $F_{\sigma z}^{PIPE}/F_{\sigma y}^{PLT}$ and $\sigma_{z0, FEM}^{PIPE}/\sigma_{y0, FEM}^{PLT}$ are shown in tables and figures in the space of Dundurs' parameters.

The achievements of this chapter have been conclude as follows:

1. The stress components for bonded pipe converged when $R_i/W \geq 0.001 \times 2^{16}(65.536)$, and also same stress component at inner point and outer point coincide each other when $R_i/W \geq 0.001 \times 2^{16}(65.536)$, which means the change of inner radius or R_i/W has no effect on the stress components if it's large enough. Therefore in this research, it is assumed that $R_i/W \geq 10^5$.

2. Although the change of inner radius or R_i/W has no effect on the stress components when it's large enough, there are still differences between the bonded pipe and bonded plane strain problem since the existence of non-singular circumference strain ε_{θ} in bonded axi-symmetric problems.

3. The analysis method used in bonded cylinder is suitable for bonded pipe if accurate radial displacement at the end of interface can be obtained.

4. The bonded pipe is different from plane strain problems. The singular stress field near the end of interface of two dimensional problems as shown in Figs. 4.1(b) is governed by Dundurs' parameters (α, β) uniquely regardless of the plane stress condition or the plane strain condition. However, the singular stress field of bonded

pipe in Fig. 4.1(a) is not governed by (α, β) , as same as the situation in bonded cylinder. Therefore the maximum and minimum value of $F_{\sigma_z}^{PIPE}/F_{\sigma_y}^{PLT}$ should be considered.

5. Similar as bonded cylinder, it's suitable to use $F_{\sigma_z}^{PIPE}/F_{\sigma_y}^{PLT}$ for the prediction of debonding strength of the bonded pipe in bad pair, as for good pair and close to equal pair, the direct ratio of stress $\sigma_{z0, FEM}^{PIPE}/\sigma_{y0, FEM}^{PLT}$ is more suitable since it contains the influence of the non-singular stress. Thus for different region we use different value to evaluate the debonding strength.

6. For most material combinations which are distributed in $0 < \beta < 0.3$ under the (α, β) space, the value of $\left(\sigma_{z0, FEM}^{PIPE}/\sigma_{y0, FEM}^{PLT}\right)_{max}$ is approximately located as the following range

$$1.0 \leq \frac{\sigma_{z0, FEM}^{PIPE}}{\sigma_{y0, FEM}^{PLT}} \leq 1.3$$

And since the differences between $\left(\sigma_{z0, FEM}^{PIPE}/\sigma_{y0, FEM}^{PLT}\right)_{max}$ and $\left(\sigma_{z0, FEM}^{PIPE}/\sigma_{y0, FEM}^{PLT}\right)_{min}$ is less than about 10.5%, the effect of the material combination can be put in order by Dundurs' parameters (α, β) .

4.8 Reference of Chapter 4

- [1] J. Arenas, J.J. Narbon, C. Alia. Optimum adhesive thickness in structural adhesives joints using statistical techniques based on Weibull distribution. *International Journal of Adhesion&Adhesives*, 30, 160-165 (2010).
- [2] M. Afendi, T. Teramoto, H. B. Bakri. Strength prediction of epoxy adhesively bonded scarf joints of dissimilar adherends. *International Journal of Adhesion&Adhesives*, 31, 402-411(2011).
- [4] D. Hunston, Z. Miyagi, C. Schultheisz, S. Zaghi. *Mechanics of Time-Dependent Materials*, 7, 71-88 (2003).

Chapter 4

[5] Y. Suzuki. Transactions of the Japan Society of Mechanical Engineers, A-53, 514-522(1987).

[6] A.A. Neves, E. Courinho, A.Poitevin. Influence of joint component mechanical properties and adhesive layer thickness on stress distribution in micro-tensile bond strength specimens. Dental Materials, 25, 4-12 (2009).

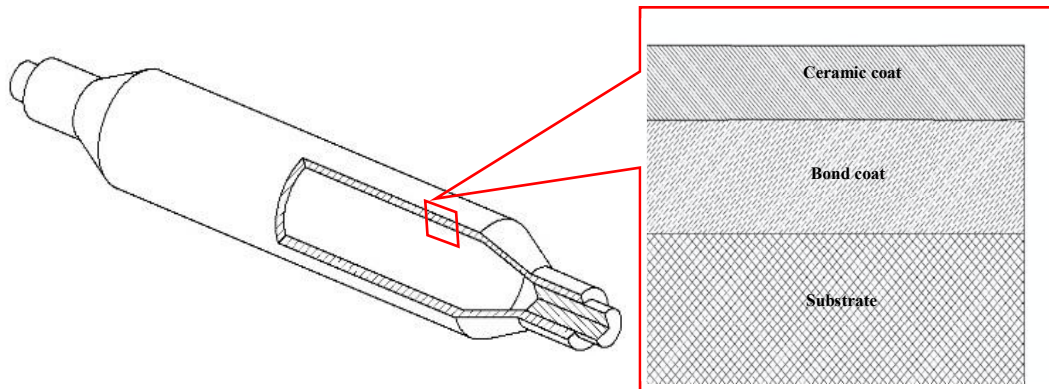
[7] Yuuki, R., Xu, J. -Q, Liu, J. -Q., Analysis of Stress Singularity at Interface Edge in Dissimilar Materials, Seisan Kenkyu, Vol. 44, No. 4 (1992), pp. 206 - 210

Chapter 5 Analysis on singular stress intensity of ceramic spray coating on hearth roll

5.1 Introduction



(a) Hearth roll used in CAL



(b) Structure of hearth roll with spray coating

Fig. 5.1 Hearth roll used in CAL

The properties of ceramic and metal have mutual compensation relationship. Their application can be more extensive by bonding them together. Therefore, Ceramic to

metal bonding is seeing increased application for use in sensors, electronic packaging and in steel industry. Hearth rolls (Fig. 5.1) are the most important part in continuous annealing line which is used to produce thin steel sheet. Usually the roll surface is coated by ceramic spray coating.

There are various methods for the bonding of metal and ceramics, such as brazing, solid phase diffusion bonding, partial transient liquid phase bonding and self-propagating high-temperature synthesis, which are described as follows:

1. Adhesive joints: ceramic and metal are bonded by adhesion. This kind of joints are usually used in the manufacturing and maintenance of aero-engine. The adhesive joints can be only use as the disposable parts which can only sustain static load, although it has many advantages such as low costs and easy to process.

2. Fusion welding: Including electron beam machining (EBM) and laser beam welding(LBW). As laser and electron beam can create high temperature to melt the metal and ceramic, the two materials can be bonded very well and can resist high temperature[1,2]. However this kind joints need complex process such as preheat and slow cooling and hence is expensive.

3. Brazing: Brazing offers high joint strength (close or equal to that of the ceramic), high in service temperature (about 0.6 the absolute melting temperature of the braze), excellent thermal and electrical conductivity, excellent tightness and moderate costs[3,4].

4. Solid phase diffusion bonding: the jointing is achieved by tight contact of metal and ceramics under certain pressure and temperature (with contacting distance of 10^{-10} m). By recrystallization and the change of grain boundary, new metal bond or chemical bond were formed at the interface, thereby forming a solid combination of joint[5]. However this method usually needs an intermediate layer which can reduce the residual stress caused by the mismatch properties of metal and ceramic.

5. Self-propagating high-temperature synthesis(SHS): This method uses the reaction that generates high temperatures between metal and ceramic which can melts the two materials at the interface and finally bonded them together. Since there is

mismatch of metal and ceramic, functionally gradient solders are usually use to reduce the residual stress[6,7]. And notably, the reaction is too quick and is very hard to control, quality control is poor.

Among these methods, the reactive brazing and solid phase diffusion bonding method are more mature, with high strength and good repetition joint, and widely used to bond ceramic/metal compound structure for middle and low temperature application. The partial transient liquid phase bonding is the most promising method.

Table 5.1 Material properties of several typical metals and ceramics

Material		E (GPa)	ν	Remark
Metal	Al	70	0.34	
	Cu	108	0.32	
	TC4*	110	0.34	Cr5 or BT6
	SUS	195	0.27	SUS304
Ceramic	ZrO ₂	210	0.25	
	Si ₃ N ₄	310	0.25	
	Al ₂ O ₃	360	0.22	
	SiC	475	0.142	

Common ceramic to metal joints are Al₂O₃ to metal, ZrO₂ to metal, SiC to metal, Si₃N₄ to metal, the metal includes but is not limited to the following: SUS, Ti, Cu, Ni, Al. Table. 5.1 shows the properties of several typical metals and ceramics.

Usually the strength of the bonding is evaluated by the intensity of singular stress at the end of interface. Therefore the Dundurs' parameters α , β and singular index λ is important in the prediction of debonding strength[8-11]. Table 5.2 and 5.3 show the Dundurs' parameters α , β and singular index λ for each combinations between several typical metals and ceramics.

Chapter 5

Table 5.2 Dundurs' parameters (α , β) for different combinations of metals and ceramics

Ceramics Metal	ZrO ₂	Si ₃ N ₄	Al ₂ O ₃	SiC
Al	(0.4778, 0.0921)	(0.6137, 0.1312)	(0.6540, 0.1384)	(0.7193, 0.1498)
Cu	(0.3011, 0.0557)	(0.4664, 0.1052)	(0.5174, 0.1142)	(0.6023, 0.1291)
TC4	(0.2860, 0.0369)	(0.4533, 0.0851)	(0.5051, 0.0936)	(0.5916, 0.1077)
SUS	(0.0315, 0.0011)	(0.2224, 0.0630)	(0.2854, 0.0742)	(0.3948, 0.0935)

Table 5.3 Singular index λ for different combinations between metals and ceramics

Ceramics Metals	ZrO ₂	Si ₃ N ₄	Al ₂ O ₃	SiC
Al	0.9028	0.8571	0.8398	0.8103
Cu	0.9571	0.9146	0.8958	0.8618
TC4	0.9551	0.9103	0.8910	0.8561
SUS	0.9982	0.9829	0.9696	0.9391

* Blue color means low singularity, red color means strong singularity.

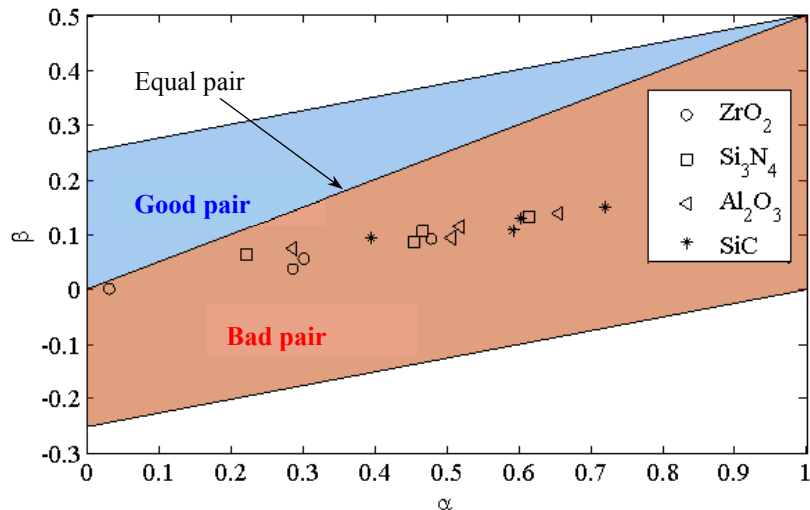
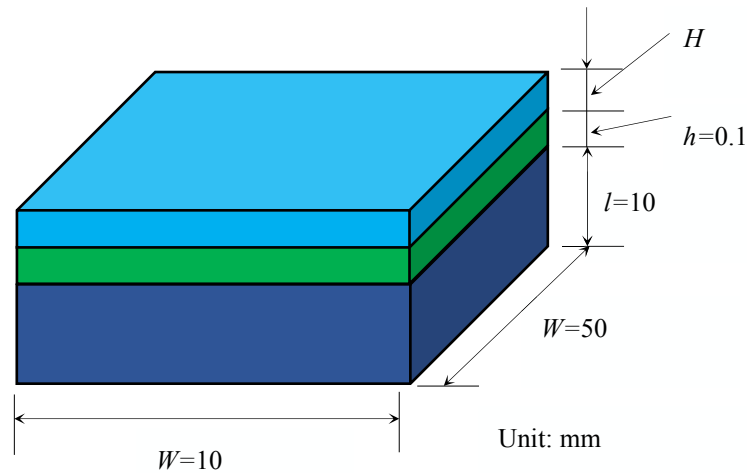


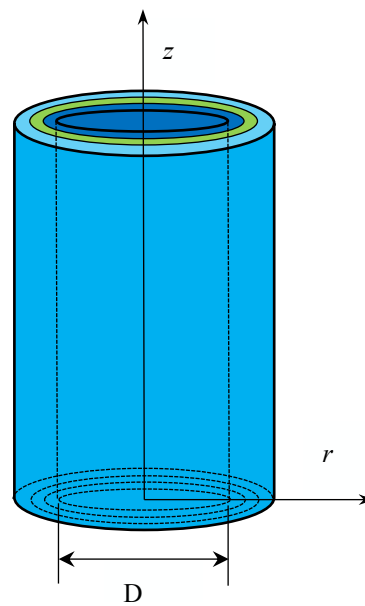
Fig. 5.2 Material combinations of metal and ceramics in (α , β) space

As shown in Table 5.3, the combinations contains ZrO₂ or SUS are better than that with SiC and Al. All combinations are plotted in Fig. 5.2, in which the points close to equal pair are better than the points away from the equal pair. It can explain why most

ceramics spray coating, hearth rolls for example, are used between ZrO_2 and steel. And this chapter will mainly focus on the strength evaluation of ceramic spray coating on the surface of hearth rolls.



(a) JIS 8304 specimen for thermal shock test



(b) Cylindrical structure of hearth roll

Fig. 5.3 Specimen for thermal shock test and the test conditions

Hearth rolls (Fig. 5.2) are the most important part in continuous annealing line which is used to produce thin steel sheet. Usually the roll surface is coated by ceramics using thermal spraying. However, mismatch of materials and temperature change may

cause thermal stress which will lead to the failure of the coating, although it has high adhesive strength and wears resistance. Therefore, to optimize the design of spray coating and improve the debonding strength of it is very important. The traditional method of evaluating the debonding strength of spray coating is to carry out the thermal test specified by JIS H8304[12]. While this research will focus on the intensity of singular stress at the end of interface, as few research is available in terms of singular stress. Previous researches are based on the JIS specimen which is a plane strain problem, however the hearth roll, which should be an axi-symmetric problem in practical engineering, is cylindrical. As discussed in chapter 4, the difference between these two models can't be ignored, thus in this chapter the 2-D axi-symmetric model will be considered and the optimum design will be discussed by varying the coating material and the coating thickness. Also the new results will be compared with the previous research based on the JIS specimen so that the difference between actual model and JIS specimen can be obtained, which may make a contribution to the design and evaluation of the rolls, and also make the achievement of chapter 4 useful in the application of engineering.

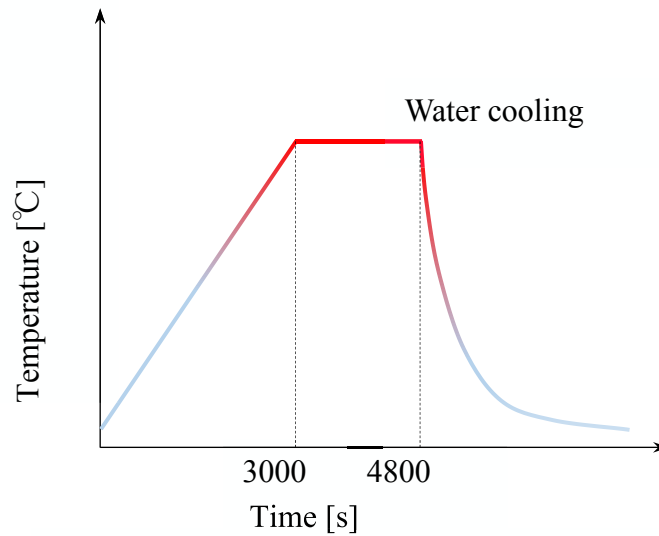
Continuous annealing furnace is the common production line for producing steel sheet used in automobile industry. As is known to all, the rolls work in a harsh environment since the temperature is usually between 700°C and 800°C and some specialist grades require treatment at temperatures up to 1200 °C [13]. Therefore, excellent performance of material and structure of rollers is demanded. First, the surface of the roller should be able to do against corrosion and oxidation at high temperatures. Secondly, it must be wear-resistant and has a longer service life[14]. For this demand, the ceramic spaying coating rollers came into being(Fig. 1(a)), and has been widely used in recent decades[15,16]. However, failure of the ceramic coating layer due to mismatch of materials and cyclic thermal shock in the furnace should be considered. Thus, the ceramic coating is not usually sprayed alone, while multi-layer coating with adhesive layer is usually employed(Fig. 5.2(b)).

In order to improve the coating strength and service life, many different processes

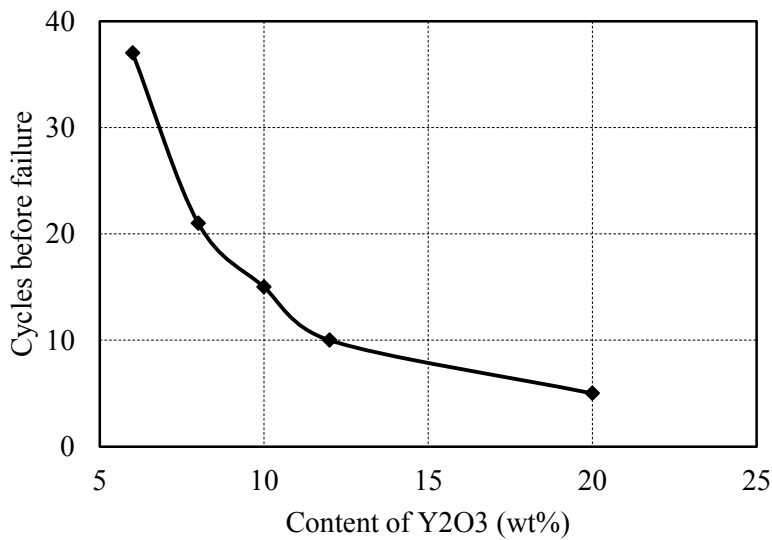
and materials have been proposed. Meanwhile, the evaluation of debonding strength has been studied by many researcher. In Japan, the thermal shock resistance of the spaying coating structure is accessed by experiments specified by JIS8304(2007)Fig. 5.3(a)[12]. Mutoh et al have reported the thermal shock damage characteristics based on experimental results and finite element analysis [17]. However in order to more accurately assess the interfacial strength of dissimilar materials adhesive structures, it is necessary to consider the singularity of thermal stress near the corner of the interface. So far, few studies have been conducted to the research of intensity of singular stress on this multi-layer structure under thermal shock. Noda et al proposed a convenience evaluation method for spray coating based on intensity of singular stress near the end of interface[18]. However the previous research is based on the JIS specimen which is a plane strain problem, while the hearth roll is cylindrical which should be an axi-symmetric problem in practical engineering(Fig. 5.3(b)). The difference between these two models can not be ignored especially for the roller with a small diameter, thus in this paper the 2-D axi-symmetric model will be considered and the optimum design will be discussed by varying the coating material and the coating thickness. Also the new results will be compared with the previous research based on the JIS specimen so that the difference between actual model and JIS specimen can be obtained.

5.2 Key parameters for analysis

The process of thermal shock test specified by JIS8304(2007) is shown by Fig. 5.4 (a). First the specimen is heat up to 1000°C and keep the temperature for a 1800s to ensures an even heat of the specimen, then the specimen is merged into water of 20°C to simulate the rapidly cooling. This cycle repeats again and again until the failure of coating occurs.



(a) Temperature history of thermal shock test



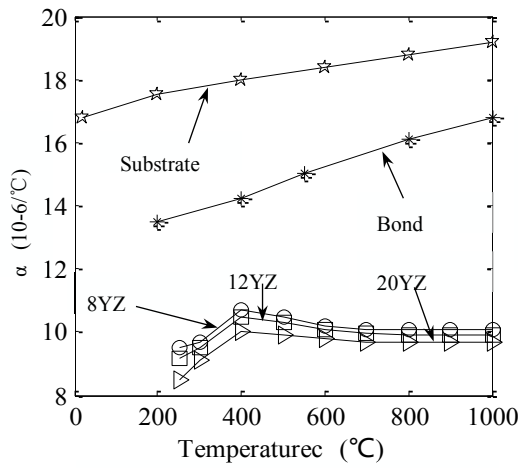
(b) Results of thermal shock test

Fig. 5.4 Thermal shock test specified by JIS8304(2007)

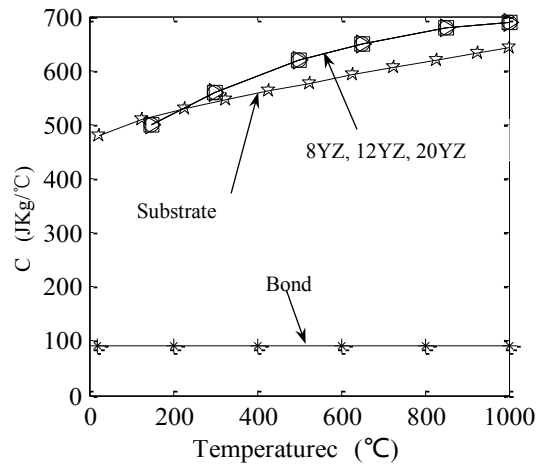
The JIS specimen is a cubic SUS304 steel coated with yttrium (Y₂O₃) stabilized zirconia (ZrO₂). The top coating ZrO₂ with 8wt% ~ 20wt% of Y₂O₃ (The following % will be omitted) and the substrate are bonded with CoNiCrAlY. The material properties are shown in Table 1. Figure 4 shows the material properties of three layers: coefficient of expansion α_e , specific heat C, young's modulus E and thermal conductivity K.

Table 5.4. Material Properties depending on temperature

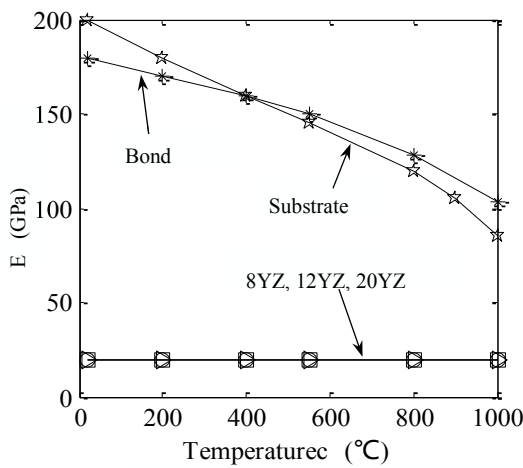
Material		Young's modulus E [GPa]	Poisson's ratio ν	Thermal expansion α_e [$10^{-6}/K$]
Top Coating	20YZ (ZrO_2 -20wt% Y_2O_3)	20	0.25	7.5-9.7
	12YZ (ZrO_2 -12wt% Y_2O_3)			8.3-9.93
	8YZ (ZrO_2 -8wt% Y_2O_3)			8.7-10.05
Bonded Coating(CoNiCrAlY)		103-180	0.33	2.8-16.8
Substrate(SUS304)		85-200	0.3	16.8-19.2



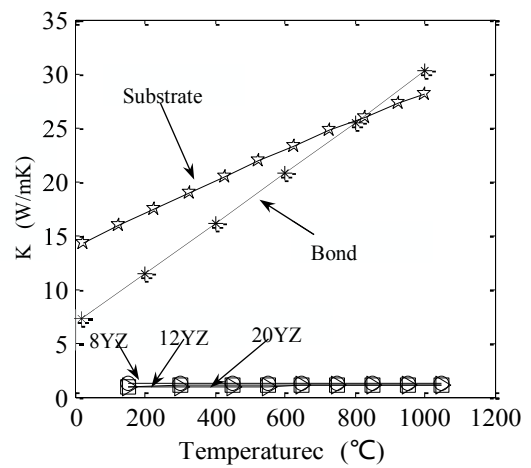
(a) Coefficient of expansion



(b) Specific heat



(a) Young's modulus



(a) Thermal conductivity

Fig. 5.5 Relationship between material properties and temperature

5.3 Analysis method for the singularity of thermal stress

In this study, we mainly focus on the intensity of singular stress near the end of interface between coating layer during the thermal shock test. The optimization will be based on the analysis of intensity of singular stress, in which the effect of the coating thickness will be investigated. In previous study, a convenient method for the solution of ISSF in an adhesive bonding plate under bending and tension has been proposed [19, 20]. Thus in this paper, this method is applied to analysis the coating problem under thermal shock.

In this method, FEM is use to get the value of stress at the end of interface when simulating the thermal shock. The JIS specimen is a plane strain problem, while in this paper, the 2-D axi-symmetric model shown in Figure 5.6 is use as the analysis model so that the results of actual structure and experimental specimen can be compared. Here the subscript 1, 2 and 3 represent the top coating, bond coating and substrate respectively, with the corresponding material properties shown in Table 5.4. The ANSYS 16.2 is used in this research and the 4 nodes quad element was employed. The analysis type is thermal-structural, and all materials are considered as elastic.

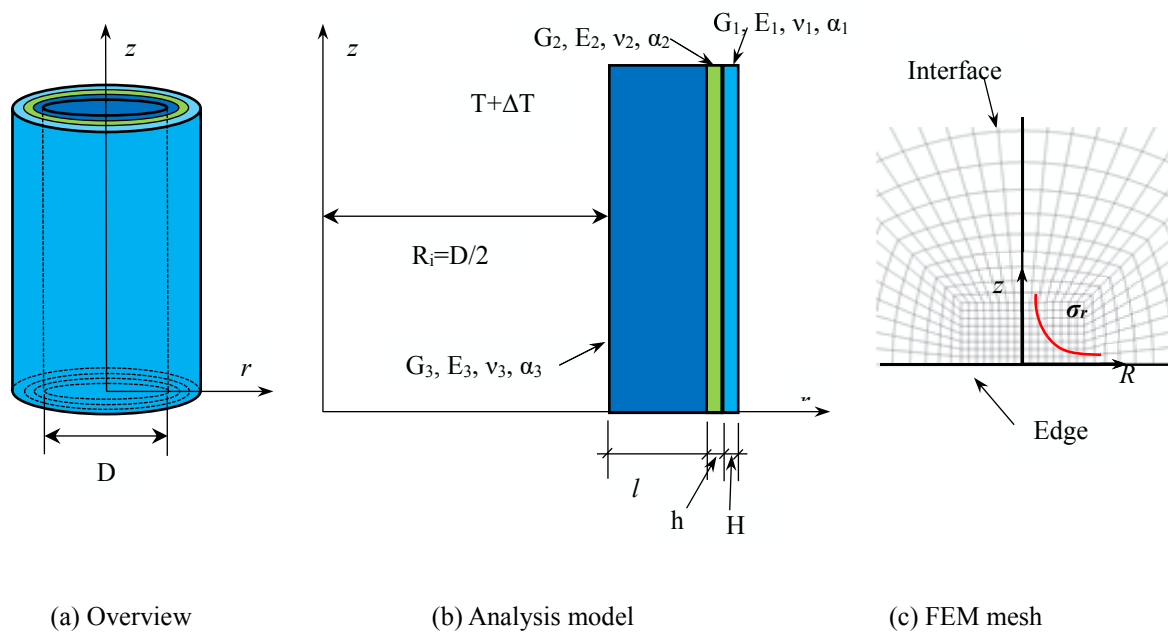


Fig. 5.6 Analytical model and FEM mesh

For bonded structure shown in Fig. 5.6, it is known that the stress at the end of

interface goes infinity with its singularity of $\sigma_{ij} \propto 1/R^\lambda$, in which R is the distance from the end of interface in a dissimilar materials bonded structure. Here λ is singular index, which is the root of Eq. (5.1). As for α and β in Eq. (5.1) are known as Dundurs' parameters which are expressed by the following Eq. (5.2)[10,11], here ν is Possion's ratio and $G = E/2(1+\nu)$ is shear modulus.

$$\left[\sin^2\left(\frac{\pi}{2}\lambda\right) - \lambda^2 \right] \beta^2 + 2\lambda^2 \left[\sin^2\left(\frac{\pi}{2}\lambda\right) - \lambda^2 \right] \alpha\beta + \lambda^2 (\lambda^2 - 1) \alpha^2 + \frac{\sin^2(\pi\lambda)}{4} = 0 \quad (5.1)$$

$$\alpha = \frac{G_1(\kappa_2 + 1) - G_2(\kappa_1 + 1)}{G_1(\kappa_2 + 1) + G_2(\kappa_1 + 1)},$$

$$\beta = \frac{G_1(\kappa_2 - 1) - G_2(\kappa_1 - 1)}{G_1(\kappa_2 + 1) + G_2(\kappa_1 + 1)}, \quad (5.2)$$

$$\kappa_j = \begin{cases} \frac{3-\nu_j}{1+\nu_j} (\text{plane stress}) \\ 3-4\nu_j (\text{plane strain}) \end{cases} \quad (j=1,2)$$

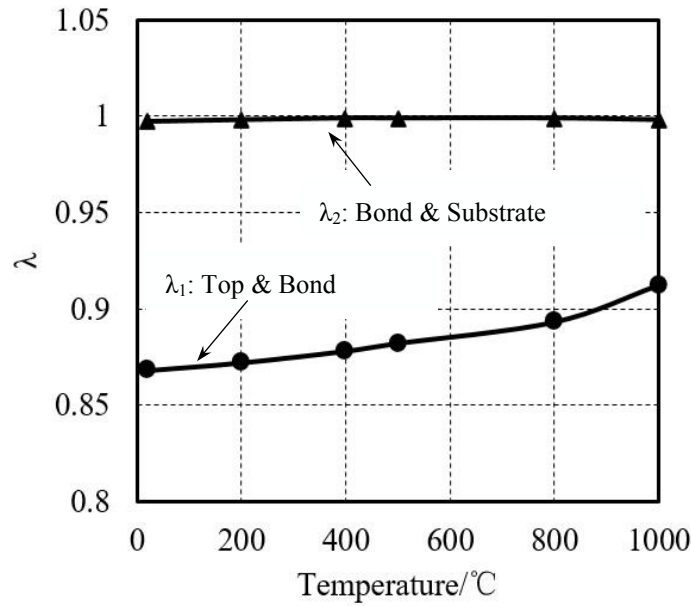


Fig. 5.7 Relationship between temperature and singular index λ

Since all properties of the three materials vary with temperature, the singular stress field is therefore changed by the variety of material properties. The relationship of singular index λ and temperature is plotted in Fig. 5.7. Singular index λ_2 of the interface

between the bond coating and substrate is close to 1, which means less singularity. Therefore, this study will mainly focus on the singularity between top coating and bond coating as shown in Fig.5.6. During the thermal shock test process as shown in Fig. 5.4(b), water-cooled condition is simulated by given temperature 20 °C to the entire surface of specimen at t = 4800s, then the temperature distribution and thermal stress was determined by thermal and elastic analysis.

Thermal stress σ_r is caused by entire body temperature difference $T + \Delta T$ in the bonded structure shown in Fig. 5.8(a). In our previous research[21], it is found that there is non-singular terms $\tilde{\sigma}_r$ in the stress component as shown in Eq. (5.3), thus it is necessary to eliminate the non-singular term. There is also another non-singular term σ_0 caused by thermal stress [22]. By eliminating the non-singular terms σ_0 , and $\tilde{\sigma}_r$ the remaining singular term $(\sigma_y - \sigma_0 - \tilde{\sigma}_r)$ has a singularity of $r^{1-\lambda}$ expressed as Eq. (5.4).

$$\sigma_r^{Axial} - \sigma_0 = \lim_{r \rightarrow 0} \frac{K_{\sigma}^{Axial}}{r^{1-\lambda}} + \tilde{\sigma}_r = \lim_{r \rightarrow 0} \frac{K_{\sigma}^{Axial}}{r^{1-\lambda}} + \frac{(\nu_1 - \nu_2)E_1E_2}{(1 + \nu_1)\nu_1E_2 - (1 + \nu_2)\nu_2E_1} \frac{u_{r0}^{AXIAL}}{(W + R_{inf})} \quad (5.3)$$

$$\sigma_r^{Axial} - \sigma_0 - \tilde{\sigma}_r = \lim_{R \rightarrow 0} \frac{K_{\sigma}^{Axial}}{R^{1-\lambda}} \quad (5.4)$$

This intensity of singular stress field caused by thermal stress is equivalent to the one that subjected to the tension of σ_0 determined by Eq. (5.5)[19].

$$\sigma_0 = -\Delta\alpha\Delta E\Delta T, \quad (5.5)$$

where,

$$\Delta\alpha = \begin{cases} \alpha_1 - \alpha_2 & (\text{plane stress}) \\ (1 + \nu_1)\alpha_1 - (1 + \nu_2)\alpha_2 & (\text{plane strain}) \end{cases} \Delta E = \frac{8}{\left\{ \frac{(\kappa_1 - 3)}{G_1} - \frac{(\kappa_2 - 3)}{G_2} \right\}}$$

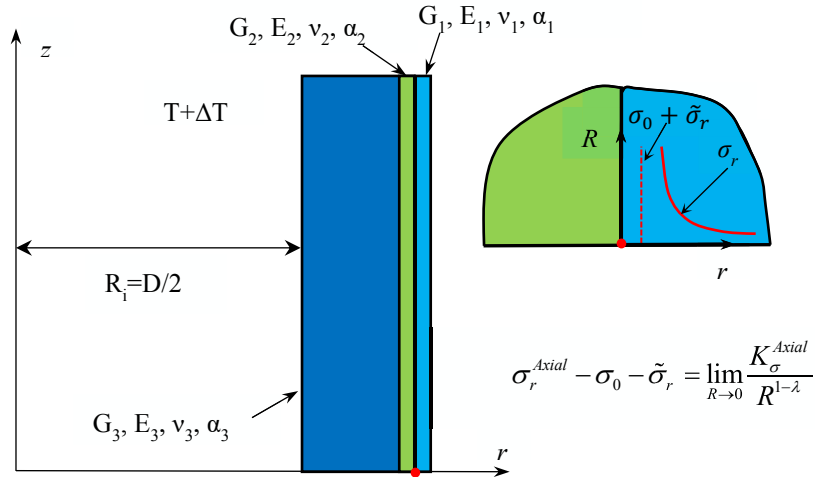
$$\kappa_j = \begin{cases} \frac{3 - \nu_j}{1 + \nu_j} & (\text{plane stress}) \\ 3 - 4\nu_j & (\text{plane strain}) \end{cases}, \quad G_j = \frac{E_j}{2(1 + \nu_j)} \begin{cases} j = 1 : \text{Top coat,} \\ j = 2 : \text{Middle coat} \end{cases}$$

The problem of finite bonded plate subjected to tension shown in Fig. 5.8(b) has been accurately calculated by using body force method [23, 24]. Since the singular stress fields are similar if the material angles of two bonded structures are same, then the stress intensity of unknown problem shown in Fig. 5.8(a) can be determined by

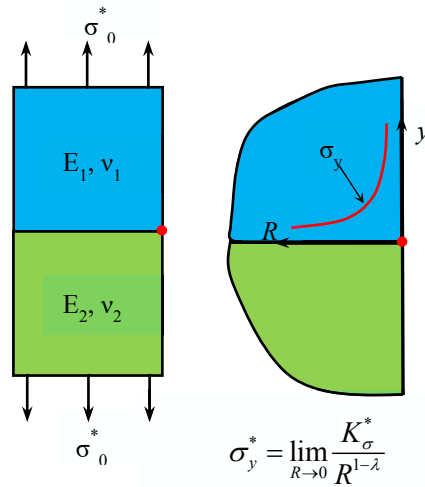
apply this known solution (Fig.5.8(b)) to Eq. (5.6)[19,20, 25].

$$\frac{K_{\sigma}}{K_{\sigma}^*} = \frac{F_{\sigma} \sigma_0 W^{1-\lambda}}{F_{\sigma} \sigma_0^* W^{1-\lambda}} = \frac{\sigma_{r,FEM} - \sigma_0 - \tilde{\sigma}_r}{\sigma_y^{FEM^*}} \quad (5.6)$$

Here the superscript * means known reference problem.



(a) Thermal singular stress field for ceramic coating as unknown problem



(a) The bonded strip model as the known reference problem

Fig. 5.8 Comparing known problem and unknown problem

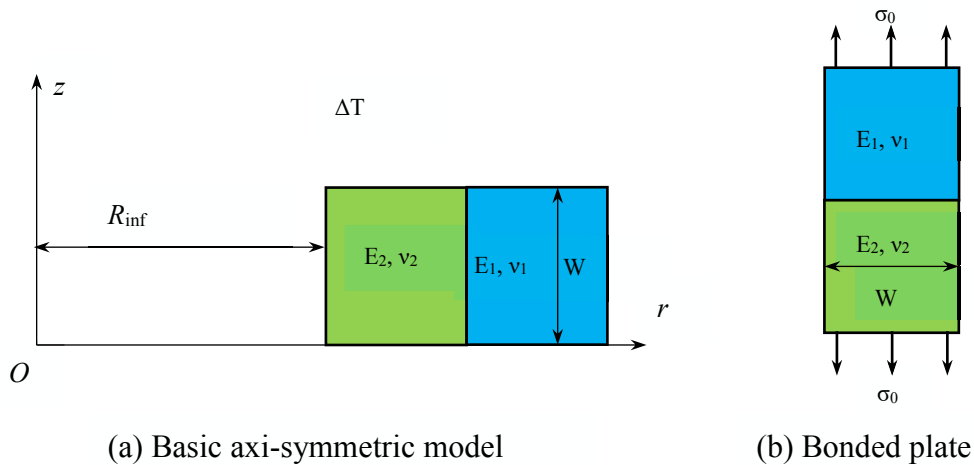
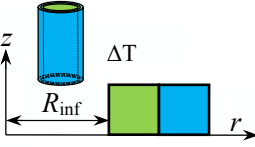

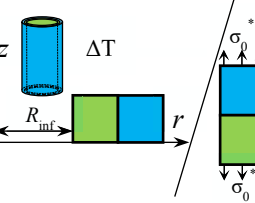


Fig. 5.9 Basic axi-symmetric problem and bonded plate

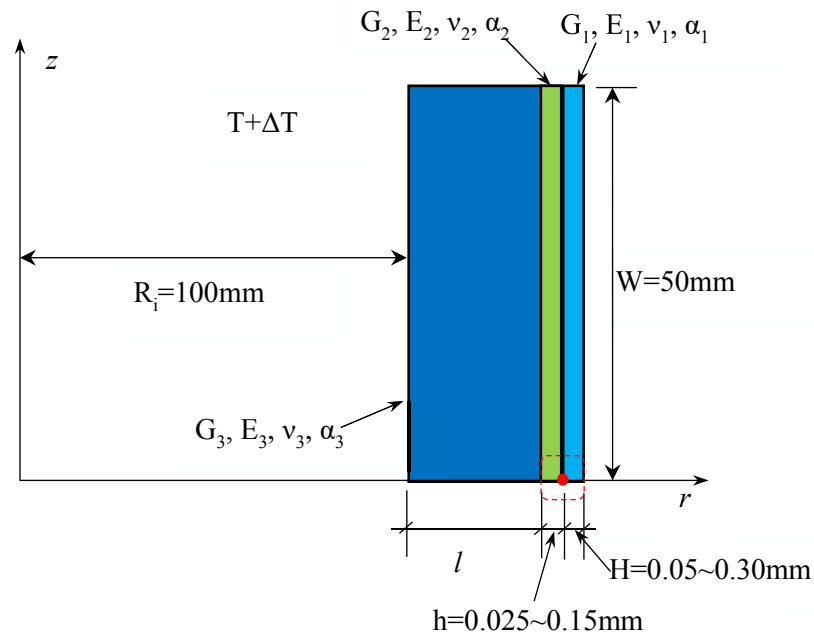
A basic bonded axi-symmetric problem under thermal load is investigated to verify application of proportional method expressed as Eq. (5.5). Considering the thickness of coating is usually small enough compared to the inner radius of the roll, the inner radius of the basic model is assumed as infinite (Fig. 5.9(a)). Here we use $W/R_{inf}=10^{-5}$. Table 5.5 shows the FEM results of stress for these two problems with using different minimum element size of 2.25×10^{-7} mm and 2.25×10^{-8} mm respectively. The thermoelastic constant term σ_0 and the non-singular term $\tilde{\sigma}_r$ are also listed in the table. The value $\sigma_{r0,FEM}^{Axial}$ and $\sigma_{y0,FEM}^*$ in Table 5.5 are FEM solutions which are usually mesh dependence. However, the stress ratio $(\sigma_{r0,FEM}^{Axial} - \sigma_0 - \tilde{\sigma}_r)/\sigma_{y0,FEM}^*$ is independent of mesh size when same material property and FE mesh pattern are applied to the two problems. This means the irremovable FEM error can be eliminated by applying the same mesh pattern and same minimum element size to the unknown problem and reference problem. This also reveals that the elimination of the non-singular terms in the stress of axi-symmetric problems under thermal load is correct. In view of the fact that the exact solution of the reference problem shown in Fig. 5.9(b) has already been obtained [23, 25], the ISSFs for the unknown axi-symmetric problem can be solved by applying Eq. (5.6).

Table 5.5 Stress ratio of bonded axi-symmetric problem and reference problem

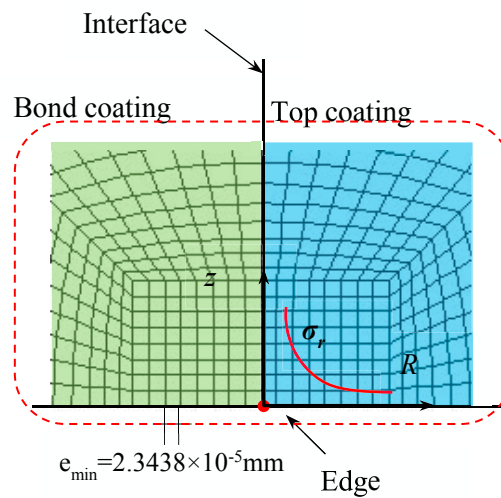
Items	Stress components	$e_{\min}/W=2.25\times 10^{-7}$		$e_{\min}/W=2.25\times 10^{-8}$	
		Mat. 1	Mat. 2	Mat. 1	Mat. 2
	$\sigma_{r0,FEM}^{Axial}$	1.2689×10^9	1.6841×10^9	1.8654×10^9	2.4035×10^9
	$\tilde{\sigma}_{r0,FEM}^{Axial}$	9.8708×10^7	9.8708×10^7	9.8708×10^7	9.8708×10^7
	σ_0	-8.4354×10^8	-8.4354×10^8	-8.4354×10^8	-8.4354×10^8
	$\sigma_{y0,FEM}^*$	2.2750×10^9	2.7441×10^9	2.9489×10^9	3.5568×10^9
	$\sigma_{r0,FEM}^{Axial} / \sigma_{y0,FEM}^{Plate}$	0.55776	0.61372	0.63257	0.67575
	$\frac{\sigma_{r0,FEM}^{Axial} - \sigma_0 - \tilde{\sigma}_{r0,FEM}^{Axial}}{\sigma_{y,FEM}^*}$	0.885158	0.885148	0.885155	0.885159

5.4 Results and Discussion for the Intensity of Singular Stress Field

The model used in analysis is shown in Fig. 5.10(a) with the local FEM mesh near the end of interface between top coating and bond coating shown Fig. 10(b). The minimum element size near the end of interface is $e_{\min}=2.3438\times 10^{-5}$ mm.



(a) Dimension of Analysis model



(b) Local FEM mesh

Fig. 5.10 Analysis model and local FEM mesh

Fig. 5.11 shows the stress history at the end of interface around the water cooling. The occurrence time of the largest singular stress is after the water cooling point, however K_σ takes a maximum value at the steady state (constant temperature of 1000°C) and decreases immediately after the start of cooling which has already been confirmed

in our previous study[18]. Therefore in this research we mainly pay attention to temperature 1000 °C. It's also found that the top material 8YZ, which means the content of Y_2O_3 is 8%, has the best thermal shock resistance among the three materials. This result coincides with the experimental result shown in Fig. 5.4(b). Therefore the following research will mainly focus on the structure with top coating of 8YZ.

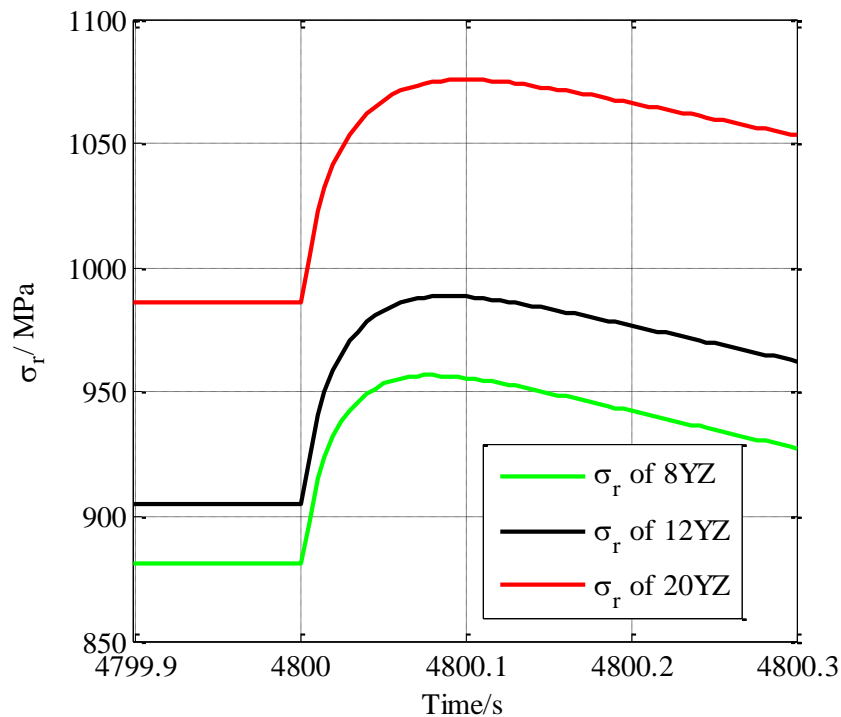


Fig. 5.11 Stress history at the end of interface around the water cooling

To investigate the effect of top coating and bond coating thickness on the stress intensity factor, the top coating thickness H and the bond coating thickness h of the FEM model were changed systematically. As shown in Fig. 5.10(a), the thickness of top coating was changed from 0.05mm to 0.30mm while the thickness of bond coating was changed from 0.025mm to 0.15mm. And the results of K_σ are listed in Table 5.6.

From Table 5.6 it can be found that the model with thinner top coating thickness always has smaller K_σ , or in other words, the thinner top coating has better thermal shock resistance. The results for each H constant in Table 5.6 were plotted in Fig. 5.12, and it can be found that the singular stress intensity reaches its minimum value when

the coating thickness ratio of top coating and the bond coating $H/h \approx 2$, which is in accord with the results for plane strain state model shown in Table 5.7[18]. This also coincides with the experimental results in engineering.

Table 5.6 K_σ for 8YZ at 1000°C (axi-symmetric model)

Bond coating thickness	H=0.05m m	H=0.12m m	H=0.15m m	H=0.20m m	H=0.30m m
h=0.025mm	308.44	332.45	342.51	355.46	375.17
h=0.060mm	310.27	328.85	336.48	347.37	364.67
h=0.075mm	311.64	328.97	336.09	346.31	362.74
h=0.100mm	314.67	329.92	336.21	345.67	360.33
h=0.150mm	319.05	332.65	339.26	347.78	359.98

*(Red figure shows minimum value when $H=\text{const.}$) [$\text{MPa} \cdot \text{m}^{0.1127}$]

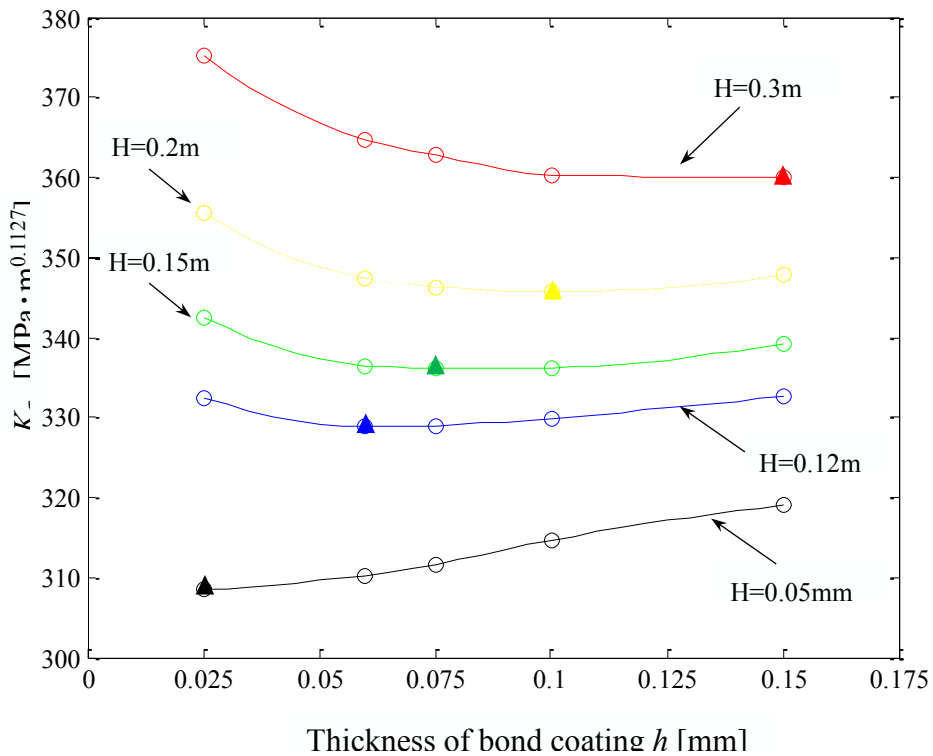


Fig. 5.12 K_σ for each constant thickness H of top coating

Chapter 5

Table 5.7 K_{σ} for 8YZ at 1000°C (plane strain model)[18]

Bond coating thickness	H=0.05m m	H=0.12m m	H=0.15m m	H=0.20m m	H=0.30m m
h=0.025mm	366.27	407.27	419.34	435.87	460.77
h=0.060mm	370.48	403.72	413.93	428.68	451.35
h=0.075mm	371.24	404.05	413.88	427.83	449.68
h=0.100mm	373.59	405.05	414.31	427.40	448.05
h=0.150mm	376.81	407.73	416.30	428.27	447.17

*(Red figure shows minimum value when $H=\text{const.}$) [$\text{MPa} \cdot \text{m}^{0.1127}$]

Table 5.8 $K_{\sigma}^{\text{plane}} / K_{\sigma}^{\text{axial-symmetric}}$ of 8YZ at 1000°C

Bond coating thickness	H=0.05m m	H=0.12m m	H=0.15m m	H=0.20m m	H=0.30m m
h=0.025mm	1.1875	1.2251	1.2243	1.2262	1.2282
h=0.060mm	1.1941	1.2277	1.2302	1.2341	1.2377
h=0.075mm	1.1912	1.2282	1.2315	1.2354	1.2397
h=0.100mm	1.1872	1.2277	1.2323	1.2364	1.2435
h=0.150mm	1.1810	1.2257	1.2271	1.2316	1.2422

It's important to understand the difference between the model specified by JIS8304 and actual axi-symmetric model, so that the error in evaluating the debonding strength of the ceramic spraying for a hearth roll can be eliminated. Therefore the ratio $K_{\sigma}^{\text{plane}} / K_{\sigma}^{\text{axial-symmetric}}$ for these problems are shown in Table 5.8. All results are larger than 1 which means the stress intensity factor of plane strain problem is larger than that of axi-symmetric problem. Or in other words, the JIS specimen is more dangerous than the actual shaped model under 1000°C. For different coating thickness, the difference of SIFs for these two problems varies from 18.10% to 24.35%. The result in Table 5.8 indicate that the error in evaluating the debonding strength of an actual shaped hearth roll using the JIS specimen is around 20%. However, the JIS

standard is relatively safe since the SIFs of JIS specimen are always larger than the axi-symmetric model.

5.5 Conclusion

This chapter focuses on the optimum design of ceramic spray coating by considering the intensity of singular stress at the end of interface. Previous researches are based on the JIS specimen under plane state, while this research focuses on the real shape of hearth roll which should be an axi-symmetric problem in practical engineering. The stress intensity factor for different coating thickness and different materials of top coating were analyzed. Furthermore, the new results were compared with the previous research based on the JIS specimen and the difference between actual model and JIS specimen was obtained. The achievements of this chapter have been conclude as follows:

(1) By eliminating the non-singular term $\tilde{\sigma}_r$ and thermal constant σ_0 from the total stress of axi-symmetric problem, the proportional method was verified to be available in the solution of axi-symmetric problem under thermal load.

(2) Both experimental results and analysis results showed that the dangerous point is between the top coating and bond coating, and for the material of top coating, 8YZ with the minimum content of Y_2O_3 shows the best performance of thermal shock resistance. Therefore the analysis mainly focused on the intensity of singular stress field near the end of interface between top coating of 8Y and bond coating.

(3) It's found that thinner top coating always has better thermal shock resistance. And for each constant top coating thickness, the singular stress intensity reaches its minimum value when the coating thickness ratio of top coating and the bond coating $H/h \cong 2$, which is in accord with previous research for plane strain state and experimental results in engineering.

(4) The difference between actual shaped cylindrical model and JIS model under plane strain state was obtained by comparing the stress intensity factor of these two problems. It's found that JIS specimen is dangerous than the real shaped model. The

stress intensity factor of plane strain model is approximately 20% larger than that of cylindrical model.

5.6 Reference of Chapter 5

- [1] Iseki T, Kameda T, Maruyama T. Interfacial Reaction Between SiC and Aluminum During Joining [J]. *Journal of Science*. 1984, 19 :1, pp.692~1 - 698
- [2] Turman, Bobby N, Glass, S. J, Halblerb, J. A., Helmich, D. R. High-energy electron beam for ceramic joining [J]. *Proceedings of SPIE: The International Society for Optical Engineering*, 1995, 23 (74) :10~18
- [3] Samandi M, Gudze M, Evans P. Application of Ion Implantation to Ceramic/metal Joining [J]. *Nuclear Instruments and Methods in Physics Research B*, 1997, (127/128): 699
- [4] Piekoszewski J, Krajewski A, Prokert F, et al. Brazing of Alumina Ceramics Modified by Pulsed Plasma Beams Combined with Arc PVD Treatment [J]. *Vacuum*, 2003, (70): 307
- [5] D. Treheux et al. Metal-Ceramic Solid state Bonding: Mechanisms and Mechanics [J]. *Scripta Metallurgical et Materialia*, 1994,31(8): 1055-1060
- [6] Li. S.J, Duan. H. P., Reaction Characteristics of the Filers for SHS Welding of SiC Ceramic to Ni based Supper-alloy[J]. *International Symposium on SHS*. Moscow, August 16-19, 1999
- [7] Munir. Z.A, Mccoy. B.J, Risbud S.H. Formation of Functionally Grade Materials through Centrifugal-assisted Combustion Synthesis. *Proceeding of 4th international Symposium on Functionally Grade Materials* [J]. Tsukba, Japan. October 21-24, 1996, Elsevier. 1997: 587-589
- [8] Dundurs, J., Discussion of edge bonded dissimilar orthogonal elastic wedges under normal and shear loading, *Journal of Applied Mechanics*, 36 (1969) 650-652.
- [9] Dundurs, J., Effect of Elastic Constants on Stress in a Composite under Plane Deformations, *Journal of Composite Materials*, 1(1967), 310.
- [10] D.B.Bogy: *Trans. of the ASME Jour. of Applied Mech.*, 38(1971), 377.

Chapter 5

- [11] D.B.Bogy: Trans. of the ASME Jour. of Applied Mech., 35(1968), 460 .
- [12] JIS H 8304: 2007. Ceramic Thermal Spraying
- [13] W. Lankford, N. Samways, R. Craven, and H. McGannon, The Making, Shaping and Treating of Steel, United States Steel, 1985
- [14] R.L. Hao, Thermal Spraying Technology and Its Applications in the Iron & Steel Industry in China, Thermal Spray 2007: Global Coating Solutions, B.R. Marple, M.M. Hyland, Y.C. Lau, C.J. Li, R.S. Lima, and G. Montavon, Ed., 14-16 May, 2007 (Beijing, China), ASM International, Materials Park, OH, 2007, p 291-296
- [15] S. Kasai, Y. Sato, A. Yanagisawa, A. Ichihara, and H. Onishi, Development of Surface treatment Techniques for Process Rolls in Steelworks, Kawasaki Steel Technical Report No. 17, 1987, p 81-90
- [16] M. Sawa and J. Oohori, Application of Thermal Spraying Technology at Steelworks, Thermal Spraying: Current Status and Future Trends: Proceedings of the 14th International Thermal Spray Conference, A. Ohmori, Ed., 22-26 May, 1995 (Kobe, Japan), High Temperature Society of Japan, 1995, p 37-42
- [17] Y.Mutoh, I.Sakamoto, O.Waranabe and T.Nishimura, Failure Characteristics of Zirconia-Coated Structural Steel Under Thermal Cycling and Thermal Shock, Quarterly Journal of the Japan Welding Society, Vol. 7 (1989) No. 2, pp. 208-213.
- [18] Nao-Aki Noda, Takumi Uchikoba, Masayasu Ueno, Yoshikazu Sano, Kazuki Iida, Zefeng Wang, Guohui Wang, Convenient Debonding Strength Evaluation for Spray Coating Based on Intensity of Singular Stress, ISIJ International, Vol. 55, No.12(2015), pp.2624-2630.
- [19] Y.Zhang, N.A.Noda, K.Takaishi and X.Lan: Trans. Jpn. Soc. Mech. Eng. A, 77 (2011a) , No.774, 128.
- [20] Y.Zhang, K.Takaishi, N.A.Noda and X.Lan: Trans. Jpn. Soc. Mech. Eng. A, 77 (2011b) , No. 784, 2076
- [21] Tatsujiro Miyazaki, Nao-Aki Noda, Zefeng Wang, Yoshikazu Sano. Analysis of Intensity of Singular Stress Field for Bonded Cylinder in Comparison with Bonded Plate. Transactions of the JSME, vol.81 (829) (p.1-14), 2015.08

Chapter 5

[22] S.Ioka, S.Kubo, K. Ohji and J.Kishimoto: Trans. Jpn. Soc. Mech. Eng. A, 60 (1994), No.572 , 141.

[23] Chen, D.H., and Nisitani, H., Intensity of Singular Stress Field near the Interface Edge Point of a Bonded Strip, Transactions of the Japan Society of Mechanical Engineers Series A, Vol. 59 (1993) No. 567 pp. 2682-2686.

[24] Noda, N.A, Shirao, R., Li, J. and Sugimoto, J.S., Intensity of Singular Stress at the End of a Fiber under Pull-out Force, International Journal of Solids and Structures, Vol. 44, No.13(2007), pp. 4472-4491.

[25] T.Teranishi and H. Nisitani: Trans. Jpn. Soc. Mech. Eng. A, 65 (1999-10), No.638, 16.

Chapter 6 Conclusion

The bonded axi-symmetric structures have been widely used in the steel and petroleum industries recent years. However, as is known that there is stress singularity at the end of interface for different materials, which may result in the failure of the joint. The intensity of singular stress has already been discussed for bonded plate under arbitrary material combination, while few studies are available for the intensity of bonded structures in axi-symmetric problems, and no results with varying material combination. Thus this research concentrated on the analysis of ISSFs of different axi-symmetric problems with arbitrary material combinations, which may make a contribution on a general understanding of the strength for an axi-symmetric problem. And in addition, this method was applied in the analysis of a practical engineering problem to verify the significance of this study. This thesis is concluded as follows.

1. The axi-symmetric problems are different from plane strain/stress problems when directly apply the proportional method. The stress components of $\sigma_{z0,FEM}^{Axial}$ and $\sigma_{\theta\theta,FEM}^{Axial}$ contain non-zero terms without singularity. The non-singular terms are originated from the circumferential strain $\varepsilon_{\theta}^{Axial}$. Since this strain component is controlled by the radial displacement at the end of interface, which is mesh independent, the non-singular terms are constant composition of the stress component. To extend the proportional method to the bonded axi-symmetric problems, this terms have to be eliminated from the stress.

2. It is found that the ratios of the all stress components without non-singular stress are same with 4 significant digits, which verified the derivation of the non-singular terms. It is also found that the ratios are almost independent of element size. This means proportional method can be used to evaluate the ISSFs of bonded axi-symmetric problems. Since the stress components σ_r^{AXIAL} and τ_{rz}^{AXIAL} do not contain non-singular terms, it will be easier to evaluated the ISSFs by using the ratio of these two stress

components.

3. The singular stress field near the end of interface of two dimensional problems is governed by Dundurs' parameters (α , β) uniquely regardless of the plane stress condition or the plane strain condition. However, the singular stress field of bonded cylinder is not governed by (α , β). Therefore the maximum and minimum value of $F_{\sigma}^{CYL}/F_{\sigma}^{PLT}$ should be considered. For bonded cylinder, the maximum value of $F_{\sigma_z}^{CYL}/F_{\sigma_y}^{PLT}$ tends to go infinite when it closes to the equal pair: $\alpha=2\beta$, and for equal pair and good pair, there is no singularity, therefore, there is no meaning for $F_{\sigma_z}^{CYL}/F_{\sigma_y}^{PLT}$ under good and equal pair. For the prediction of debonding strength of the bonded structure in good pair and close to equal pair, the direct ratio of stress $\sigma_{z0, FEM}^{CYL}/\sigma_{y0, FEM}^{PLT}$ is more suitable since it contains the influence of the non-singular stress.

4. For most material combinations which are distributed in $0 < \beta < 0.3$ under the (α , β) space, the range of $(\sigma_{z0, FEM}^{CYL}/\sigma_{y0, FEM}^{PLT})_{max}$ is approximately obtained as follows

$$0.8 \leq \frac{\sigma_{z0, FEM}^{CYL}}{\sigma_{y0, FEM}^{PLT}} \leq 1.5$$

And since the differences between $(\sigma_{z0, FEM}^{CYL}/\sigma_{y0, FEM}^{PLT})_{max}$ and $(\sigma_{z0, FEM}^{CYL}/\sigma_{y0, FEM}^{PLT})_{min}$ is less than about 10%, the effect of the material combination can be put in order by Dundurs' parameters (α , β).

5. The stress components for bonded pipe converged when $R_i/W \geq 10^2$, and also same stress component at inner point and outer point coincide each other when $R_i/W \geq 10^2$, which means the change of inner radius or R_i/W has no effect on the stress components if it's large enough. Although the change of inner radius or R_i/W has no effect on the stress components when it's large enough, there are still differences between the bonded pipe and bonded plane strain problem since the existence of non-singular circumference strain ε_{θ} in bonded axi-symmetric problems.

6. The analysis method used in bonded cylinder is suitable for bonded pipe if accurate radial displacement at the end of interface can be obtained. Similar as bonded

cylinder, it's suitable to use $F_{\sigma_z}^{PIPE}/F_{\sigma_y}^{PLT}$ for the prediction of debonding strength of the bonded pipe in bad pair, as for good pair and close to equal pair, the direct ratio of stress $\sigma_{z0, FEM}^{PIPE}/\sigma_{y0, FEM}^{PLT}$ is more suitable since it contains the influence of the non-singular stress. For most material combinations which are distributed in $0 < \beta < 0.3$ under the (α, β) space, the range of $\left(\sigma_{z0, FEM}^{PIPE}/\sigma_{y0, FEM}^{PLT}\right)_{max}$ is approximately obtained as follows

$$1.0 \leq \frac{\sigma_{z0, FEM}^{PIPE}}{\sigma_{y0, FEM}^{PLT}} \leq 1.3$$

And since the differences between $\left(\sigma_{z0, FEM}^{PIPE}/\sigma_{y0, FEM}^{PLT}\right)_{max}$ and $\left(\sigma_{z0, FEM}^{PIPE}/\sigma_{y0, FEM}^{PLT}\right)_{min}$ is less than about 10.5%, the effect of the material combination can be put in order by Dundurs' parameters (α, β) .

7. The last part of this research focuses on the optimum design of ceramic spray coating by considering the intensity of singular stress at the end of interface. Previous researches are based on the JIS specimen under plane state, while this research focuses on the real shape of hearth roll which should be an axi-symmetric problem in practical engineering. By eliminating the non-singular term $\tilde{\sigma}_r$ and thermal constant σ_0 from the total stress of axi-symmetric problem, the proportional method was verified to be available in the solution of axi-symmetric problem under thermal load.

8. Both experimental results and analysis results showed that thinner top coating always has better thermal shock resistance. And for each constant top coating thickness, the singular stress intensity reaches its minimum value when the coating thickness ratio of top coating and the bond coating $H/h \cong 2$, which is in accord with previous research for plane strain state and experimental results in engineering. The difference between actual shaped cylindrical model and JIS model under plane strain state was obtained by comparing the stress intensity factor of these two problems. It's found that JIS specimen is dangerous than the real shaped model. The stress intensity factor of plane strain model is approximately 20% larger than that of cylindrical model.

Appendix A

Convenient Debonding Strength Evaluation for Spray Coating Based on Intensity of Singular Stress

Abstract: Hearth rolls are used in continuous annealing furnace to produce thin steel sheet. The roll surface is usually coated by using thermal spraying, which has high adhesive strength and wears resistance. However, in the ceramics coating, thermal stress caused during heating and cooling process in the furnace may lead to debonding due to the low toughness of ceramics. In order to improve the heat resistance of the thermally sprayed coating, it is essential to evaluate the debonding strength. Generally, heat resistance of thermal spray coating is evaluated by thermal shock test prescribed by JIS H8304 although few research is available in terms of singular stress at the end of the interface for JIS specimen under thermal shock. This research focuses on the intensity of the singular stress at the end of interface. Then, the most suitable conditions are discussed with varying the coating material and the coating thickness.

Key words: ceramics, rooling, interface, strength, thermal spraying, thermal shock, Intensity of Singular Stress

A.1 Introduction

In continuous annealing furnace for producing steel sheet, hearth rolls as shown in Fig. A.1(a) are used to produce thin sheet. To prevent against steel adhesive and to improve wear resistance, ceramics spraying coating is usually applied to the roll surface. Due to its excellent chemical stability and high hardness at high temperatures, the wide

Appendix A

use of ceramics spraying coating is expected. However, the peeling of the coating layer should be considered after long-term use, which is mainly caused by heating and cooling process in the furnace. Therefore, the ceramic coating is not usually used as a single layer, while multi-layer coating with adhesive layer is usually employed.

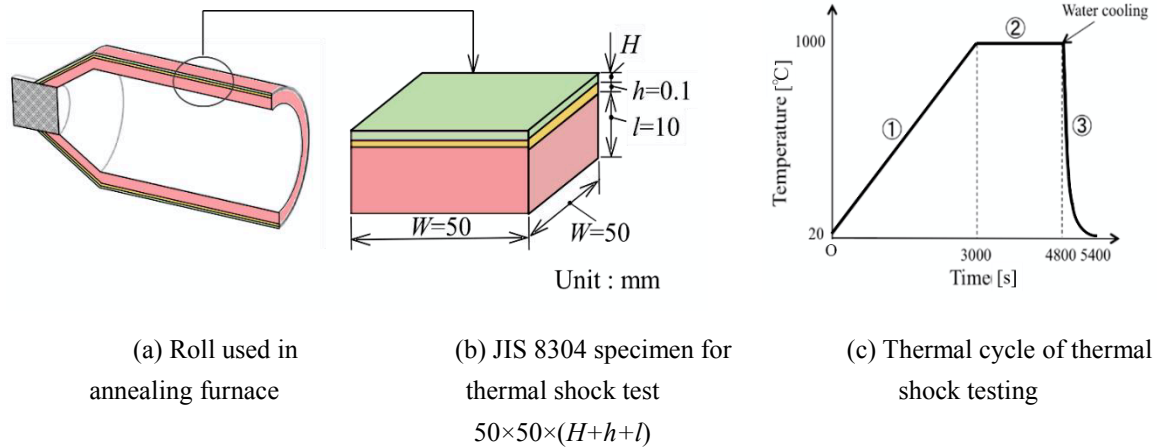


Fig. A.1 Specimen for thermal shock test and the test conditions

In order to improve the thermal shock resistance of the ceramic coating, it is necessary to accurately evaluate the peel strength of the sprayed coating. The thermal shock resistance of ceramic coating is usually evaluated by the thermal shock test (Fig. A.1 (b),(c)) specified by JIS8304 (2007) [1]. Mutoh et al have reported the thermal shock damage characteristics based on experimental results and finite element analysis [2]. However in order to more accurately assess the interfacial strength of dissimilar materials adhesive structures, it is necessary to consider the singularity of thermal stress near the corner of the interface. So far, few studies have been conducted to the research of intensity of singular stress on this multi-layer structure under thermal shock. In this study, the yttrium (Y_2O_3) stabilized zirconia (ZrO_2) sprayed coating shown in Table A.1 is used. We mainly focus on the intensity of singular stress near the edge of coating layer during the thermal shock test. And the effect of the coating thickness on the peeling strength (stated as fatigue life in experiment) of the sprayed coating will be investigated. In our previous study, an analysis method for the intensity of singular stress in an adhesive bonding plate under bending and tension has been proposed [3,4]. Thus in this paper, this method is applied to analysis the coating problem under thermal

shock.

A.2 Thermal shock test for evaluating the peeling strength of sprayed coating

JIS 8304 specimen is cubic shaped with length×width×thickness: 50mm×50mm×10mm. The substrate SUS304 and the top coating yttrium (Y_2O_3) with 8wt% ~ 20wt% of ZrO_2 (The following % will be omitted) are bonded with CoNiCrAlY(See Fig. A.1). In the experiments, the thickness of the bond coating is fixed as 100 μ m, and in order to ensure its adhesion with the top coating, the surface roughness of bond layer is adjusted to Ra4.5 μ m. After the top coating is sprayed to the bond coating surface, the coating is polished with thickness of 150 μ m and surface roughness of Ra1.0 μ m. Thermal shock test was carried out in an electric heating furnace by adjusting the ambient temperature. As shown in Fig. A.1(c), (1)the ambient temperature was first raised from 20 °C to 1000 °C during the first 3000 seconds, (2)and then during the following 1800 seconds, the temperature was kept as 1000 °C to ensures an even heat of the specimen; (3)after that, the specimen was taken out from the furnace and immersed into cold water of 25 °C. Repeat this process and the evaluation of delamination was performed by visual inspection, the number of cycles will be recorded until cracks, peeling or blistering of specimen occurs. The thermal shock resistance is evaluated by the numbers of cycles.

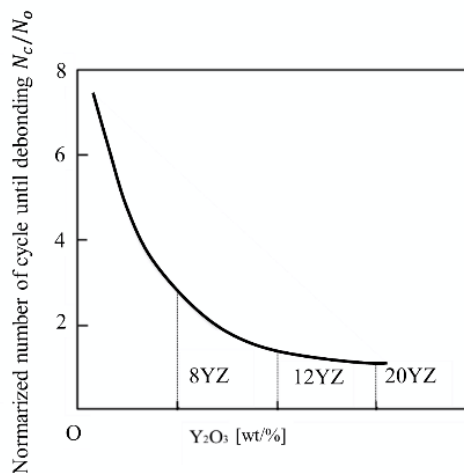
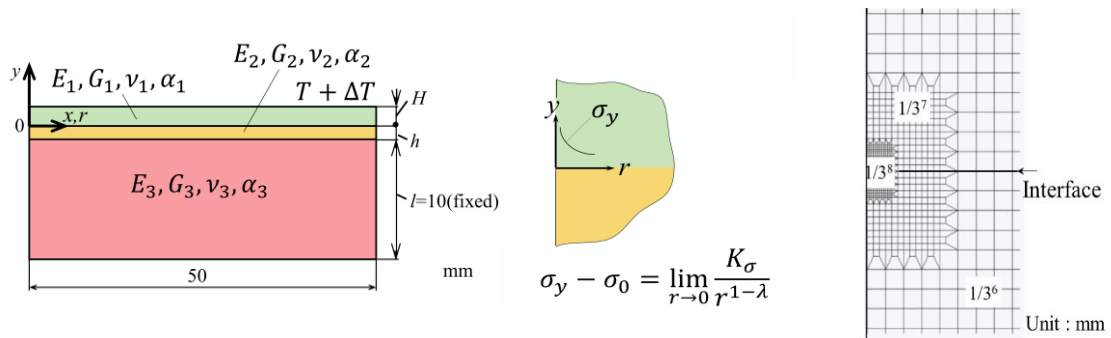


Fig. A.2 Results of thermal shock test

Appendix A

Table A.1 Material Properties depending on temperature

Material		Young's modulus E [GPa]	Poisson's ratio ν	Thermal expansion α_e [$10^{-6}/K$]	α	β	Singular index λ
Top Coating	20YZ (ZrO ₂ -20wt%Y ₂ O ₃)	20	0.25	7.5~9.7	0.969	0.199	0.8399~ 0.8899 Fig. A.4(c)
	12YZ (ZrO ₂ -12wt%Y ₂ O ₃)			8.3~9.93			
	8YZ (ZrO ₂ -8wt%Y ₂ O ₃)			8.7~10.05			
Bonded Coating(CoNiCrAlY)		103~180 Fig.A.4(a)	0.33	2.8~16.8 Fig. A.4(b)	0.978	0.188	0.9987~ 0.9988 Fig. A.4(c)
Substrate(SUS304)		85~200 Fig. A.4(a)	0.3	16.8~19.2 Fig. A.4(b)			



(a) Overview

(b) End of interface

(c) FEM mesh

Fig. A.3 Analytical model and FEM mesh

A.3 Analysis method for the singularity of thermal stress

In this study, FEM is used to analyze the destruction conditions of the sprayed coating by focusing on the failure initiated from the end of bonded interface. A two-dimensional model (plain stress problem) shown in Fig. A.3 is used to simulate the specimen, the subscripts 1, 2 and 3 represent the top coating, bond coating and substrate respectively, with the corresponding material properties shown in Table 1.

The MARC MENTAT (MSC Software Corporation, 2012) is used in this research and the 4 nodes quad element was employed. Multi-frontal method is used in the

solution of simultaneous equations. The analysis type is thermal-structural, and all materials are considered as elastic.

α and β in Table A.1 are known as Dundurs' parameters which are expressed by the following equations[5,6], here ν is Poisson's ratio and $G = E/2(1+\nu)$ is shear modulus.

$$\begin{aligned}\alpha &= \frac{G_1(\kappa_2 + 1) - G_2(\kappa_1 + 1)}{G_1(\kappa_2 + 1) + G_2(\kappa_1 + 1)}, \\ \beta &= \frac{G_1(\kappa_2 - 1) - G_2(\kappa_1 - 1)}{G_1(\kappa_2 + 1) + G_2(\kappa_1 + 1)}, \\ \kappa_j &= \begin{cases} \frac{3 - \nu_j}{1 + \nu_j} (\text{plane stress}) \\ 3 - 4\nu_j (\text{plane strain}) \end{cases} \quad (j = 1, 2)\end{aligned}\tag{A.1}$$

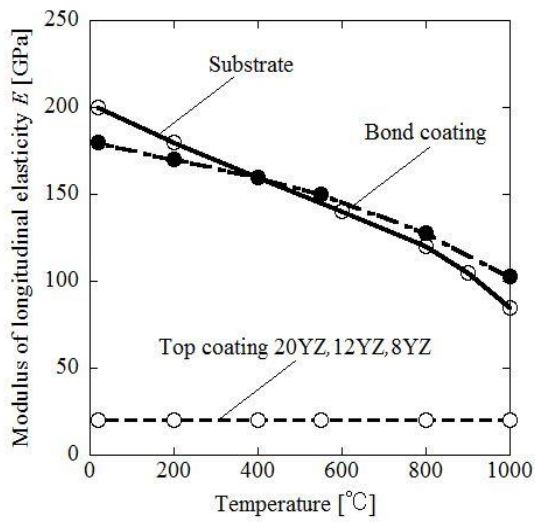
Furthermore, the singular index λ , appeared as the exponent of r in Fig. A.3(b), can be obtained by solving the following equation. Here r is the distance from the end of interface in a dissimilar materials bonded plate.

$$\left[\sin^2\left(\frac{\pi}{2}\lambda\right) - \lambda^2 \right] \beta^2 + 2\lambda^2 \left[\sin^2\left(\frac{\pi}{2}\lambda\right) - \lambda^2 \right] \alpha\beta + \lambda^2 (\lambda^2 - 1) \alpha^2 + \frac{\sin^2(\pi\lambda)}{4} = 0 \tag{A.2}$$

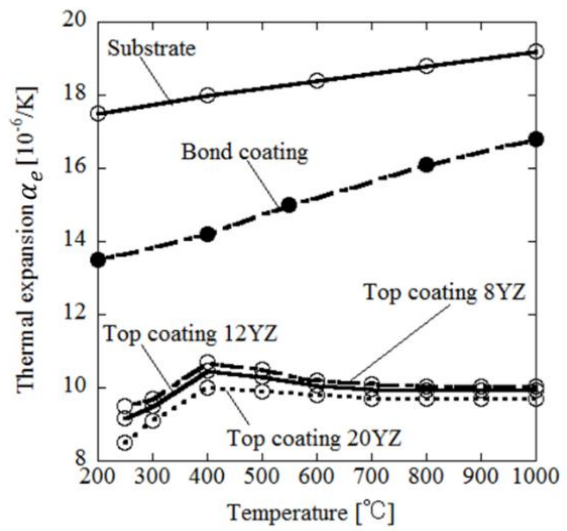
Fig. A.4 (a) and (b) show the material properties of three layers: young's modulus E and coefficient of expansion α_e . It's found that all properties of these three materials vary with the temperature except the Poisson's ratio of top coating. Therefore, the singular stress field is also changed by the variety of material properties.

Fig. A.4 (c) shows the singular index λ_1 and λ_2 for the interfaces of the specimen. Singular index λ_2 of the interface between the bond coating and substrate is close to 1, which means less singularity. Therefore, this study will mainly focus on the singularity between top coating and bond coating as shown in Fig. A.3 (a). During the thermal cycles as shown in Fig. A.1, water-cooled condition is simulated by given temperature 20 °C to the entire surface of specimen at $t = 4800s$, then the temperature distribution and thermal stress was determined by thermal and elastic analysis.

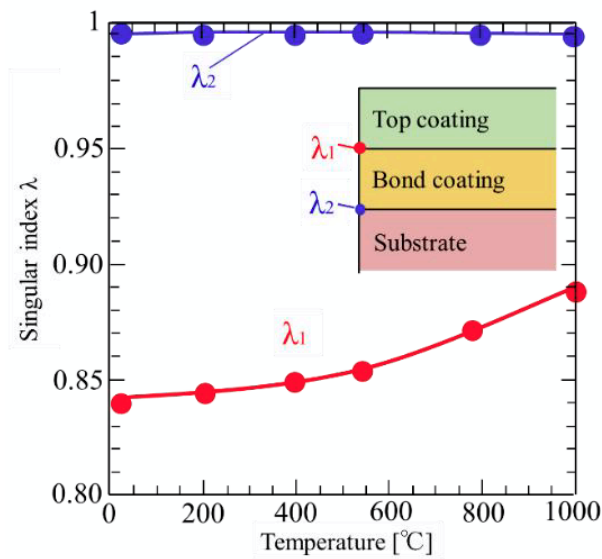
Appendix A



(a) Relationship between temperature and modulus of longitudinal elasticity



(b) Relationship between temperature and the coefficient of liner expansion



(c) Relationship between temperature and singular index λ

Fig. A.4 Relationship between various material properties and temperature

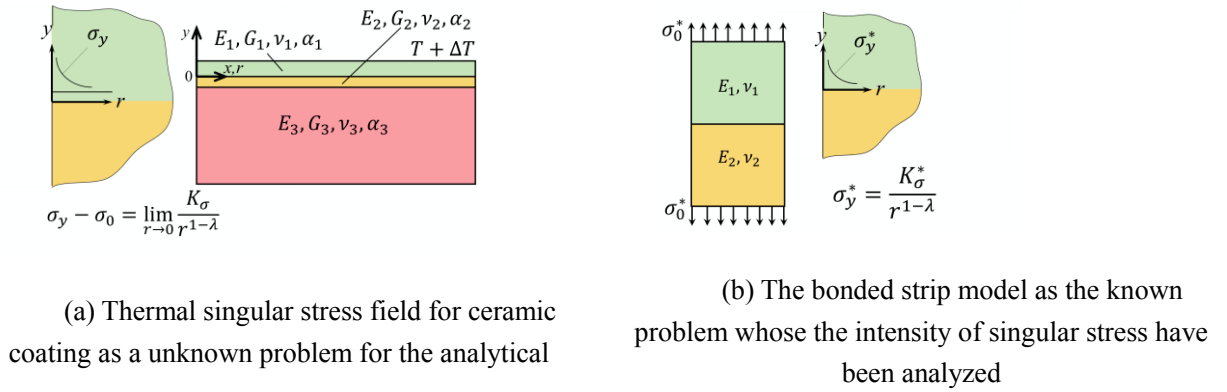


Fig. A.5 Comparing known problem and unknown problem

Thermal stress σ_y is caused by entire body temperature difference $T + \Delta T$ in the bonded structure shown in Fig. A.5(a). By eliminating the non-singular term σ_0 , the remaining singular term $(\sigma_y - \sigma_0)$ has a singularity of $r^{1-\lambda}$ expressed as Eq. A.3.

$$\sigma_y - \sigma_0 = \lim_{r \rightarrow 0} \frac{K_\sigma}{r^{1-\lambda}}, \quad K_\sigma = -\sigma_0 F_\sigma W^{1-\lambda} \quad (A.3)$$

This intensity of singular stress field caused by thermal stress is equivalent to the one that subjected to the tension of σ_0 determined by Eq. A.4[8].

$$\sigma_0 = -\Delta\alpha\Delta E\Delta T, \quad (A.4)$$

where,

$$\Delta\alpha = \begin{cases} \alpha_1 - \alpha_2 & (\text{plane stress}) \\ (1 + \nu_1)\alpha_1 - (1 + \nu_2)\alpha_2 & (\text{plane strain}) \end{cases} \quad \Delta E = \frac{8}{\left\{ \frac{(\kappa_1 - 3)}{G_1} - \frac{(\kappa_2 - 3)}{G_2} \right\}}$$

$$\kappa_j = \begin{cases} \frac{3 - \nu_j}{1 + \nu_j} & (\text{plane stress}) \\ 3 - 4\nu_j & (\text{plane strain}) \end{cases}$$

$$G_i = \frac{E_i}{2(1 + \nu_i)} \begin{cases} i = 1 : \text{Top coat,} \\ i = 2 : \text{Middle coat} \end{cases}$$

The problem of finite bonded plate subjected to tension shown in Fig. A.5 has been accurately calculated by using body force method [1, 2]. Since the singular stress fields are similar if the material angles of two bonded structures are same, then the stress intensity of unknown problem shown in Fig. A.5(a) can be determined by apply this

Appendix A

known solution (Fig. A.5(b)) to Eq. A.5[3-4,9].

$$\frac{K_s}{K_s^*} = \frac{F_s S_0 W^{1-l}}{F_s S_0^* W^{1-l}} = \frac{S^{FEM} - S_0}{S_y^{FEM^*}} \quad (A.5)$$

Here the superscript * means known reference problem.

Table A.2 shows the results of stress distribution along the interface for the problems shown in Fig. A.5(a), (b) at the time $t=4800s$ with using different minimum element size of $1/3^8$ mm and $1/3^{10}$ mm. The value σ_y^{FEM} in Table A.2 are FEM solutions which are usually mesh dependence. However, the stress ratio $(\sigma_y - \sigma_0)/\sigma_y^{FEM^*}$ is independent of mesh size and does not depend on the distance r from the end of interface. This means the irremovable FEM error can be eliminated by applying the same mesh pattern and same minimum element size to the unknown problem and reference problem. Since the reference problem has already been solved in the previous study [3-4, 9], the intensity of singular stress for problem shown in Fig. A.5(a) can be obtained by using Eq. A.5.

Table A.2 Stress distribution on the interface and the ratio of the stress

Mesh size= $1/3^8$ mm				Mesh size= $1/3^{10}$ mm			
r/W	$\sigma_y^{FEM^*}$ [MPa]	$\sigma_y - \sigma_0$ [MPa]	$\frac{\sigma_y^{FEM} - \sigma_0}{\sigma_y^{FEM^*}}$	r/W	$\sigma_y^{FEM^*}$ [MPa]	$\sigma_y - \sigma_0$ [MPa]	$\frac{\sigma_y^{FEM} - \sigma_0}{\sigma_y^{FEM^*}}$
0/6561	2300.0	1389.8	0.604	0/59049	2946.4	1778.4	0.604
1/6561	1741.1	1052.3	0.604	1/59049	2230.4	1346.2	0.604
2/6561	1639.3	990.9	0.604	2/59049	2099.9	1267.4	0.604
3/6561	1576.8	953.2	0.604	3/59049	2019.8	1219.1	0.604
4/6561	1535.7	928.2	0.604	4/59049	1967.1	1187.3	0.604
5/6561	1503.4	908.6	0.604	5/59049	1925.8	1162.4	0.604

A.4 Results and discussion for the intensity of singular stress field

A.4.1 Occurrence Time of the Largest Singular Stress

In the first place, the thermal load as shown in Fig. A.1(c) is applied to the standard specimen with coating thicknesses $H=0.15$ mm and $h=0.1$ mm (See the model in the

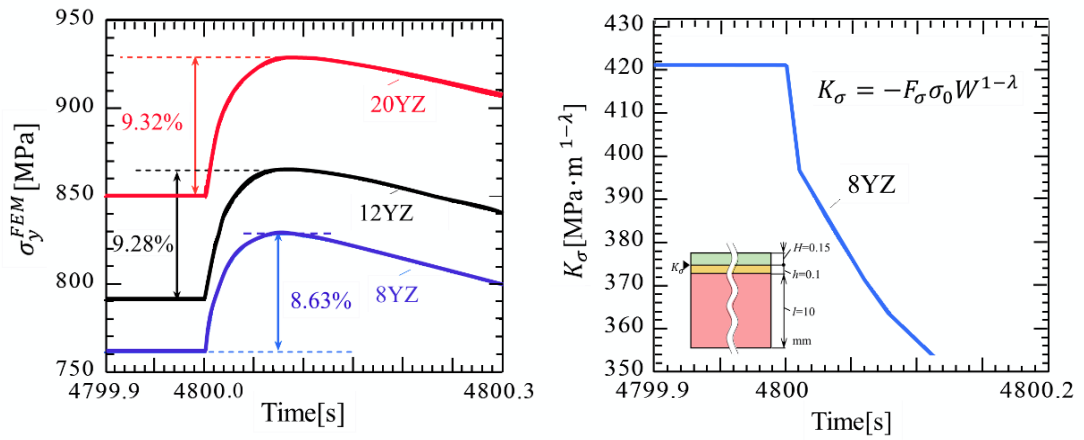
Appendix A

lower left corner of Fig. A.6(b). Although residual stress may appear in the ceramic spraying coating, but a number of micro-cracks are observed in the coating studied in this paper. Therefore, the residual stress is not considered because most of the residual stress is released after the crack formation. The thermal stress is not very large during the heating process in the thermal cycling, thus we mainly consider the thermal stress during the cooling process. Fig. A.6(a) shows the time variation of the interface stress σ_y^{FEM} obtained by FEM around the start of cooling $t=4800$ s. As shown in Fig. A.6, the maximum value of σ_y^{FEM} for the top coating occurs immediately after starting of cooling. The increment due to thermal shock in the percentage of total thermal stress for each coating material are shown in different colors, and the increment of 8YZ is the smallest of all. Fig. A.6(b) shows the time variation of the intensity of singular stress field for 8YZ around the starting of cooling. As shown in the figure, the intensity of singular stress field is different from the interfacial stress σ_y^{FEM} since it takes a maximum value at the steady state (constant temperature of 1000°C) and decreases immediately after the start of cooling. It should be noted that singular index varies depending on temperature, but from Fig. A.4(c), singular index is almost constant as $\lambda \cong 0.88$ during the first moment of cooling. Therefore, the value of $K_\sigma = -F_\sigma \sigma_0 W^{1-\lambda}$ with $\lambda \cong 0.88$ can be compared from Fig. A.6(b).

To figure out the reason that the maximum value of σ_y^{FEM} occurs immediately after the start of cooling, while K_σ decreases at the same time monotonically, all variables in Eq. A.3 are demonstrated in Table A.3 and Fig. A.7, so that a comprehensive consideration can be taken. The range of time is from the start of cooling $t=4800$ s to 4800.12 s. From Table A.3 and Fig. A.7, it is found that F_σ and $W^{1-\lambda}$ are almost constant within the variation of 1.9% and 5.2% respectively, while $-\sigma_0$ decreases 18.7% over time. For this reason, the tensile interfacial stress σ_y^{FEM} increases at the early stage of cooling while the intensity of singular stress field decreases by 16.5% as is shown in Fig. A.7. Therefore, in the following analysis of K_σ , we mainly pay attention to the

Appendix A

results of temperature 1 000°C.



(a) Stress at the end of interface by FEM
(mesh size $1/3^{10}$ mm)

(b) Intensity of the singular stress at the
interface for top coating 8YZ

Fig. A.6 Stress and intensity of the singular stress at the end of interface

Table A.3 This table shows that K_σ value of the influence factor changes with time for
top coating 8YZ

T [s]	4800	4800.01	4800.02	4800.03	4800.04	4800.06	4800.08	4800.12	Rate of change
T [°C]	1000	978.4	966.8	957.1	948.4	933.5	921.1	901.0	
K_σ [MPa·m ^{0.1127}]	421.2	397.0	391.3	386.1	381.0	371.4	363.2	351.6	16.5% ↓
F_σ	0.423	0.425	0.427	0.427	0.427	0.425	0.423	0.419	1.9% ↓
$-\sigma_0$ [MPa]	629.6	592.2	578.8	568.0	558.7	543.2	530.8	511.8	18.7% ↓
$W^{1-\lambda}$	1.554	1.576	1.584	1.592	1.598	1.608	1.617	1.640	5.2% ↑
σ_y^{FEM} [MPa]	761.2	791.9	806.7	815.9	821.7	827.2	828.4	825.5	7.8% ↑

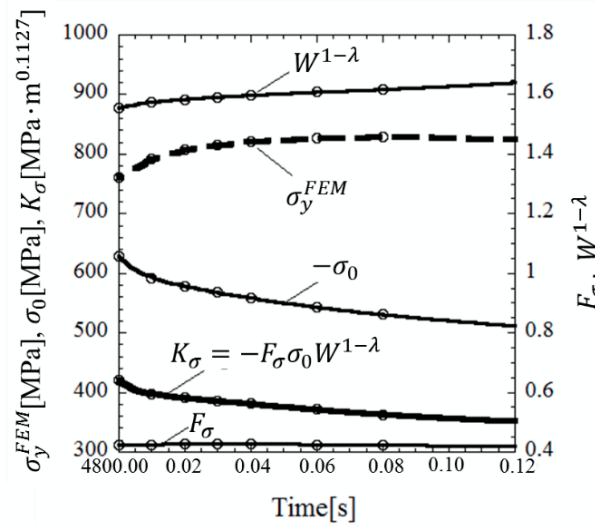


Fig. A.7 K_{σ} value of the influence factor changes with time

A.4.2 Intensity of singular stress for 2-layer coating

Here, three materials of the top coating with different content of yttrium (20YZ, 12YZ, 8YZ) are analyzed to determine the maximum intensity of singular stress field under thermal shock test. Fig. A.8 shows the intensities of singular stress for different materials with varying the top coating thickness H while keeping the bond coating layer thickness $h=0.1\text{mm}$. From Fig. A.8, it is found that the material 8YZ with the lowest content of Y_2O_3 exhibits the best thermal shock resistance under any thickness, which means thermal shock resistance has a negative correlation to the amount of added yttrium. And it can also be found that thinner top coating has higher thermal shock resistance.

Table A.4 shows the value of K_{σ} in case of changing top coating thickness H and the bond coat thickness h respectively. From Table A.4, it can be found that the singular stress intensity reaches its minimum value when the film thickness ratio of surface layer and the intermediate layer $H/h \cong 2$. In engineering application the ratio $H/h \cong 2$ is mostly used in the coating thickness design, and therefore the effectiveness of the present study on intensity of singular stress can be verified.

Appendix A

Table A.4 K_{σ} for 8YZ at 1000°C of two layers model

(Red figure shows minimum value when $H=\text{const.}$) [MPa·m^{0.1127}]

$H(\text{mm})$		0.05	0.12	0.15	0.20	0.30
$h(\text{m})$ m)	0.025	366.27	407.27	419.34	435.87	460.77
	0.06	370.48	403.72	413.93	428.68	451.35
	0.075	371.24	404.05	413.88	427.83	449.68
	0.10	373.59	405.05	414.31	427.40	448.05
	0.15	376.81	407.73	416.30	428.27	447.17

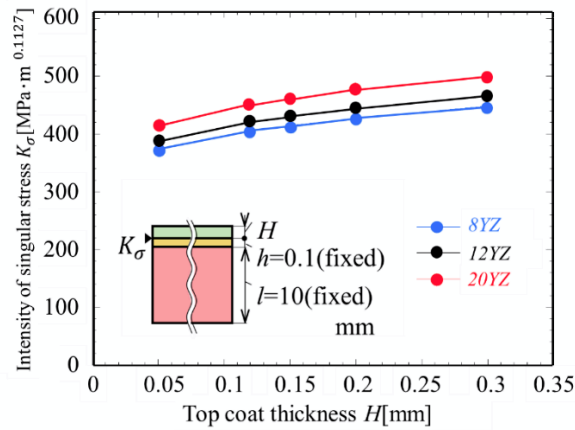
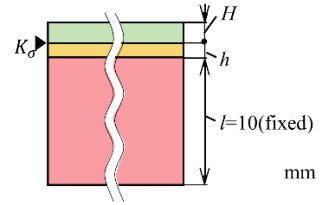


Fig. A.8 K_{σ} for 20YZ, 12YZ, 8YZ at 1000°C with varying ceramic coat thickness H when $h=0.1\text{mm}$

A.4.3 Intensity of singular stress for 3-layer coating

The intensity of singular stress K_{σ} in a two-layer coating with one layer of top coating and one layer of bond coating have been discussed in the previous section. And it is found that the singular stress of yttrium-rich 20YZ is the largest (thermal shock resistant is weak). While from another perspective, it's good to increase the content yttrium for the improvement of roughening resistance. Therefore a higher thermal shock resistance top coating with high yttrium content is desired. To accomplish that, a two layers of top coating (H_1+H_2) structure shown in Fig. A.9 is employed. The outer layer of top coating is 20YZ with high roughening resistance, and the second layer is 8YZ which exhibit a higher peeling resistance with the bond coat.

Table A.5 shows the result of K_{σ} when the thickness of the first layer of top coating

Appendix A

is fixed as $H_1=0.075$, the second layer of top coating H_2 varies from 0.015mm to 0.225mm and bond coat h varies from 0.005mm to 0.15mm. As same as the two-layer coating, when the ratio of top coating thickness and the bond coating thickness $(H_1+H_2)/h \cong 2$, the intensity of singular stress K_σ reaches minimum value. And K_σ decreased when (H_1+H_2) is reduced which means thermal shock resistant increases.

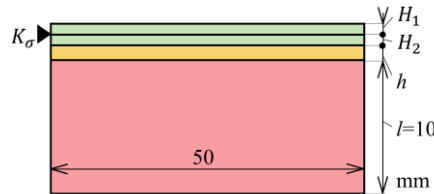


Fig. A.9 Three layers ceramic coating model used to analysis

Table A.5 K_σ at 1000°C of three layers model when fixed $H_1=0.075$ mm [MPa·m^{0.1127}]

H_2 (mm)	0.015	0.045	0.075	0.095	0.125	0.225	
H_1+H_2 (mm)	0.09	0.12	0.15	0.17	0.20	0.30	
h (mm)	0.025	408.09	419.43	430.01	436.42	445.12	468.58
	0.045	406.60	416.39	425.88	431.73	439.76	461.86
	0.060	407.10	416.06	424.91	430.42	438.03	459.2
	0.075	408.00	416.35	424.69	429.92	437.16	457.49
	0.085	408.87	416.84	424.83	429.85	436.83	456.53
	0.10	409.77	417.45	425.11	430.01	436.75	455.88
	0.15	413.09	420.19	427.22	431.61	437.70	455.05

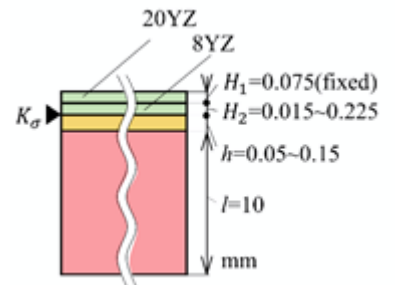


Table A.6 shows the result of K_σ when the thickness of the second layer of top coating is fixed as $H_2=0.075$, and the first layer of top coating H_1 varies from 0.015mm to 0.225mm and bond coating h varies from 0.005mm to 0.15mm. As shown in Table A.6, when the ratio of top coating thickness and the bond coat thickness $(H_1+H_2)/h \cong 2$, the intensity of singular stress K_σ reaches minimum value which is similar as Table A.4 and A.5. Fig. A.10 shows the distribution of the intensity of singular stress K_σ when the thickness of the top coating H_1+H_2 and the thickness of bond coat h are fixed as 0.15mm and 0.075mm respectively. From Fig. A.10, it can be found that the intensity of singular stress increases with increasing the top coating thickness H_1 .

Appendix A

Next, the strength improvement of the 3-layer coating in contrast with the two layers coating is considered. The 20YZ with excellent roughening resistance is used as the first layer film with the bond coat thickness $h=0.075\text{mm}$. The minimum value of singular stress field intensity $K_\sigma=424\text{ MPa}\cdot\text{m}^{0.1127}$ is obtained with $H_1=H_2=0.075\text{mm}$. Here, $H_1=H_2=0.075\text{mm}$ is the minimum allowable thickness in thermal spraying thickness.

Table A.6 K_σ at 1000°C of three layers model when fixed $H_2=0.075\text{mm}$ [$\text{MPa}\cdot\text{m}^{0.1127}$]

$H_1(\text{mm})$	0.015	0.045	0.075	0.095	0.125	0.225	
$H_1+H_2(\text{mm})$	0.09	0.12	0.15	0.17	0.20	0.30	
$h(\text{mm})$	0.025	398.38	416.05	430.01	438.07	448.79	476.32
	0.045	396.76	412.96	425.88	433.41	443.48	469.73
	0.06	397.21	412.62	424.73	432.11	441.78	467.14
	0.075	398.08	412.89	424.69	431.62	440.92	465.48
	0.085	398.93	413.37	424.83	431.56	440.6	464.55
	0.10	399.82	413.97	425.11	431.72	440.53	463.93
	0.15	403.10	416.70	427.22	433.33	441.50	463.17

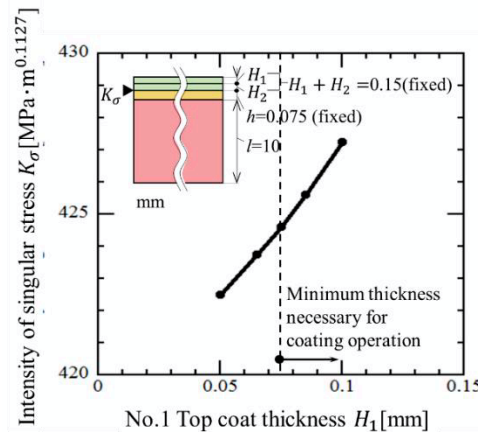
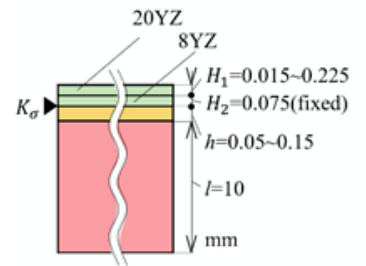


Fig. A.10 K_σ at 1000°C of three layers model when fixed $(H_1+H_2)=0.15\text{mm}$, $h=0.075\text{mm}$

Appendix A

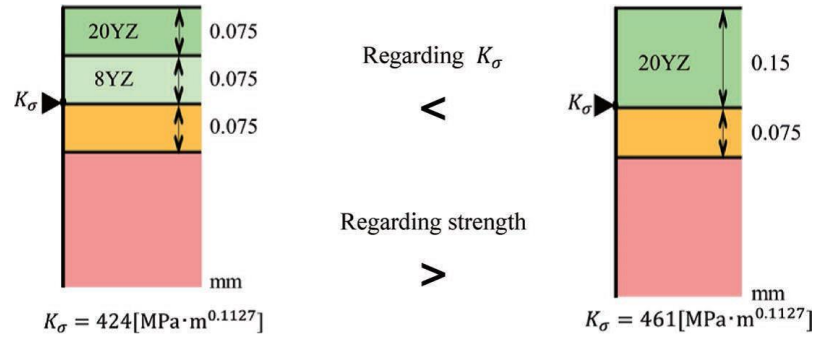


Fig. A.11 Comparison of the results for the three-layer and two-layer

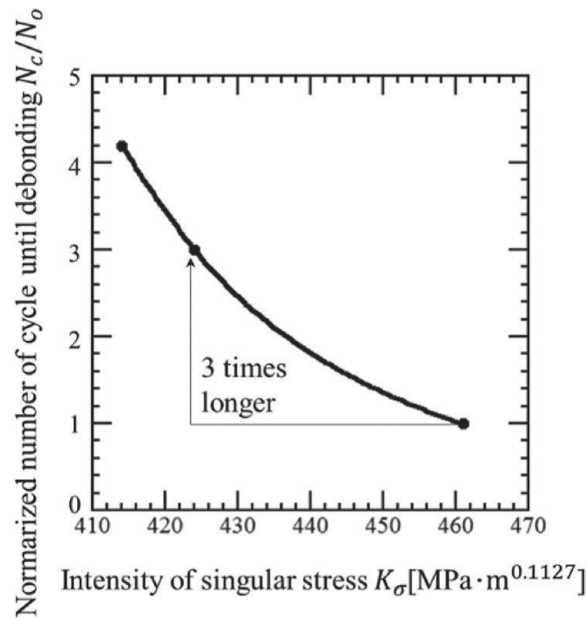


Fig. A.12 Relationship between N_c and K_σ

On the other hand, the minimum value of $K_\sigma=461\text{MPa}\cdot\text{m}^{0.1127}$ for a two-layer coating when $H=0.15$ mm and $h=0.075$ mm is about 8% higher than that of a three-layer coating. As shown in this example, when the top coating thickness $H(=H_1+H_2)$ and bond coating thickness h are fixed, it is found that the three-layer coating is better than two-layer coating in strength because of smaller K_σ . Fig. A.12 shows the relationship between K_σ and dimensionless cycle number N_c/N_0 . Here, vertical axis is dimensionless in the same manner as Fig. A.2. It is seen that the number of cycles until peeling increases about three times by using three-layer coating.

A.5 Conclusion

This study focuses on the improvement of peeling resistance for the thermal

sprayed coating roll using in the continuous annealing furnace. Considering the two-dimensional model based on the thermal shock test specimen, the effect of material properties and thickness of the sprayed coating on the intensity of singular stress field are discussed by using FEM analysis. As a result the following conclusions can be obtained.

(1) In the two-layer coating consisting of top coating and bond coating, experimental results shows that higher thermal shock peeling resistance can be obtained by smaller content of Y_2O_3 . This can be explained from the viewpoint of singular stress intensity K_σ near the end of interface for the top coating and bond coating. In other words, with decreasing Y_2O_3 content, K_σ decreases and therefore thermal shock resistance increases.

(2) Compared with the 2-layer structure, the 3-layer structure has higher thermal shock resistance because the stress intensity factor is 8% less than the 2-layer structure without losing a good roughening resistance. The first layer 20YZ (higher content of Y_2O_3) has excellent roughening resistance while the second layer 8YZ (lower content of Y_2O_3) can keep the thermal shock resistance.

(3) The optimal thickness ratio of top coating bond coating H/h is discussed from the view of intensity of singular stress near the end of interface. The theoretical analysis and engineering application all indicated that the optimal thickness ratio $H/h \cong 2.0$ both in 2-layer structure and 3-layer structure.

A.6 Reference of Appendix A

[1] JIS H 8304: 2007. セラミックス溶射

[2] Y. Mutoh, I. Sakamoto, O. Waranabe and T. Nishimura: Trans. Jpn. Welding Soc., 7(1989), No.2, 42.

[3] Y. Zhang, N. A. Noda, K. Takaishi and X. Lan: Trans. Jpn. Soc. Mech. Eng. A, 77 (2011a), No.774, 128.

[4] Y. Zhang, K. Takaishi, N. A. Noda and X. Lan: Trans. Jpn. Soc. Mech. Eng. A, 77 (2011b), No. 784, 2076

Appendix A

- [5] D. B. Bogy: Trans. of the ASME Jour. of Applied Mech., **38**(1971), 377.
- [6] D. B. Bogy: Trans. of the ASME Jour. of Applied Mech., **35**(1968), 460.
- [7] S. Ioka, S. Kubo, K. Ohji and J. Kishimoto: Trans. Jpn. Soc. Mech. Eng. A, **60** (1994), No.572, 141.
- [8] D. H. Chen, K. Nonomura and K. Ushijima: Trans. Jpn. Soc. Mech. Eng. A, **66** (2000), No.646, 130.
- [9] T. Teranishi and H. Nisitani: Trans. Jpn. Soc. Mech. Eng. A, **65** (1999-10), No.638, 16.